MINISTRY OF HIGHER EDUCATION
AND SCIENTIFIC RESEARCH

REPUBLIC OF CÔTE D'IVOIRE
UNION - DISCIPLINE - TRAVAIL

UNIVERSITY
FELIX HOUPHOUET BOIGNY

TRAINING AND RESEARCH UNIT
FOR STRUCTURE SCIENCES OF
MATTER AND TECHNOLOGY

DEPARTMENT OF PROCESS METALLURGY
AND METAL RECYCLING OF RWTH
AACHEN UNIVERSITY

Nº: 664

SPONSORED BY THE
Federal Ministry
of Education
and Research

INTERNATIONAL MASTER PROGRAM IN ENERGY AND GREEN HYDROGEN

SPECIALITY: PRODUCTION AND TECHNOLOGY OF GREEN HYDROGEN

MASTER THESIS

Topic:

ADVANCES IN UNDERSTANDING DIRECT HYDROGEN REDUCTION FOR THE PREPARATION OF METALLIC NANOPARTICLES

Presented on September 28, 2023, by:

Humphrey A. Hounsinou

JURY:

Dr. Zahiri Pascal	President	Associate Professor UFHB
Prof. Ello Aimé Serge	Examinator	Full Professor UFHB
Dr. Koffi Aka Stephane	Main Supervisor	Assistant Professor UFHB
Dr. -Ing. Srećko Stopić	Co-Supervisor	Associate Professor RWTH-AU

ACADEMIC YEAR: 2022-2023

ACKNOWLEDGMENTS

Above all else, with profound reverence, I express my heartfelt thanks to Almighty God for bestowing upon me the opportunity, strength, and knowledge to embark on this scholarly pursuit and bring it to a fulfilling culmination.

I am immensely grateful to WASCAL and the German Funder BMBF for their generous support in my academic journey. Without this scholarship, pursuing higher education would have been an insurmountable challenge for me. Furthermore, I would like to express my appreciation to the Chancellor of Abdou Moumouni University, Prof. Saïdou Mamadou, for hosting and providing facilities during the first year of the Master program in Niamey, Niger. I am also deeply thankful to Prof. Zié BALLO, Chancellor of Felix Houphouet Boigny University, for extending the same hospitality and support, making it possible for me to continue the second year of the program in Abidjan, Cote d'Ivoire. I would like to extend my heartfelt gratitude to Prof. Bernd Friedrich, the Head of IME at RWTH Aachen University, for providing me with unrestricted laboratory access and abundant resources that greatly enriched my research experience. My special thanks to Prof. Edouard Kouassi, the Director of WASCAL–COTE D'IVOIRE, for the invaluable material and logistical support provided during the second year of my master's degree. I also wish to sincerely thank the dedicated staff working with him.

I thankfully acknowledge the support of my Supervisor, Dr. Stéphane Aka Koffi, his availability, and relevant corrections on the document. I also offer my heartfelt gratitude to Dr. Srećko Stopić, my esteemed Co-Supervisor, for his unwavering guidance and wisdom throughout this research endeavor. Likewise, my sincere thanks go to the President of the Jury, Dr. Zahiri Pascal, and the Examiner, Prof. Ello Aimé Serge, for their valuable comments and evaluations of the document. Thanks to all my lecturers for providing me with exceptional and high-quality training during the first and second years of the Master's program. Thanks to all the administrative staff of WASCAL and IMP–EGH (Julich) for successfully organizing the launching program and coordinating the series of enriching educational events.

Finally, I would like to say a big thanks to my family and to all the individuals who have supported and contributed to my journey, whether directly or indirectly. Thank you from the bottom of my heart.

ABSTRACT

Due to their unique properties, nanomaterials find diverse applications across various fields, including catalysis, electronics, and energy storage. In this work, the hydrogen reduction-assisted ultrasonic spray pyrolysis method was used to synthesize simple alloy (Fe-Si and Fe-Pt) and complex alloy (AgCoCuFeNi) nanoparticles. The first part of the study focused on understanding the hydrogen reduction behavior of iron trioxide (Fe_2O_3) in the absence and presence of additives (SiO_2 or Pt). In the absence of additives, the oxygen content of iron oxide particles decreased with increasing temperature from 700 to 950 °C but significantly increased with the doping of 10 ml (40 wt.%) of SiO_2 at both reaction temperatures. The inhibitory effect of Si on the hydrogen reduction of Fe_2O_3 was more pronounced at 950 °C than at 700 °C. In contrast, the doping of only 5 ml (15 wt.%) of Pt significantly decreased the oxygen concentration in the synthesized particles by catalyzing the reduction reaction of Fe_2O_3 at 700 °C. The metallic iron (Fe) product, obtained in the undoped Fe_2O_3 run at only 950 °C, was also formed at 700 °C in the Pt-doped Fe_2O_3 run. The second part of the study consisted of investigating the influence of processing parameters (reaction temperature, precursor solution concentration, and residence time) on the microstructure, composition, and crystallinity of AgCoCuFeNi high entropy alloy nanoparticles using scanning electron microscopy, energy dispersive X-ray spectroscopy, and X-ray diffraction. The syntheses performed at 600, 700, 800, and 900 °C using a 0.05 M precursor mixture of metal salts resulted in smaller and smoother spherical particles with equiatomic elemental composition as temperature increased to 900 °C. With 0.25, 0.1, and 0.05 M precursor solutions at 900 °C, narrower size distribution and uniform AgCoCuFeNi nanoparticles were produced by reducing the solution concentration to 0.05 M. Equiatomic elemental composition was only obtained at 0.25 and 0.05 M concentrations. Increasing residence time from 5.3 to 23.8 s resulted in unclear particle microstructure. X-ray diffraction revealed that various crystal phase structures were obtained in the synthesized AgCoCuFeNi particles.

Keywords: Hydrogen reduction; Ultrasonic spray pyrolysis; High entropy alloy; Simple alloy.

RESUME

En raison de leurs propriétés uniques, les nanomatériaux trouvent diverses applications dans plusieurs domaines, notamment la catalyse, l'électronique et le stockage d'énergie. Dans ce travail, la méthode de pyrolyse par pulvérisation ultrasonique combinée avec la réduction par hydrogène a été utilisée pour synthétiser des nanoparticules d'alliages simples (Fe-Si et Fe-Pt) et complexes (AgCoCuFeNi). La première partie de l'étude s'est concentrée sur la compréhension du comportement de réduction par hydrogène du trioxyde de fer (Fe_2O_3) en l'absence et en présence d'additifs (SiO_2 ou Pt). En l'absence d'additifs, la teneur en oxygène des particules d'oxyde de fer a diminué avec l'augmentation de la température de 700 à 950 ° C, mais a augmenté de manière significative avec le dopage de 10 ml (40 % en masse) de SiO_2 à ces deux températures. L'effet inhibiteur de Si sur la réduction par hydrogène de Fe_2O_3 était plus prononcé à 950 °C qu'à 700 °C. En revanche, le dopage de seulement 5 ml (15 % en masse) de Pt a significativement diminué la concentration en oxygène dans les particules synthétisées en catalysant la réaction de réduction de Fe_2O_3 à 700 °C. Le produit de fer métallique (Fe), obtenu uniquement dans l'essai de Fe_2O_3-non dopé à 950 °C, s'est également formé à 700 °C dans l'essai de Fe_2O_3-dopé au Pt. La deuxième partie de l'étude consistait à étudier l'influence des paramètres d'expérimentation (température de réaction, concentration de la solution de précurseur et temps de séjour) sur la microstructure, la composition et la cristallinité des nanoparticules d'alliage à haute entropie (AgCoCuFeNi) à l'aide de la microscopie électronique à balayage, des rayons-X à dispersion d'énergie spectroscopique, et diffraction des rayons-X. Les synthèses effectuées à 600, 700, 800 et 900 ° C, en utilisant un mélange précurseur de 0,05 M de sels métalliques, ont donné une composition élémentaire équiatomique de particules sphériques plus petites (428 à 264 nm) et plus lisses lorsque la température a augmenté à 900 ° C. Avec des solutions de précurseurs de 0,25, 0,1 et 0,05 M à 900 °C, une distribution de taille plus étroite et des nanoparticules uniformes d'AgCoCuFeNi ont été produites en réduisant la concentration de la solution à 0,05 M. La composition élémentaire équiatomique n'a été obtenue qu'avec des concentrations de 0,25 et 0,05 M. L'augmentation du temps de séjour de 5,3 à 23,8 s a abouti à une microstructure peu claire des particules. La diffraction des rayons-X a révélé que diverses structures de phase cristalline ont été obtenues dans les particules d'AgCoCuFeNi synthétisées.

Mots-clés : Pyrolyse par pulvérisation ultrasonique ; Réduction par l'hydrogène ; Alliage simple ; Alliage à haute entropie.

TABLE OF CONTENTS

LIST OF FIGURES

LIST OF TABLES

ACRONYMS AND ABBREVIATIONS

ADB	: African Development Bank
APP	: Africa Progress Panel
at.%	: Atomic Percentage
BF	: Blast Furnace
BMNT	: Federal Ministry of Sustainability and Tourism
BOF	: Basic Oxygen Furnace
CAGR	: Compound Annual Growth Rate
CIA	: Central Intelligence Agency
DR	: Direct Reduction
EAF	: Electric Arc Furnace
EDS	: Energy Dispersive X-ray Spectroscopy
HEAs	: High Entropy Alloys
HER	: Hydrogen Evolution Reaction
HR	: Hydrogen Reduction
IME	: Institute of Process Metallurgy and Metal Recycling
INN	: Investing News Network
IR	: Indirect Reduction
Mt	: Million tons
NPs	: Nanoparticles
OER	: Oxygen Evolution Reaction
ORR	: Oxygen Reduction Reaction
PVD	: Physical Vapor Deposition
RWTH	: Rheinish-Westphalian Technical University
SEM	: Scanning Electron Microscopy
UNEP	: United Nations Environment Programme
USGS	: United States Geological Survey
USP-HR	: Hydrogen Reduction-assisted Ultrasonic Spray Pyrolysis
wt.%	: Weight Percentage
XPS	: X-Ray Photoelectron Spectroscopy
XRD	: X-Ray Diffraction

GENERAL INTRODUCTION

GENERAL INTRODUCTION

Research motivation and objectives

We often do not think about it, but a life without metals would be difficult, if not nearly impossible. Of the existing periodic table, they make up 80% and therefore, cannot be avoided. Metals play an important role in our bodies. Calcium, the most abundant metal in the human organism, is needed for bones. Iron is responsible for transporting oxygen to cells. Magnesium, potassium, and other trace metal elements are needed to perform many metabolic reactions within our bodies.

Metals and alloys have become an integral part of our modern way of life. Due to their physical properties, they have revolutionized the transportation sector (bikes, automobiles, ships, trains, airplanes), the construction sector (buildings, bridges, highways), and even the electronics sector (computers and electronic devices). Metals are also needed for electricity generation. Without the use of metals, mankind would be back in the Stone Age (Free, 2022).

Most pure metals are naturally found in ores within the Earth's crust in many regions of the world. Metals are also produced in large quantities in different places around the world. The world's annual production value of metals was estimated to be more than $2.8 trillion in 2020 (USGS, 2020), while the global metal manufacturing market is expected to grow to $4.5 trillion in 2026 at a CAGR of 7.3% (GlobeNewswire, 2022).

In terms of the share of global production, Africa accounts for a significant proportion of the world's metals as shown in Appendix 1. In addition to the metals depicted in Appendix 1, it is essential to highlight that two of the world's top-3 platinum-producing countries are located in Africa (BMNT, 2019). Of these top-3 countries, South Africa alone produces 72.07% of the world's platinum (APP, 2013). Likewise, it accounts for 80.70% of the world's rhodium production and 15.23% of the world's titanium production while the DRC accounts for 43.04% of the world's tantalum production (BMNT, 2019). At the present time, the DRC shares the place of the world's second-largest copper producer with Peru after overtaking China in 2022 (INN, 2023).

Furthermore, Africa has considerable potential for mining which is still untapped. In fact, the continent holds 30% of the world's total mineral reserves (ADB, 2012), placing it among the world's richest continents. Nearly half of the world's gold and up to 90% of its chromium and platinum lie beneath the surface of Africa (UNEP, 2022). In Benin, for instance, considerable reserves of iron ore estimated at over 600 Mt can be found and mined from its crust (Minergy Resources Ltd., 2023). Africa not only leads the world in the production of several metals but also accounts for a significant share of the world's total mineral reserves.

However, metals and their alloys have recently progressed from simple to complex component systems due to the increasing demand for materials with unique physical, chemical, or magnetic properties (Zhang *et al*., 2014). Usually, conventional alloys are based on one and rarely two principal elements (Yeh *et al*., 2004), such as silver in sterling silver, iron in steel, and nickel in superalloys, with only smaller amounts of other elements. But this traditional strategy has become less successful due to the limited number of base elements in the periodic table (Babić *et al*., 2021). Fortunately, a novel class of alloys based on multi-principal elements was independently introduced by Yeh *et al*. (2004) and Cantor *et al*. (2004) to reinforce the development of new materials. These complex metallic alloys, referred to as "high entropy alloys" (HEAs), are made by combining at least five well-mixed metal elements at equiatomic or near equiatomic concentrations (Yeh *et al*., 2004).

Because of their high mixing entropies, HEAs favor the formation of advanced materials with specific and diverse properties, including high thermal and chemical stability, excellent strength, outstanding corrosion and oxidation resistance, superconductivity, and magnetic properties (Zhang *et al*., 2013; Zou *et al*., 2017). Many of these properties cannot be achieved in conventional alloys, making HEAs a growing field of interest (Miracle and Senkov, 2017).

At the nanoscale (1 to 100 nm), HEAs, as well as traditional alloys, will exhibit more interesting properties compared to larger scales because of the shape, very small size, and chemical composition of the particles. HEA nanoparticles (NPs) can be used in a variety of potential applications, particularly as high-performance catalysts (Katiyar *et al*., 2021).

A variety of methods such as laser scanning ablation (Wang *et al*., 2022), carbothermal shock (Yao *et al*., 2018), wet chemical reduction (Lui *et al*., 2019), moving bed pyrolysis (Gao *et al.*, 2020), electrosynthesis (Glasscott *et al*., 2019), and ultrasonic spray pyrolysis (Simić *et al*., 2022; Küçükelyas *et al*., 2022) have been proposed for the synthesis of HEA NPs. Among these techniques, ultrasonic spray pyrolysis (USP) has been recognized as a very simple, cost-effective, and highly efficient method for synthesizing uniform particles with finite and controlled size (Stopić *et al*., 2006; Toparli *et al*., 2017; Muñoz-Fernandez *et al*., 2019).

USP is a continuous and one-step process in which a precursor solution is cold atomized in a nebulizer generating aerosol by ultrasound waves. Aerosol droplets are transported into a heating zone with a carrier gas, mainly a reducing agent, where they undergo evaporation, shrinkage, thermal decomposition, and densification to form spherical particles. The desired particle size and morphology can be controlled by varying the precursor solution concentration, temperature, gas flow rate, and reactor dimensions (Ebin and Gürmen, 2011; Toparli *et al*., 2013).

Besides the USP technique itself, choosing a preferable and environmentally friendly reducing agent is another important step for reducing massive CO_2 emissions in the metallurgical industry. In fact, the iron and steelmaking industry alone accounts for nearly 34% and 7% of industrial and global CO_2 emissions respectively (Raabe *et al*., 2019; Ma *et al*., 2022), motivating the replacement of carbon with hydrogen as the reducing agent for NPs (Patterer *et al*., 2023).

So far, various HEA NPs, such as NiCoCuFePt (Yang *et al.*, 2020), AgPdPtCuNi (Simić *et al*., 2022), and CoCuFeNi (Küçükelyas *et al.*, 2022), have been successfully synthesized using diverse techniques. However, the combination of AgCoCuFeNi alloy and its particle synthesis via the hydrogen reduction-assisted ultrasonic spray pyrolysis (USP-HR) technique has not been explored. Furthermore, while the inhibitory effect of silicon (Si) and the catalytic effect of platinum (Pt) on the hydrogen-based direct reduction of Fe_2O_3 have been investigated using sputter deposition **(**Patterer *et al*., 2023**)** and direct pyrolysis (Meng *et al*., 2019) methods, respectively, the USP-HR technique has received limited attention. Therefore, this thesis aims to synthesize and characterize simple alloy (Fe-Si and Fe-Pt) and complex alloy (AgCoCuFeNi) NPs by USP-HR.

The specific objectives of this thesis consist of using scanning electron microscopy (SEM), energy dispersive X-ray spectroscopy (EDS), and X-ray diffraction (XRD) analyses:

- To study the effect of the reaction temperature on the hydrogen-based reduction of Fe_20_3 at 700 and 950 °C.
- To compare the effect of Si on the hydrogen-based reduction of Fe_20_3 at 700 and 950 °C.
- To study the effect of Pt on the hydrogen-based reduction of Fe_20_3 at 700 °C.
- To study how the variation in furnace temperature influences the morphology, microstructure, composition, and crystallinity of AgCoCuFeNi NPs.
- To understand how the morphology, microstructure, composition, and crystallinity of AgCoCuFeNi NPs are modified through variation in precursor solution concentration.
- To analyze the transition in morphology, microstructure, composition, and crystallinity of AgCoCuFeNi NPs due to the change in residence time of aerosol droplets inside the furnace.

Research questions

The following three questions have been addressed in this thesis:

- Is it possible to inhibit the hydrogen reduction of Fe_2O_3 with silicon at 700°C by the USP technique? Will Si-doped Fe_2O_3 at 950 °C exhibit higher inhibition to reduction than Si-doped Fe_2O_3 at 700 °C?
- What is the effect of platinum on the hydrogen reduction of Fe_2O_3 at 700 °C?
- What are the suitable processing parameters (temperature, precursor concentration, residence time) to consider for optimizing the synthesis of spherical AgCoCuFeNi NPs?

Research hypotheses

These two main hypotheses were formulated based on the research questions:

- The hydrogen-based direct reduction of iron oxide (Fe_2O_3) can effectively be inhibited and accelerated by silicon (Si) and platinum (Pt), respectively.
- The optimization of synthesis conditions for spherical AgCoCuFeNi nanoparticles can be achieved by systematically investigating and adjusting processing parameters such as temperature, precursor concentration, and residence time.

In addition to the general introduction and conclusion, the thesis is divided into three chapters. Chapter 1 exposes an in-depth review of literature. Chapter 2 outlines the materials and methods employed to verify our hypotheses. Chapter 3 presents and discusses the results of our research.

CHAPTER 1.
LITERATURE REVIEW

CHAPTER 1. LITERATURE REVIEW

Introduction

This chapter reviews the relevant literature, with various aspects. The initial section focuses on the development of alloy nanomaterials and explains the fundamentals of HEAs. The second part of the chapter discusses the possible fabrication methods of HEA and traditional alloy NPs. Following that, the third part explains the importance of using hydrogen as a reducing agent for NP synthesis. It includes a detailed discussion of the thermodynamic analysis of metal salts via hydrogen reduction and explores the applications of synthesized nanoparticles. The fourth part provides an overview of the various characterization techniques used to study the microstructure, composition, and physical properties of NPs. Finally, the chapter concludes by identifying gaps in the existing research.

1.1. Development of nanomaterials: from simple to complex alloy systems

Throughout the history of human civilization, the development of new materials has been closely intertwined with technological progress. The journey of alloy development began with the combination of two or more elements, referred to as simple or traditional alloys, in which minor alloying elements are added to a single principal element to enhance its properties. An example of this practice can be seen in duralumin, where small amounts of copper, manganese, and magnesium are added to an aluminum base to enhance its strength and hardness. Similarly, in stainless steels, chromium is incorporated into an iron base to improve its resistance to corrosion, while the addition of nickel enhances its mechanical performance. The introduction of HEAs with remarkable properties disrupted this traditional foundation in metallurgy by introducing a new concept of alloys composed of multiple principal elements.

As mentioned in the introduction section, the concept of high entropy alloys (HEAs) was introduced by Yeh *et al*. in 2004 and defined as multi-principal elements made by combining at least five metal elements with (near) equiatomic concentrations between 5 and 35 at.% (Yeh *et al*., 2004). Unlike conventional alloys, HEAs explore compositions in the central region of multi-component phase diagrams (Figure 1.1a). The high configurational entropy (ΔS_{mix}) resulting from mixing multiple elements is the key factor behind the stabilization of solid solutions in HEAs (Miracle *et al*., 2014).

It is expressed by:

$$\Delta S_{mix} = -R \sum_{i=1}^{n} C_i \ln C_i \qquad \text{(Eq. 1.1)}$$

where R is the gas constant, C_i is the molar fraction of i^{th} element, and n is the total number of constituent elements. In an equiatomic HEA, the entropy reaches its maximum value with the configurational entropy (ΔS_{conf}):

$$\Delta S_{conf} = R \ln n \qquad \text{(Eq. 1.2)}$$

where n is the number of elements. Consequently, the configurational entropy ΔS_{conf} for an equimolar alloy containing 3, 5, 6, and 9 elements, using Eq. 1.2, amounts to 1.10R, 1.61R, 1.79R, and 2.20R, respectively.

Therefore, for a multi-component alloy to be categorized as a HEA, a proposed threshold for the lower limit of ΔS_{conf} is 1.5R. The addition of multiple elements in an alloy causes the entropy of mixing to increase, which, in turn, results in a decrease in the Gibbs free energy of mixing (ΔG_{mix}). This promotes the formation of stable solid solutions in a completely random equiatomic alloy with crystal structures such as face-centered cubic (FCC), body-centered cubic (BCC), or hexagonal close pack (HCP) (Figure 1.1b).

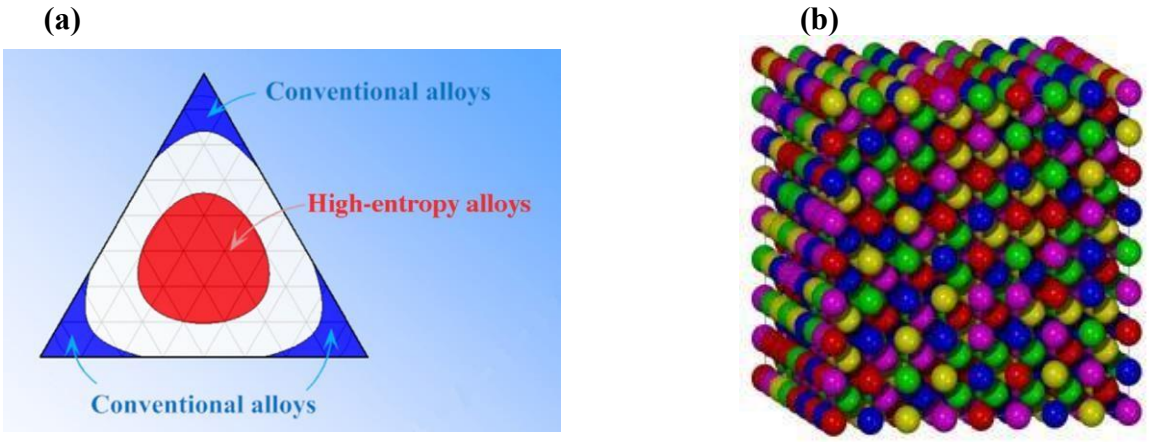

Figure 1.1. a) multi-component phase diagram highlighting the regions for conventional and high entropy alloys *(*Ye *et al*., 2016), b) atomic structure model of five-element bcc HEA phase by the MaxEnt method (Wang, 2013)

The relationship between ΔS_{mix} and ΔG_{mix} can be expressed by the following equation:

$$\Delta G_{mix} = \Delta H_{mix} - T\Delta S_{mix} \quad \text{(Eq. 1.3)}$$

where ΔH_{mix} is the enthalpy of mixing and T is the absolute temperature. The formation of phases in HEAs is influenced by the balance between ΔH_{mix} and $T\Delta S_{mix}$ product (Eq. 1.3). As the temperature increases, the $T\Delta S_{mix}$ term becomes more significant in this balance. Thus, at higher temperatures, the dominance of the $T\Delta S_{mix}$ term favors the formation of solid solutions in the material.

In addition, being able to mix different metals at the nanoscale will enable the formation of multicomponent metal nanoparticles with enhanced and unique physical and chemical properties (Chen *et al*., 2019). Nanomaterials, including both traditional alloy nanoparticles and high entropy alloy nanoparticles, have made significant contributions to recent technological advancements.

1.2. Fabrication routes of nanomaterials

Here, we will focus on some synthesis techniques used for high entropy alloy nanoparticles, which can also be adapted for traditional alloy nanoparticles.

1.2.1. Physical vapor deposition method

In physical vapor deposition (PVD), certain processes like heat evaporation convert solid particles into a gaseous state (Baptista *et al*., 2018a; Vu *et al*., 2019). This transformation occurs when the substrate is placed in a vacuum chamber with low gas pressure (Pinto *et al*., 2018). Figure 1.2 illustrates the mechanism of the PVD process.

Heating increases the kinetic energy of the atoms or molecules present in a solid or liquid state (Schneider *et al*., 2000; Baptista *et al*., 2018b). As the temperature rises, more atoms can overcome the energy barrier and avoid evaporation. The evaporated particles consist mainly of atoms, molecules, and clusters with various sizes and compositions (Wang *et al*., 2021; Stuart and Stan, 2021). To achieve evaporation, a laser beam or arc discharge is used to heat the material.

Compared to thermal evaporation, the composition and energy of the vapor particles are different. Additionally, when the target material is bombarded with ions having energies over 30 eV, surface particles and secondary electrons detach in a process known as sputtering (Ali *et al*., 2019; Gupta *et al*., 2021). These ejected particles, primarily molecules and atoms, then deposit on the substrate and the walls of the vacuum chamber, forming a film.

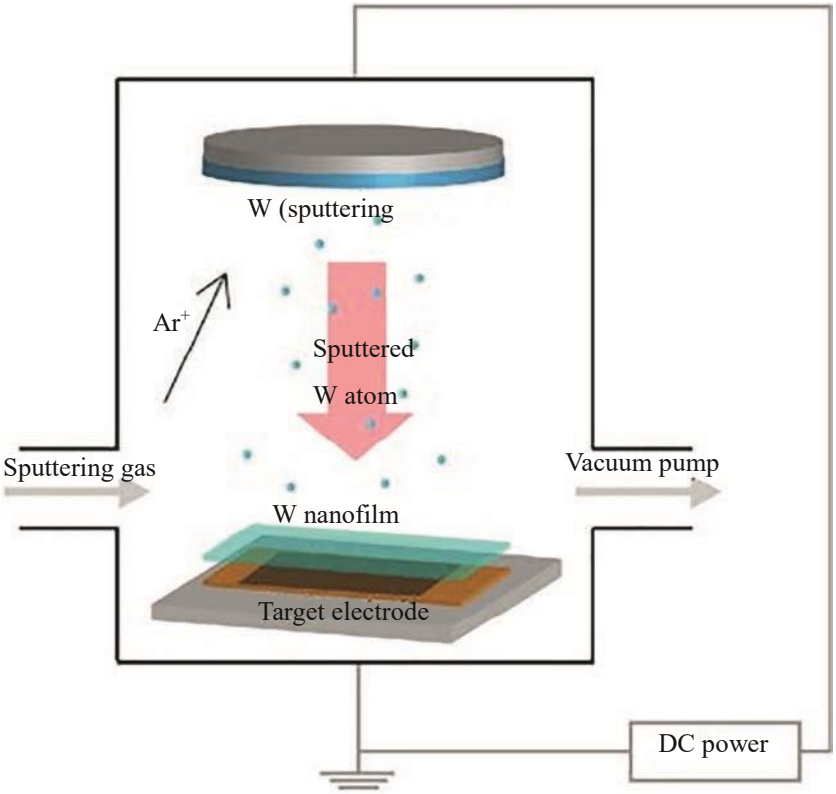

Figure 1.2. General mechanism of the physical vapor deposition process (Son *et al*., 2018)

PVD enables the easy deposition of high entropy alloy films through magnetron co-sputtering. It also allows obtaining high entropy nanomaterials with adjustable shapes and sizes using ionic liquids instead of traditional solid substrates in a top-down technique (Sun *et al*., 2021). For instance, high entropy CrMnFeCoNi nanoparticles were synthesized using ionic liquids through vapor deposition, resulting in extraordinary oxygen reduction reactions with complete compositional homogeneity of the material (Garzón-Manjón *et al*., 2018).

1.2.2. Laser deposition method

In the laser deposition method, a laser beam is utilized as a heating source to melt the coating material onto a substrate, enabling the creation of an alloy-clad layer (Arif *et al*., 2021; Zhu *et al*., 2021). Figure 1.3 shows an experimental setup for synthesizing high entropy alloy nanoparticles (HEA NPs) using the laser deposition technique. The process offers several advantages, including high input energy, low distortion, and the ability to selectively clad small areas (Santo, 2008; Singh *et al*., 2020). These characteristics make laser cladding suitable for specific mold metal component restoration. Researchers have explored different compositional systems, such as AlCoCrCuNi, to fabricate nanoparticles using laser cladding (Mao *et al*., 2018). The microstructure and properties of these nanomaterials were investigated with varying aluminum content. As the aluminum content increased, the microstructure transitioned from a single Cu-rich face-centered cubic (FCC) phase to a mixture of FCC + M3Al-type L12 phase, followed by FCC + body-centered cubic (BCC) phases. The authors found that the chemical compositions of the targets differed significantly from those of the nanoparticles, which exhibited a spherical shape and had an average size ranging from 110 nm to 180 nm. Hence, the laser cladding process can be used to create multicomponent nanoparticles with adjustable compositions and structures, offering potential in various applications and research fields.

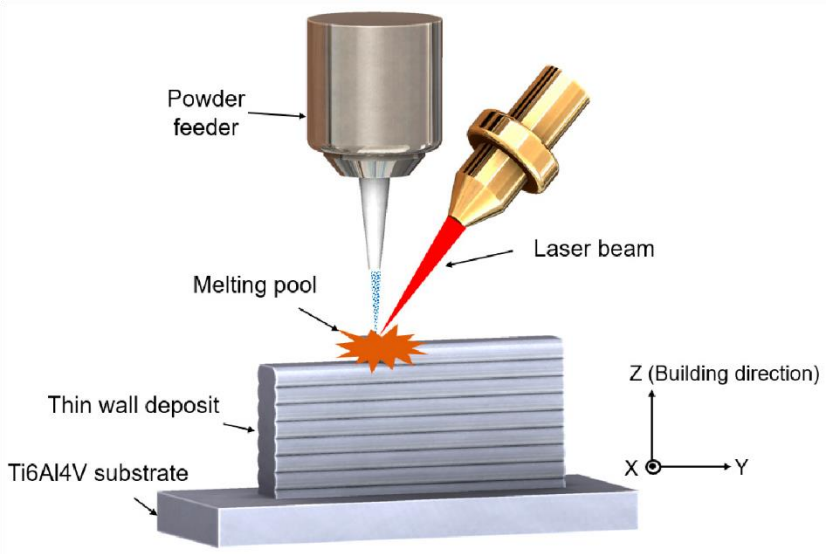

Figure 1.3. Schematic of the laser deposition process (Cui *et al*., 2020)

1.2.3. Wet chemical method

In wet chemical synthesis for nanoscale high entropy alloy production, metal salts are reduced or mixed in a specialized solution with capping agents to control crystal aggregation and growth. This synthesis method was employed by Liu *et al*. (2019) to create PtAuPdRhRu high entropy nanoparticles, yielding an average particle size of around 3 nm. The authors reported that these nanoparticles exhibited excellent electrocatalytic activities for hydrogen evolution reactions.

In 2020, Wang *et al.* introduced a groundbreaking wet chemical technique, referred to as a "droplet-to-particle" approach (Figure 1.4). This process involves incorporating a gas-blowing agent and transient high-temperature heating for producing hollow HEA NPs.

Figure 1.4. Schematic of the droplet-to-particle evolution for the synthesis of hollow HEA NPs (Wang *et al*., 2020)

Metal chloride salts were dissolved in ethanol, and citric acid was added as the blowing agent to create an aerosol stream containing extremely small particles with diameters as tiny as 1 m. These droplets were then transported through a tube furnace's heating zone by argon at a flow rate of 5 L/min, facilitating homogeneous mixing of up to eight different components in the HEA NPs.

1.2.4. Ultrasonic spray pyrolysis method

In the ultrasonic spray pyrolysis (USP) technique, a metal precursor solution or suspension is used to produce spherical particles. A USP setup consists of three main components. An ultrasonic atomizer, fitted with piezocrystals at its bottom, is connected to a heated tube which leads to a catchment device. Upon applying an electric current, the piezocrys-tals will vibrate at the same frequency as the applied electric frequency. The vibration is then transferred to the solution stored in the atomizer. Waves propagate through the liquid, with microcavitation being identified as the primary mechanism behind the formation of small droplets from the bulk liquid.

If they are sufficiently small, these droplets become suspended in the gas phase above the liquid, forming an aerosol. The fundamental concept of USP is illustrated in Figure 1.5.

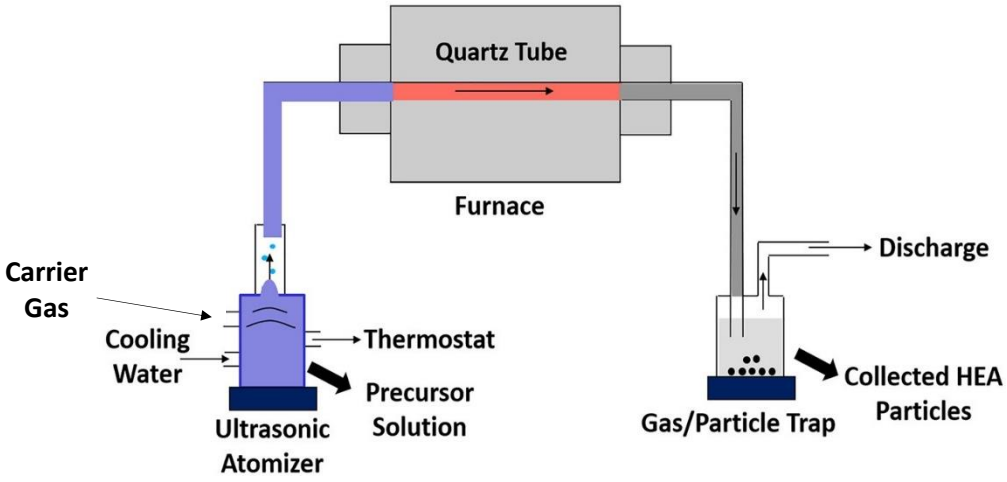

Figure 1.5. Schematic illustration of a USP apparatus [adapted from Küçükelyas *et al*. (2022)]

Within the furnace lies the reaction tube, which is connected at one end to wash bottles. In these bottles, the particles are suspended in deionized water or ethanol to maintain their structure (Toparli *et al*., 201; Muñoz-Fernandez *et al*., 2019; Küçükelyas *et al*., 2022).

Due to turbulence caused by the carrier gas bubbling into the bottles, the particles do not precipitate immediately. Some particles might be carried along with the flow out of the first bottle; hence, typically two or more wash bottles are employed to capture as much product as possible.

The aerosol is subsequently transported into the reaction tube by a carrier gas. This tube is externally heated by the furnace. Within the tube, a three-stage process occurs to transform particles from droplets. This process is illustrated in Figure 1.6. At elevated temperatures, the solvent evaporates, causing precipitation of the dissolved contents. These dehydrated particles undergo decomposition, resulting in the formation of hollow particles. Chemical reactions can also take place during this stage. The hollow particles then undergo a densification process, leading to the creation of solid particles. Due to the inherent nature of droplet formation, USP can generate spherical or nearly spherical particles (Stopić *et al*., 2006; Ebin and Gürmen, 2011). In the absence of densification, hollow or porous particles are produced (Bang and Suslick, 2010).

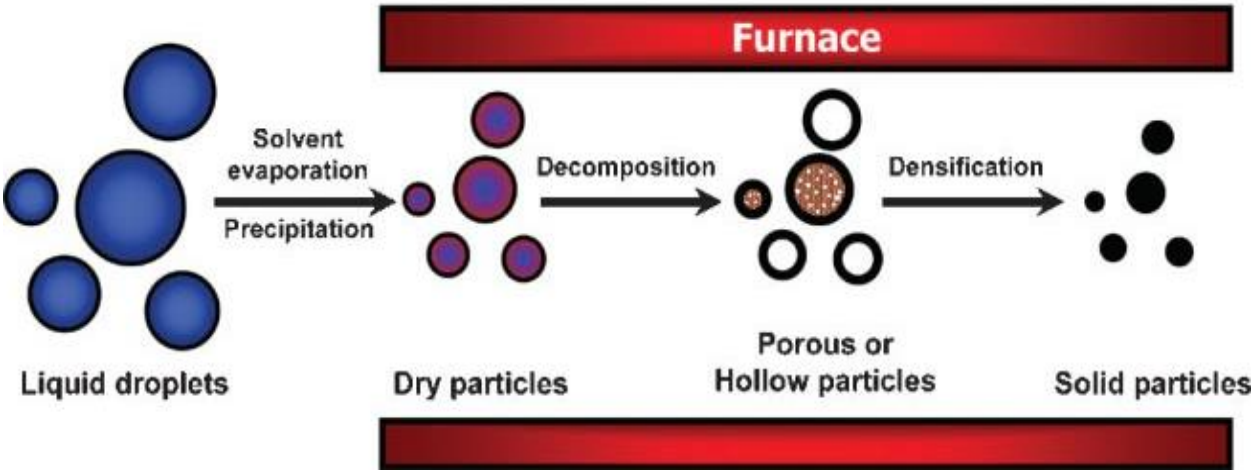

Figure 1.6. Simplified USP process (Bang and Suslick (2010)

The droplet size directly governs the resultant particle size, as elucidated in the preceding paragraph. The droplet size is affected by factors such as the piezo crystal frequency, solution density within the atomizer, and surface tension. Notably, greater surface tension results in larger droplets. On the other hand, elevated density yields smaller droplets, as heavier ones cannot be effectively suspended in the gas. In the context of water-based solutions, surface tension and density exhibit less variance, rendering their influence comparatively minor in contrast to the impact of frequency.

Increased frequency induces heightened turbulence and greater microcavitation within the solution, culminating in the emergence of smaller droplets from the bulk solution. The droplet size is given by Lang's equation (Eq. 1.4):

$$D = 0.34(8 \cdot \pi \cdot \gamma/\rho \cdot f^2)^{1/3} \quad \text{(Eq. 1.4)}$$

where D is the average droplet diameter (μm), γ is the surface tension of the solution (Nm^{-1}), ρ is the density of the solution (g/cm^3), and f is the frequency of the ultrasound (Hz).

The particle size is subsequently determined based on the initial droplet size, accounting for solvent evaporation and potential concurrent reactions. The relationship between droplet and particle sizes is expressed by the following equation (Eq. 1.5):

$$Dp = D(C_{precursor} M_{product}/M_{salt} \rho_{product})^{1/3} \quad \text{(Eq. 1.5)}$$

where D_p is the particle diameter, D is the droplet diameter, $C_{precursor}$ is the solution concentration, $M_{product}$ is the molar mass of the resultant product, M_{salt} is the molar mass of the metal salt, and $\rho_{product}$ is the density of the metal product.

In the USP process, both physical and chemical changes occur as droplets and particles pass through a heated tube. The time it takes for this journey of aerosol droplets inside the heating zone is known as residence time (T). By assuming that the droplets move with the gas flow and don't experience significant interactions, coagulation, or other complex behaviors, T can be calculated as follows (Eq. 1.6):

$$T = V_{tube}/\dot{V} = \pi \cdot r^2 \cdot l/\dot{V} \qquad \text{(Eq. 1.6)}$$

where $\dot{V}$ is the gas flow rate, r is the radius of the cylinder, and l is the length of the glass tube heated by the furnace.

1.3. Advantages and disadvantages of the methods

In addition to the previously mentioned methods, there certainly exist many other techniques for producing nanomaterials tailored for different applications, spanning a range of sizes, energy demands, and financial investments. The advantages and disadvantages of each synthesis category are listed in Table 1.1. Although there are other unique synthesis techniques, we can generally classify them into one of these categories: mechanical alloying, thermal spraying, physical vapor deposition, severe plastic deformation, electrodeposition, and USP.

USP is often preferred due to several distinct advantages it offers. However, there are also certain disadvantages associated with this method. Different nanoparticle synthesis methods have their strengths and weaknesses, and the choice of method depends on the specific requirements of the desired nanoparticles and their intended applications. Researchers and engineers evaluate factors like cost-effectiveness, production scale, material properties, and ease of implementation when selecting the most suitable synthesis method for their needs.

Table 1.1. Advantages and disadvantages of nanomaterial synthesis methods [adapted from Haché *et al*. (2020)]

Method	Advantages	Disadvantages
Mechanical alloying (Suryanarayana et al., 2001) Ball-milling and cryo-milling	• Scalable • No melting required • Allows alloying of normally immiscible elements	• Rapid grain growth upon consolidation of powders • Void formation on compaction and sintering • High energy input • High risk of contamination • Large variation in particle size
Thermal spraying (Kim et al., 2011) Plasma-spray, flame-spray, etc...	• High deposition rate • Near-net-shape coating technology • Scalable • No thickness limitations	• Voids and constrained geometry • High equipment cost • High energy input • Nonuniform grain-size distribution
Physical vapor deposition (Koch, 2007; Swann, 1988) Gas condensation, DC/RF sputtering, vacuum arc deposition	• Wide range of materials can be synthesized • Good control of cluster sizes • Continuous process, and excellent uniformity • Low risk of contamination • Low thermal load to substrate • High coating density and adhesion	• Void formation upon compaction and sintering of vapor-deposited powders • High cost (need ultra-high vacuum) • Difficult to scale up (low yield) • Requires vacuum environment • Limited to thin films
Severe plastic deformation (Valiev, 2011) High-pressure torsion, equal channel angular pressing	• Straightforward relationship between strain and grain size • Simple grain-refinement mechanism	• Small-scale • Constrained geometry • Poor efficiency • High waste
Electrodeposition (Erb, 1995)	• Low initial capital investment, cost, and energy requirements • Scalable, and few size or shape limitations • Can obtain uniform grain sizes	• Difficult to co-deposit multiple elements • Constrained by certain elements • Significant internal stresses can be built up in the material
Ultrasonic spray pyrolysis	• Low-cost, scalable, and continuous process • High purity, finite, and spherical grain • Uniform particle size distribution	• Increase in processing time • Precursor volatility

1.4. Direct hydrogen reduction

1.4.1. Why use hydrogen as the reducing agent?

In addition to the USP method or other techniques, the selection of a suitable and eco-friendly reducing agent for the synthesis of nanoparticles is a crucial measure to decrease the substantial carbon dioxide (CO_2) emissions in the metallurgical industry.

The metallurgical industry is a significant contributor to global CO_2 emissions, primarily due to its intensive energy consumption and reliance on carbon-rich materials in various production processes. CO_2 emissions from the metallurgical sector stem derived from activities such as iron and steelmaking, aluminum production, and other metal extraction processes. These emissions have significant environmental and climate implications, making it a crucial area of focus for emission reduction strategies. Iron and steelmaking, in particular, is a major source of CO_2 emissions within the metallurgical industry. The traditional blast furnace (BF)/basic oxygen furnace (BOF) method used in steel production involves the reduction of iron ore using carbon-rich materials like coal or coke. This process releases substantial amounts of CO_2 into the atmosphere, both from the combustion of fossil fuels and the chemical reactions involved (Figure 1.7).

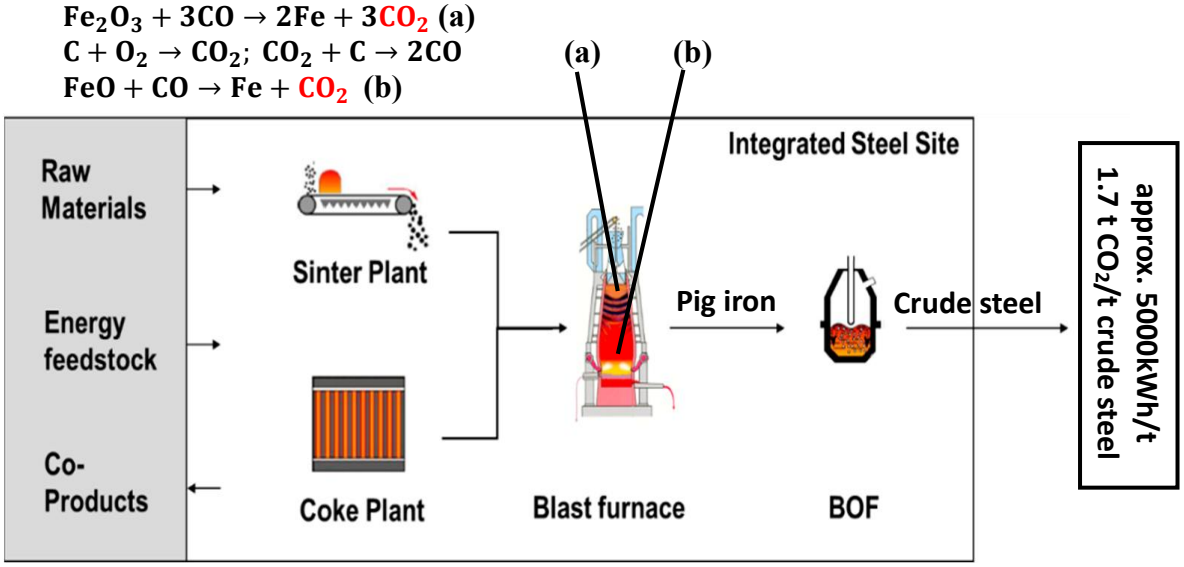

Figure 1.7. Schematic of a steel site using coal or coke reducing agents [adapted from Suer *et al.* (2022)]

Efforts to reduce these CO_2 emissions often focus on developing more sustainable and efficient production methods. This includes exploring alternative reducing agents, like hydrogen, as well as adopting advanced technologies and processes that can minimize carbon emissions.

In contrast to the indirect reduction (IR) of iron ore using coal or coke in a blast furnace to produce an intermediate pig iron product, direct reduction (DR) is a one-step process that directly converts iron ore into metallic iron without the need for an intermediary step. This process typically involves using a reducing agent (such as natural gas or hydrogen) in an electric arc furnace (EAF) to directly reduce iron oxide at elevated temperatures. DR processes are generally more efficient and have a lower environmental impact compared to traditional BF methods because they produce less CO_2 emissions. The reducing agent reacts with iron oxide, extracting oxygen and leaving behind metallic iron (Fe). When hydrogen is used, water (H_2O) is produced instead of CO_2 as the direct by-product (Spreitzer and Schenk, 2019), as shown in Figure 1.8. Furthermore, utilizing hydrogen from renewable sources in industrial applications offers numerous environmental, economic, and societal benefits.

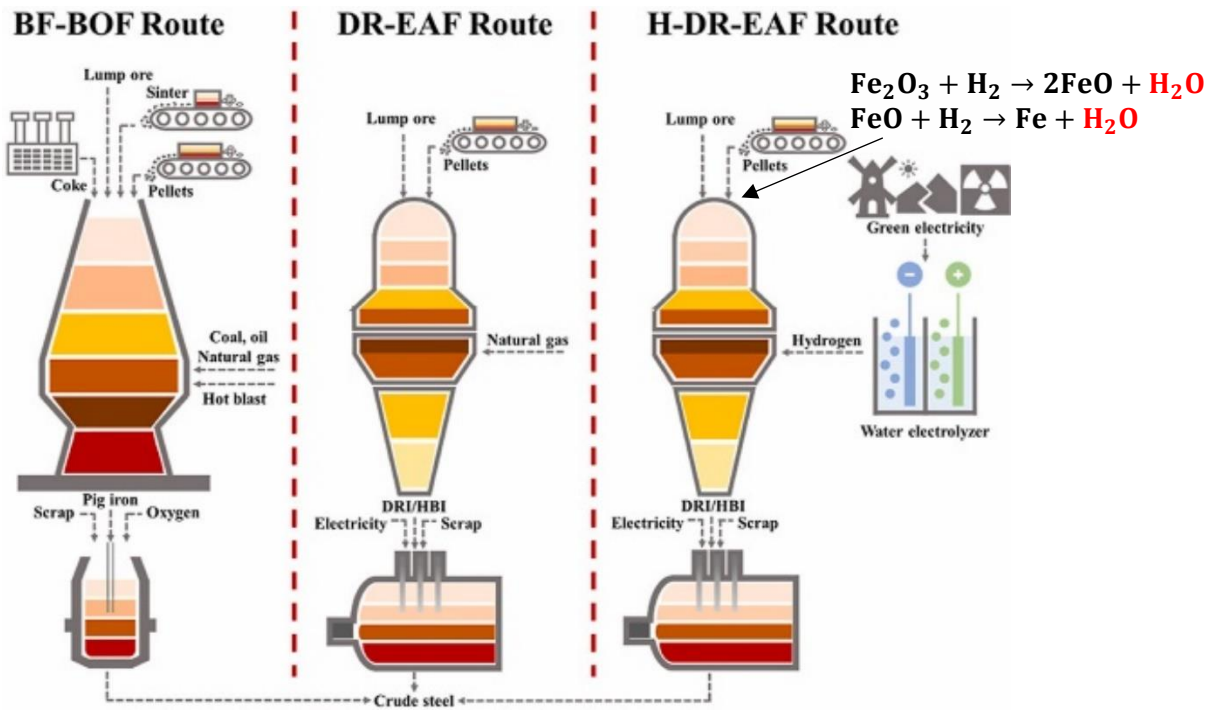

Figure 1.8. Hydrogen-based route to steel compared to coal and natural gas-based routes [adapted from Wang et al. (2021)]

At the nanoscale, the significance of utilizing hydrogen as the reducing agent remains as pronounced as it is in bulk materials. Nanomaterials even exhibit unique interesting properties which cannot be found in bulk materials, holding great promise for a wide range of applications.

1.4.2. Thermodynamic analysis of hydrogen reduction

The process of hydrogen reduction for nanoparticle synthesis typically involves exposing precursor materials to hydrogen gas at elevated temperatures. The hydrogen molecules interact with the precursor molecules, causing reduction reactions that lead to the formation of nanoparticles. Thermochemical analysis focuses on calculating the change in enthalpy (ΔH°) and Gibbs free energy (ΔG°), which helps us understand the feasibility and effectiveness of the synthesis process. This also guides researchers in making informed decisions about reaction conditions, precursor materials, and process parameters to achieve desired nanoparticle characteristics while minimizing energy consumption and waste.

In this subsection of the review, we will delve into the thermodynamic facets related to the thermal decomposition of materials used in the experimental section and the subsequent hydrogen reduction of the resulting oxides, drawing insights from existing literature.

1.4.2.1. For the formation of the AgCoCuFeNi HEA NPs

For the formation of the AgCoCuFeNi HEA NPs, by applying heat, reactions like those shown in Eqs 1.7 to 1.11 occur, leading to the formation of metal oxides evenly distributed within the mixture.

$$2AgNO_3(s) \rightarrow 2Ag(s) + 2NO_2(g) + O_2(g) \quad \text{(Eq. 1.7)}$$

$$2Co(NO_3)_2 \cdot 6H_2O(s) \rightarrow 2CoO(s) + 6H_2O(g) + 4NO_2(g) + O_2(g) \quad \text{(Eq. 1.8)}$$

$$2Cu(NO_3)_2 \cdot 3H_2O(s) \rightarrow 2CuO(s) + 3H_2O(g) + 4NO_2(g) + O_2(g) \quad \text{(Eq. 1.9)}$$

$$2Fe(NO_3)_3 \cdot 9H_2O(s) \rightarrow Fe_2O_3(s) + 9H_2O(g) + 6NO_2(g) + \frac{3}{2}O_2(g) \quad \text{(Eq. 1.10)}$$

$$Ni(CH_3CO_2)_2 \cdot 4H_2O(s) \rightarrow NiO(s) + 3H_2O(g) + 2CH_3COOH(g) \quad \text{(Eq. 1.11)}$$

The possibility of thermodynamically reducing the metal salts using hydrogen can also be studied by the computation of the Gibbs free energy as a function of temperature (Figure 1.9). The hydrogen reduction reactions for the formation of metallic (Ag, Co, Cu, Fe, and Ni) NPs from the metal salts can be described in the following equations (Eqs. 1.12 – 1.16):

$$AgNO_3(s) + H_2(g) = Ag(s) + H_2O(g) + NO_2(g) \quad \text{(Eq. 1.12)}$$

$$Co(NO_3)_2(s) + 2H_2(g) = Co(s) + 2H_2O(g) + 2NO_2(g) \quad \text{(Eq. 1.13)}$$

$$Cu(NO_3)_2(s) + 2H_2(g) = Cu(s) + 2H_2O(g) + 2NO_2(g) \quad \text{(Eq. 1.14)}$$

$$Fe(NO_3)_3(s) + 3H_2(g) = Fe(s) + 3H_2O(g) + 3NO_2(g) \quad \text{(Eq. 1.15)}$$

$$Ni(CH_3CO_2)_2(s) + H_2(g) = Ni(s) + H_2O(g) + CH_3COCH_3 + CO_2(g) \quad \text{(Eq. 1.16)}$$

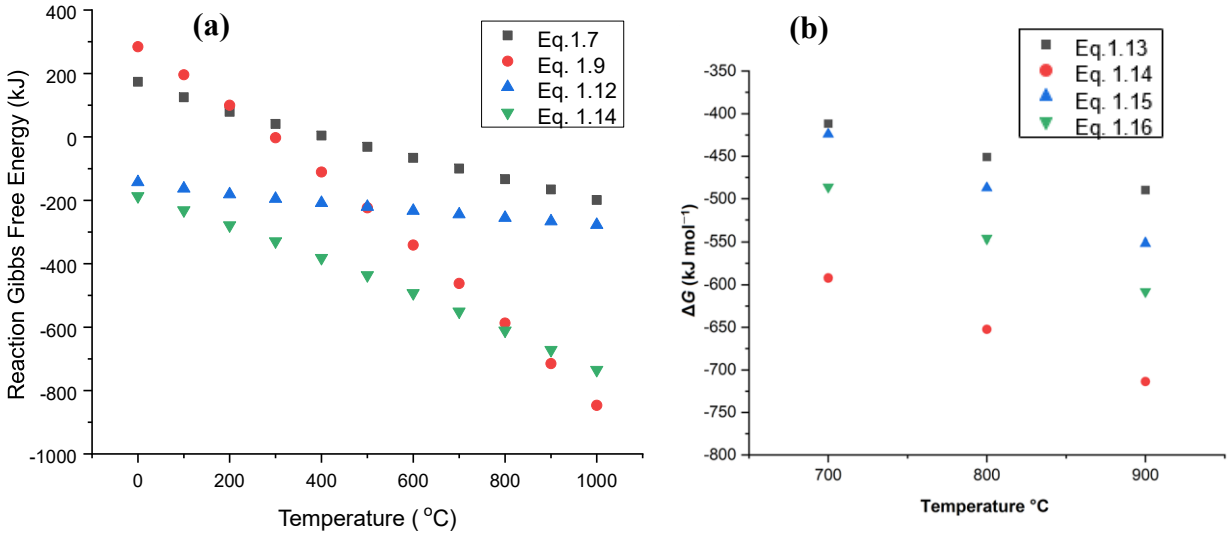

Figure 1.9. Gibbs free energy change for the hydrogen reduction of (a) silver and copper nitrates [Adapted from Köroğlu *et al*. (2021)], (b) cobalt and iron nitrates, and nickel acetate [adapted from Küçükelyas *et al*. (2022)]

As shown in Figure 1.10, the values of Gibbs free energy (ΔG°) for Eqs. 1.12 – 1.16 are negative within the temperature range of 600 – 1000 °C, indicating that hydrogen reduction of the corresponding metal salts to Ag, Co, Cu, Fe, and Ni is thermodynamically possible.

1.4.2.2. For the formation of Fe-Si NPs: inhibitory effect of Si

As far as the formation of Fe-Si NPs is concerned, only the direct reduction of iron from iron oxide can be performed by hydrogen gas, as proved in the previous Eq. 1.15. Itaka *et al*. (2015) examined in their research the Ellingham Diagrams for hydrogen reduction and carbon-carbon monoxide reduction processes (illustrated by red lines) involving iron, silicon, titanium, and aluminum (Figure 1.10). They found that the line of the hydrogen reduction intersects only with the iron curve, while the line of the carbon-carbon monoxide reduction intersects with the silicon curve. This implies that hydrogen gas cannot directly reduce silicon (Si) from silica (SiO_2).

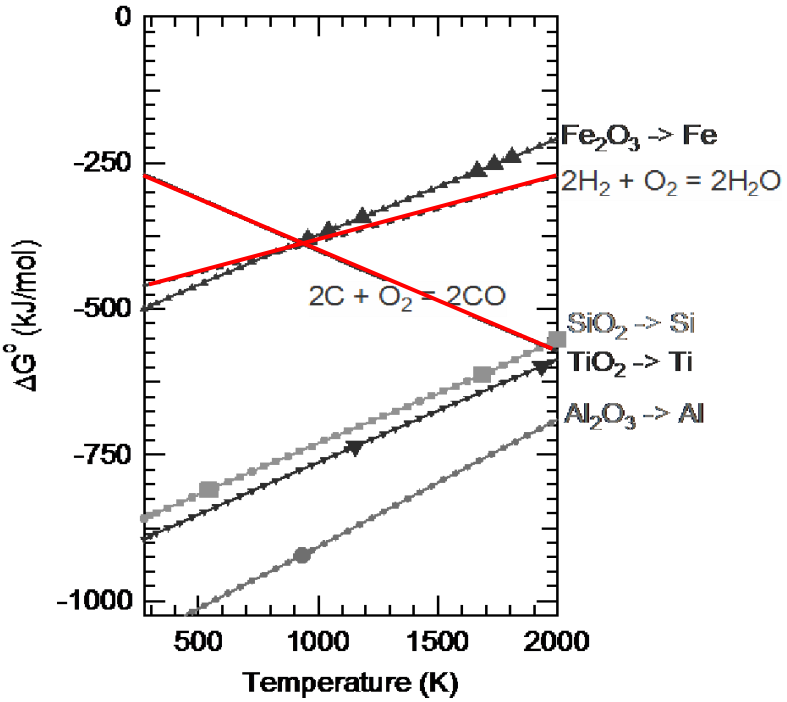

Figure 1.10. Ellingham Diagrams of iron, silicon, titanium, and aluminum in the H-reduction and C-C monoxide reduction (Itaka *et al*., 2015)

Silica (SiO_2), being a stable and inert compound under normal conditions, its direct reaction with H_2 to produce silicon (Si) is not thermodynamically favored at ordinary temperatures and pressures. However, at very high temperatures and under specific conditions, SiO_2 can undergo a reduction reaction with hydrogen to form silicon monoxide (SiO), as demonstrated in the following equation:

$$SiO_2(s) + H_2(g) = SiO(s) + H_2O(g) \qquad \text{(Eq. 1.17)}$$

Regarding the hydrogen reduction of iron oxide (Fe_2O_3) resulting from the thermal decomposition of iron nitrate, it can also be noticed that intermediate iron oxide products may be generated (prior to the metallic iron) depending on the temperature imposed. In their study on the formation of Fe-Ni by hydrogen reduction, Avalo *et al*. (2014) assessed the thermodynamic feasibility of using hydrogen to reduce Fe_2O_3 by calculating the equilibrium mole fraction of H_2 at different temperatures (Figure 1.11). At lower temperatures (~ below 600 °C), the reduction of Fe_2O_3 by hydrogen is less thermodynamically favorable, and the reaction rate might be relatively slow. The primary product under these conditions is likely to be Fe_3O_4 with water as a by-product. In the intermediate temperature range of ~ 600 – 800 °C, the thermodynamic favorability of the reduction process increases. The main product becomes FeO. The extent of reduction to metallic iron becomes more substantial compared to lower temperatures. At elevated temperatures (~ 800 – 1200 °C), the reduction of Fe_2O_3 by hydrogen becomes highly thermodynamically favorable. The primary product is almost exclusively metallic iron (Fe). Water continues to be released as a byproduct of the reaction. The reduction process is more complete, and the yield of metallic iron is maximized at high temperatures.

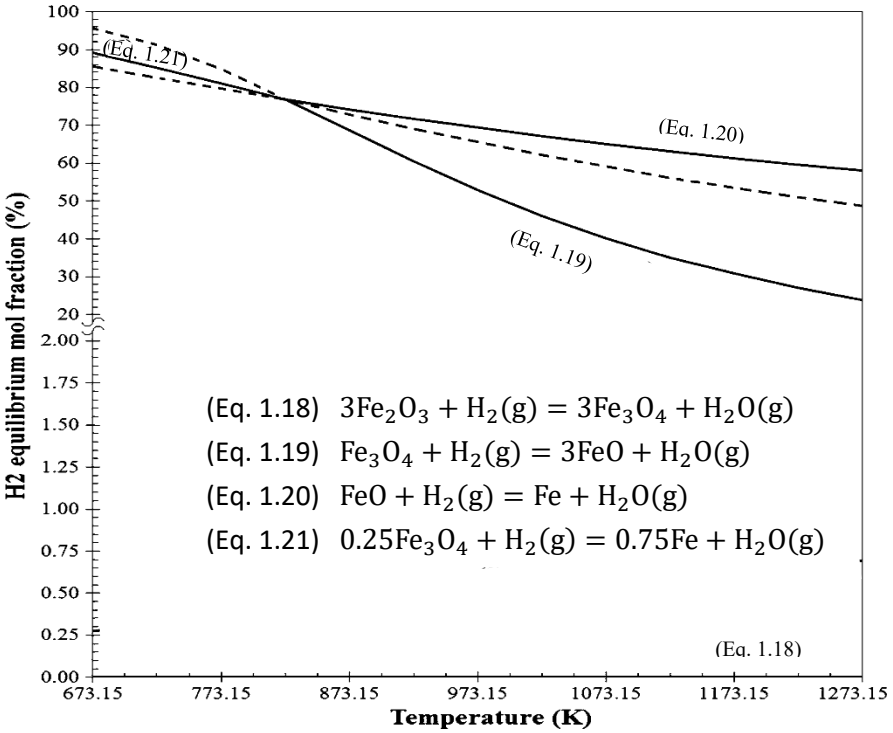

Figure 1.11. Equilibrium mole fraction of hydrogen as a function of temperature for iron oxide reduction [adapted from Avalo et al. (2014)]

Furthermore, Patterer *et al*. (2023) studied the effect of Si on the hydrogen-based direct reduction of Fe_2O_3 at 700 °C through sputter deposition. They reported that the doping of a relatively low amount of Si (e.g., 3.7 at.%) significantly inhibits the hydrogen reduction process of Fe_2O_3 at 700 °C. This inhibition occurs due to the creation of a layer enriched with SiOx in the surface-near region. As a result, the progress of reduction is locally halted by blocking free surfaces of iron oxide, and thus, hindering the direct interactions with reducing agents (Figure 1.12).

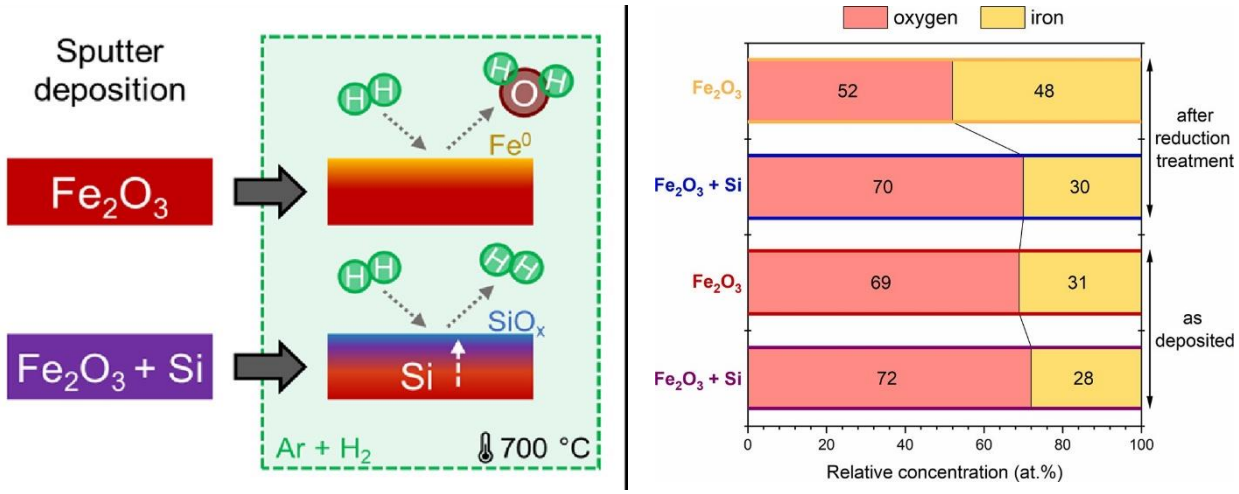

Figure 1.12. Mechanism behind the inhibition of hydrogen reduction of Fe_2O_3 by Si (Patterer *et al*., 2023)

1.4.2.3. For the formation of Fe-Pt NPs: hydrogen spillover effect

The thermodynamic analysis of hydrogen reduction for the formation of metallic platinum (Pt) from platinum (IV) nitrate [$Pt(NO_3)_4$] is not well-documented in the literature. However, many researchers have studied the catalytic effect of Pt on the hydrogen reduction of iron oxide.

Platinum is a highly effective catalyst which provides an alternative reaction pathway with lower activation energy, enabling reactions to occur more readily and at lower temperatures (Miller *et al*., 1996). In contrast to silicon which blocks the iron oxide free surfaces, platinum provides active sites on its surface where hydrogen molecules can adsorb, dissociate into atomic hydrogen species, and react more readily with the iron oxide (Spreafico *et al*., 2017; Karim *et al*., 2017; Meng *et al*., 2019).

This mechanism, known as the hydrogen spillover effect (Figure 1.13), facilitates the breaking of chemical bonds within the iron oxide, promotes the reduction reaction, reduces the activation energy, and lowers the temperature at which hydrogen reduction takes place (Lin *et al*., 1993; Rioux *et al*., 2005). Therefore, even at low temperatures, FeO or metallic iron Fe could be directly formed from the hydrogen reduction of Fe_2O_3.

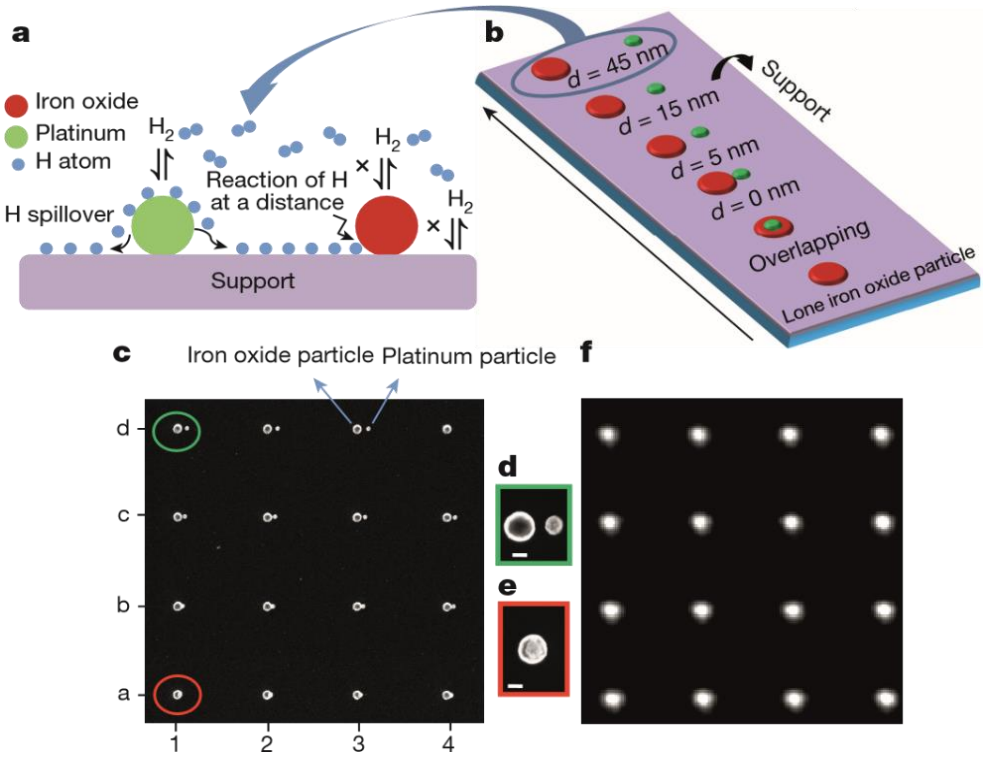

Figure 1.13. Hydrogen spillover effect during Fe-Pt particle synthesis (Karim *et al*., 2017)

1.5. Applications of Fe-Si, Fe-Pt, and AgCoCuFeNi nanopowders

Nanomaterials exhibit unique interesting properties which cannot be found in bulk materials, holding great promise for a wide range of applications. They play a crucial role in electronics, biomedical, and particularly in catalysis fields, enabling the creation of smaller and more efficient devices, enhancing chemical reactions, and revolutionizing drug delivery and medical imaging (Shokouhmand *et al*., 2008; Jones *et al*., 2008; Xie and Chen 2009; Liu *et al*., 2009). In the energy sector, nanomaterials contribute to the improvement of batteries, efficient energy conversion, and materials reinforcement (Tyagi *et al*., 2009; Wu *et al*., 2010; Otanicar *et al*., 2010). In environmental applications, they are employed in water purification, pollutant sensing, and the

enhancement of coatings (Vassallo *et al*., 2004). Nanomaterials also have applications in textiles, aerospace, agriculture, cosmetics, and various other fields (Kim *et al*., 2007).

Particularly, Fe-Si nanoparticles excel in magnetic technology, where they contribute to the development of high-performance magnets for electronics, motors, and generators (Park *et al*. 2013; Tabasi *et al*., 2021); in catalysis, where they serve as catalysts in chemical reactions, speeding up processes like hydrogenation and oxidation; and in biomedical imaging, where they act as contrast agents, enhancing the quality of magnetic resonance imaging (MRI) scans (Dutta *et al*., 2018). Fe-Pt nanoparticles are extensively used as catalysts in various chemical reactions (especially in hydrogen evolution reaction) due to their high catalytic activity and ability to enhance reaction rates and selectivity. They also find significant use in biomedical imaging and therapy, including magnetic resonance imaging (MRI) contrast agents and targeted drug delivery systems. In magnetic storage, Fe-Pt nanoparticles contribute to the development of high-capacity and high-density storage devices (Sun *et al*., 2000; O'Connor *et al*., 2001; Stahl *et al*., 2003).

However, the utilization of noble metal and noble metal-based oxide catalysts (such as Pt, RuO_2, and IrO_2), along with traditional alloy catalysts (like Fe-Pt, Pt-Ni, CuPdAu), in largescale applications, is hindered by their high costs, limited natural resources, and scarceness (Kim *et al*., 2018). This creates a strong incentive to innovate and fabricate electrocatalysts that are cost-effective, exceptionally efficient, and easily accessible, surpassing the catalytic performance of noble metals and conventional alloys (Wang *et al*., 2019; Yan *et al*., 2019; Feng *et al*., 2020). This leads again to the importance of HEAs in catalytic applications such as hydrogen evolution reaction (HER), oxygen reduction reaction (ORR), oxygen evolution reaction (OER), CO_2 reduction reaction (CO_2RR), and ammonia (NH_3) decomposition (Modupeola and Popoola, 2023). In their study on the synthesis of CoCuFeNi particles by hydrogen reduction-assisted ultrasonic spray pyrolysis (USP-HR), Küçükelyas *et al*. (2022) found that these particles exhibited high ferromagnetic behavior, making them promising materials for catalytic applications. Also, silver (Ag) nanoparticles, due to their unique properties and high surface area, have often been used as catalysts in catalytic processes. In 2022, Köroğlu and his co-workers demonstrated that AgCu nanoparticles could be used as antibacterial agents in various areas because they completely eliminated bacteria. The AgCoCuFeNi HEA NP combination could therefore serve as highly effective catalysts.

1.6. Characterization of nanomaterials

The main primary techniques used to analyze nanopowders include scanning electron microscopy (SEM), energy-dispersive X-ray spectroscopy (EDS), and X-ray diffraction (XRD). Table 1.2 below provides a summary of the characterization methods along with the intent pursued in each of them.

Table 1.2. Characterization tools for investigating the properties of nanomaterials [adapted from Modupeola and Popoola (2023)]

Characterization	**Objective**
Scanning Electron Microscopy (SEM) or Transmission Electron Microscopy (TEM)	Determines the particle shape and size distributions
Energy-Dispersive X-ray Spectroscopy (EDS)	Determines the elemental composition of individual particles
X-ray diffraction (XRD)	Investigates the phase analysis
Electron Probe Microanalysis (EPMA)	Quantifies each component
Inductively Coupled Plasma Mass Spectrometry (ICP-MS)	Detects the elements at milligram to nanogram and estimates the trace contamination level
X-Ray Photoelectron Spectroscopy (XPS), Atomic Emission Spectroscopy (AES), Operando X-Ray Absorption Near Edge Spectroscopy (XANES), Analysis of the Extended X-Ray Absorption Fine-Structure (EXFAS), and Surface Plasmon Resonance (SPR) Spectroscopic analysis	Investigates the surface chemistry, binding energy, and oxidation state
Density Functional Theory (DFT) Calculation and Molecular Dynamics Simulations	Determines the physical movements
Cyclic Voltammetry	Probes the redox potential of the catalyst system and the oxidation-reduction rates
Chronoamperometry	Examines the catalyst stability and the current changes during reaction

Conclusion

Although a lot of work has been done on the preparation of conventional iron alloy nanoparticles (NPs) such as Fe-Si and Fe-Pt NPs, there are only a few reports studying the effects of silicon (Si) and platinum (Pt) on the hydrogen-based direct reduction of iron oxide (Fe_2O_3) nanoparticles, particularly those generated via ultrasonic spray pyrolysis (USP). Likewise, while various high entropy alloy (HEA) NPs have been prepared through diverse methods, the combination of AgCoCuFeNi alloy and its particle synthesis using the hydrogen reduction-assisted ultrasonic spray pyrolysis (USP-HR) technique have not been explored. Furthermore, the effect of processing parameters on the synthesized AgCoCuFeNi HEA NPs needs to be investigated through characterization techniques in order to enhance the properties of the HEA NPs. Hence, keeping this research gap in mind, this thesis tries to study the hydrogen reduction behavior of Fe_2O_3 in the absence and presence of additives (SiO_2 or Pt), and the microstructural variation of AgCoCuFeNi NPs with change in synthesis parameters, using the USP-HR method.

CHAPTER 2.
METHODOLOGY

CHAPTER II. METHODOLOGY

Introduction

All the performed experiments were done in the hydrometallurgical laboratory of the Institute of Process Metallurgy and Metal Recycling (IME) at RWTH Aachen University, Germany.

Located in Central Europe, Germany is the seventh-largest country by area in the continent and the second-most populous country in Europe after Russia. Based on Worldometer elaboration of the United Nations data, the population of Germany was about 84.5 million in July 2023 (Worldometer, 2023). The territory covers 357,022 km^2 between latitude 51° N and longitude 9° E. The country shares its borders with nine other countries: Denmark in the north, Poland and the Czech Republic in the east, Austria and Switzerland in the south, France and Luxembourg in the south-west, and Belgium and the Netherlands in the north-west (CIA, 2023). The Institute of Process Metallurgy and Metal Recycling is in the north-western part of the city of Aachen, street Intzestraße 3, 52072 (Figure 2.1). It belongs to the Faculty of Georesources and Materials Engineering of RWTH Aachen University.

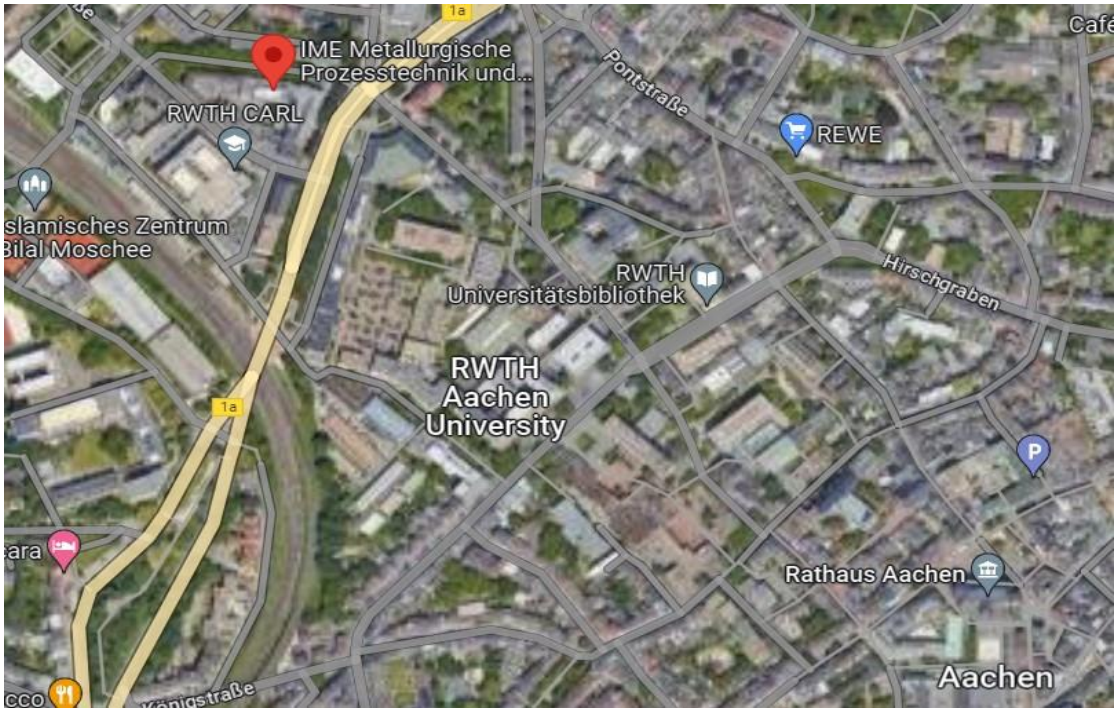

Figure 2.1. Geographical location of IME (Google Maps)

2.1. Materials

Seven different reagents were used as starting materials for the preparation of the precursor solutions: colloidal silica (40 wt. % of SiO_2), platinum nitrate solution ($N_4O_{12}Pt$, 15 wt. % of Pt), iron nitrate nonahydrate [$Fe(NO_3)_3 \cdot 9H_2O$], copper nitrate trihydrate [$Cu(NO_3)_2 \cdot 3H_2O$], cobalt nitrate hexahydrate [$Co(NO_3)_2 \cdot 6H_2O$], silver nitrate ($Ag\ NO_3$) and nickel acetate tetrahydrate ($C_4H_6O_4Ni \cdot 4H_2O$). All the chemicals were purchased from Sigma-Aldrich company and used as received without further purification because of their analytical grade (≥99% pure).

2.2. Precursor preparation

2.2.1. For traditional alloy: doping of Fe_2O_3

Three precursor solutions of the same concentration (0.5 mol/L) and volume (400 mL) were prepared by dissolving 80.8 g of iron nitrate in deionized water and stirred for 30 min using a magnetic stirrer. Two of the solutions were mixed with 10 mL of SiO_2 (40 wt. %) and 5 mL of Pt (15 wt. %) respectively, while the third one was left undoped (Figure 2.2).

(a) **(b)** **(c)**

Figure 2.2. Precursor solution of (a) undoped Fe_2O_3, (b) Si-doped Fe_2O_3, (c) Pt-doped Fe_2O_3

2.2.2. For AgCoCuFeNi high entropy alloy

An initial aqueous solution (0.5 mol/L, 1 L) was prepared by dissolving an equimolar amount of 0.2 mol of iron nitrate, cobalt nitrate, copper nitrate, silver nitrate, and nickel acetate in deionized water. Afterward, this solution was stirred for 1 h and diluted three times {S_1(1:1), S_2(1:4), and S_3(1:9)} to obtain three precursor solutions with different concentrations (Figure 2.3).

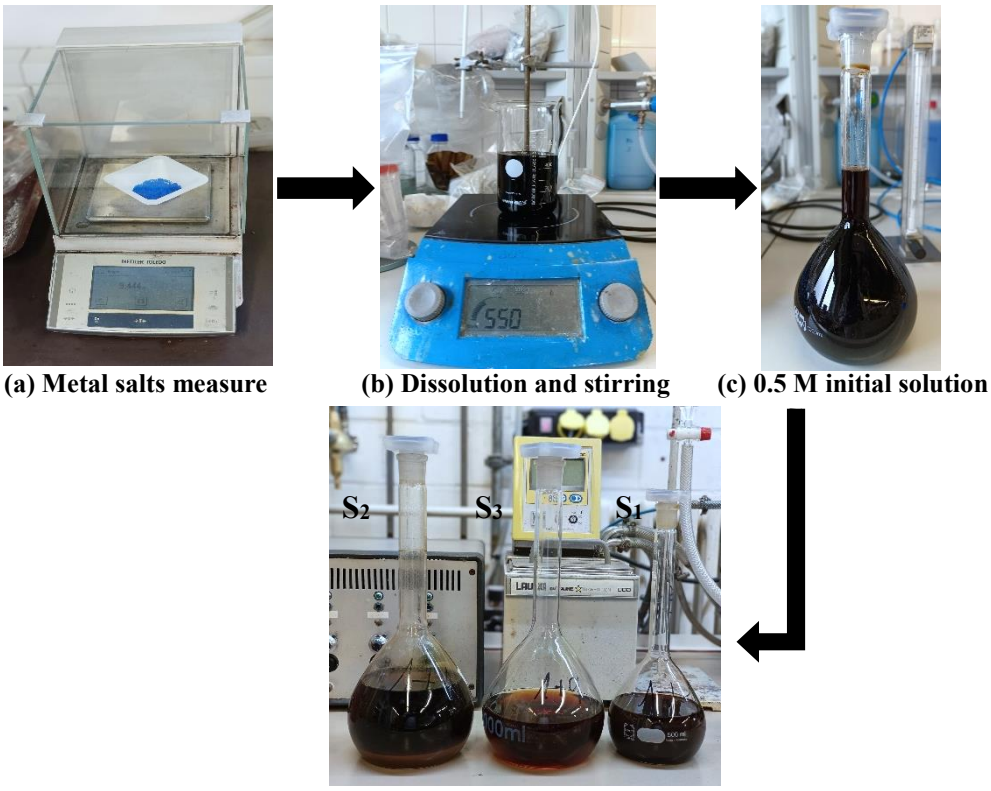

(a) Metal salts measure **(b) Dissolution and stirring** **(c) 0.5 M initial solution**

(d) Diluted solutions S_1 (0.25 M), S_2 (0.1 M), S_3 (0.05 M)

Figure 2.3. Preparation steps of AgCoCuFeNi HEA precursor solutions

2.3. Hydrogen reduction-assisted ultrasonic spray pyrolysis technique

Fe, Fe-Si, Fe-Pt, and AgCoCuFeNi HEA NPs were synthesized by the USP-HR method using their respective precursor solutions at different temperatures. Firstly, low-temperature equipment (Thermostar, max. 1000 °C) was used to produce the simple and complex alloy NPs. Secondly, experiments were performed only on the complex alloy (AgCoCuFeNi) system using a high-temperature setup (Carbolite, max. 1300 °C) to investigate the effect of residence time on the particle microstructure.

In both cases, the basic setup consisted of gas bottles, a rotameter, a thermostat or cooling system, an ultrasonic atomizer (with three transducers) connected to a frequency generator, a silica or alumina tube heated by the furnace(s), two wash bottles with deionized water for nanoparticle collection, and a gas exhaust pipe.

2.3.1. Synthesis of Fe and AgCoCuFeNi alloy nanoparticles via low-temperature setup

The low-temperature setup was characterized by a silica glass tube passing through two combined small furnaces (Figure 2.4). The synthesis method is the same regardless of the type of precursor solution used in the atomizer. The experiment began with setting the furnace temperature followed by loading the precursor solution through a funnel to a certain level of the atomizer. The solution was then nebulized at a frequency of 1.7 MHz into aerosol droplets under a gas flow rate of 3 L/min. To prevent the transducers from being damaged, the nebulizer temperature was controlled and cooled each time to 23 °C with water from the thermostat. The droplets were transported by the gas mixture into the horizontal tubular reactor. Hydrogen was especially used as a reducing agent at 2 L/min gas flow rate but also carried some of the droplets into the reactor. Argon with 1 L/min flow rate was used to maximize the transport of the aerosol droplets into the reactor. For safety reasons, argon was also used, before and after each experiment, to flush the quartz tube inside the furnaces to create an inert atmosphere conducive to the use of hydrogen.

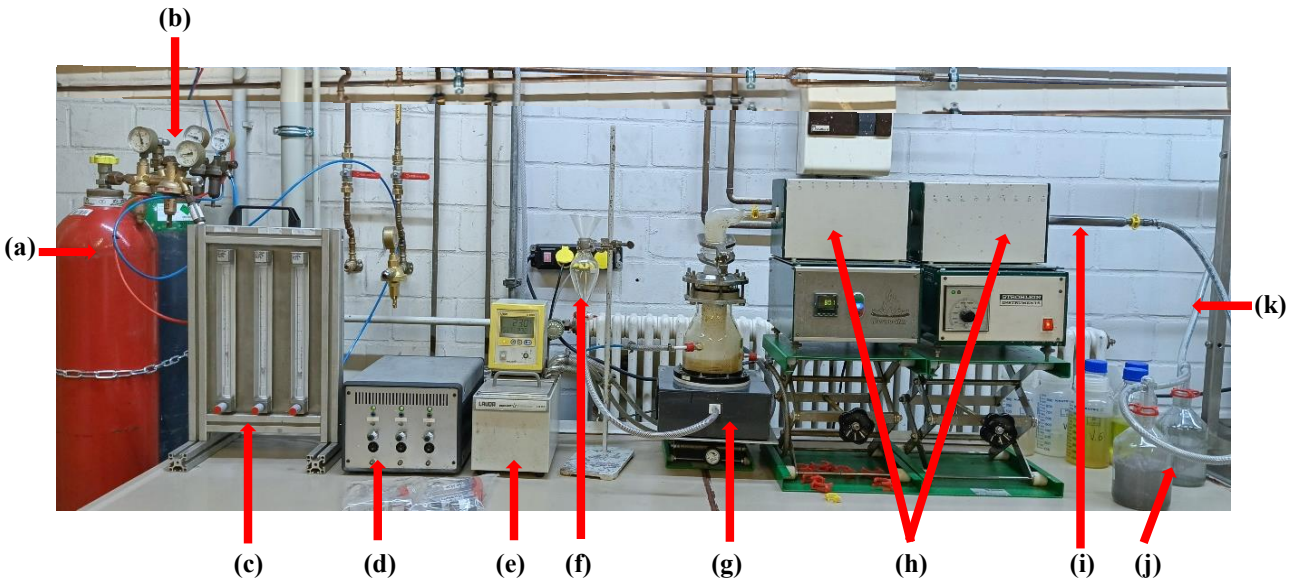

Figure 2.4. Thermostar setup for USP-HR technique with (a) hydrogen and (b) argon gas bottles, (c) rotameter, (d) transformer, (e) thermostat, (f) funnel (precursor input), (g) atomizer, (h) small furnaces, (i) silica tube, (j) wash bottles, (k) exhaust gas.

Water evaporation, decomposition, and densification of droplets happened consecutively in the quartz tube heated by the electrical furnaces to form the NPs. The total length of the silica tube is 83 cm with an inner diameter of 2.35 cm. Of this total length, 61 cm was heated by the furnaces and 11 cm at each end of the tube was unheated.

Knowing the gas flow rate (3 L/min) and the geometry of the tubular reactor, the residence time was determined using Eq. 1.6. The calculated T is ~5.3 s. So, the residence time for aerosol droplets passing through the heating zone of the small tubular reactor was about 5.3 s.

After the completed reduction process, the obtained nanopowders were collected in the wash bottles connected to the outlet of the reactor, and the exhaust gases were vented to the outside atmosphere through a pipe. The operating time for each experiment was 2 h. The details of the low-temperature experimental parameters for the synthesis of Fe-alloy and AgCoCuFeNi HEA NPs are given in Tables 2.1 and 2.2, respectively.

As stated earlier, the maximum temperature to be set using the low-temperature equipment is 1000 °C, as the silica glass tube cannot withstand furnace temperatures above 1050 °C. Moreover, the reaction time of aerosol droplets in small furnaces is also relatively short due to the short residence time, while the synthesis of spherical AgCoCuFeNi NPs requires a longer residence time or a large furnace with an adapted glass tube. For that purpose, a Carbolite furnace with an alumina glass tube was used.

Table 2.1. Parameters used for the synthesis of Fe-alloy NPs

No.	Precursor solution	Concentration (mol/L)	Temperature (°C)	H2 flow rate (L/min)	Ar flow rate (L/min)	Ultrasonic frequency (MHz)
1	Undoped Fe_2O_3	0.5	700	2	1	1.7
2	Undoped Fe_2O_3	0.5	950	2	1	1.7
3	Si-doped Fe_2O_3	0.5	700	2	1	1.7
4	Si-doped Fe_2O_3	0.5	950	2	1	1.7
5	Pt-doped Fe_2O_3	0.5	700	2	1	1.7

Table 2.2. Parameters used for the synthesis of AgCoCuFeNi NPs in the low-temperature setup

Solution	No.	Concentration (mol/L)	Temperature (°C)	H2 flow rate (L/min)	Ar flow rate (L/min)	Ultrasonic frequency (MHz)
S_1	6	0.25	600	2	1	1.7
	7	0.25	700	2	1	1.7
	8	0.25	800	2	1	1.7
	9	0.25	900	2	1	1.7
S_2	10	0.1	600	2	1	1.7
	11	0.1	700	2	1	1.7
	12	0.1	800	2	1	1.7
	13	0.1	900	2	1	1.7
S_3	14	0.05	600	2	1	1.7
	15	0.05	700	2	1	1.7
	16	0.05	800	2	1	1.7
	17	0.05	900	2	1	1.7

2.3.2. Synthesis of AgCoCuFeNi nanoparticles via high-temperature setup

The precursor solution homogeneity is necessary for obtaining nanoparticles with uniform size and shape. Due to the unexpected formation of solid residues in the first and second precursor solutions (S_1 and S_2) over time, only the third, more diluted solution S_3 with a concentration of 0.05 mol/L, was used as the starting material in the large furnace setup (Figure 2.5).

The AgCoCuFeNi nanoparticle synthesis method is the same in the Thermostar and Carbolite apparatus, except that the latter is automated equipment (start and end time of the experiment, cooling system, and furnace temperature) with a large furnace. There are also differences in the settings. The large furnace heats up and cools down slower than the small one. The heating rate of the small furnace is about 900 °C/h while that of the large furnace is programmed at 300 °C/h. The large furnace should be left to cool to 500°C before safely switching it off. This excessively prolongs the total duration of the experiment by approximately 3 h, which is more than the operating or reaction time (2 h).

The residence time of droplets in the large tubular reactor was also calculated, knowing that the gas flow rate is the same (3 L/min), the furnace length (95 cm) equals the heating zone length, and the inner diameter of the alumina tube is 4 cm. Using Eq. 1.6, the calculated residence time of aerosol droplets passing through the heating zone of the large tubular reactor was about 23.8 s. The experiments were performed on the precursor solution S_3 using the same parameters as in the low-temperature setup (Table 2.3).

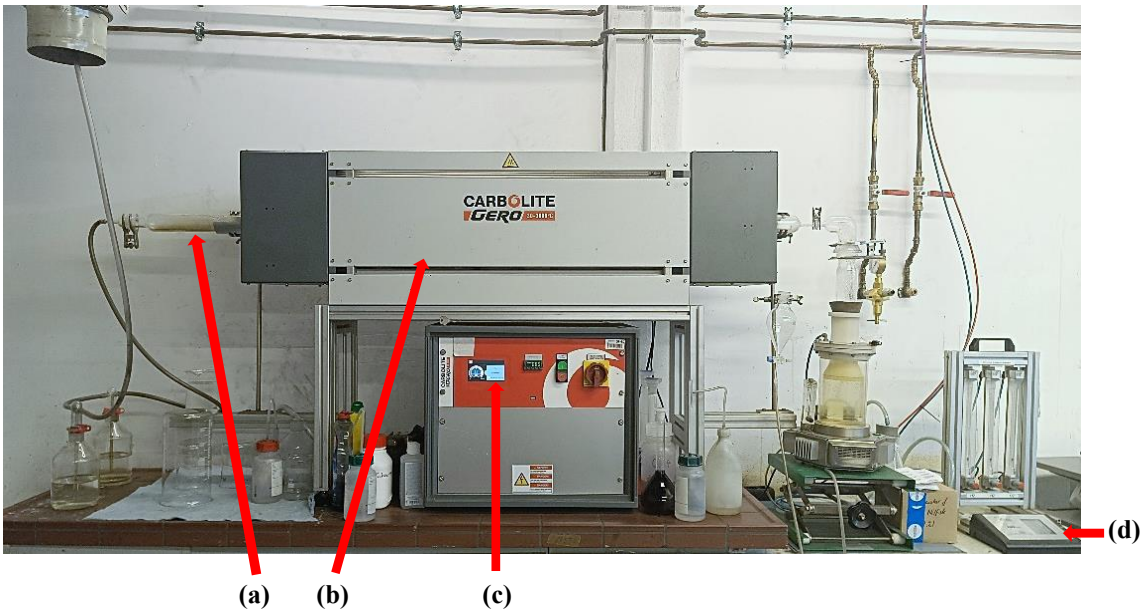

Figure 2.5. Carbolite setup for USP-HR technique with some specific features (a) alumina tube, (b) large furnace, (c) furnace control panel, (d) automatic ultrasonic generator

Table 2.3. Parameters used for the synthesis of AgCoCuFeNi NPs in the high-temperature setup

Solution	No.	Concentration (mol/L)	Temperature (°C)	H2 flow rate (L/min)	Ar flow rate (L/min)	Ultrasonic frequency (MHz)
S3	18	0.25	600	2	1	1.7
	19	0.25	700	2	1	1.7
	20	0.25	800	2	1	1.7
	21	0.25	900	2	1	1.7

2.4. Sampling and characterization of nanoparticles

At the end of each experiment, the obtained nanopowders (with deionized water) were removed from the wash bottles and placed in a large 2 L beaker to allow their sedimentation. Laboratory cleaning papers were used to cover the beaker to prevent contact of the NPs with air or oxygen. One day was enough for the complete sedimentation of the NPs. Afterward, the water was delicately removed from the beaker using a filter-based collection unit connected to a vacuum pump. The nanoparticle suspension was collected in a small open glass bottle and dried in a vacuum oven at 100 °C to obtain powder samples for X-ray diffraction (XRD) analysis. The suspension was also sampled in a small bottle for scanning electron microscope (SEM) and energy disperse X-ray spectroscopy (EDS) analyses. Figure 2.6 shows the different steps of the performed sampling.

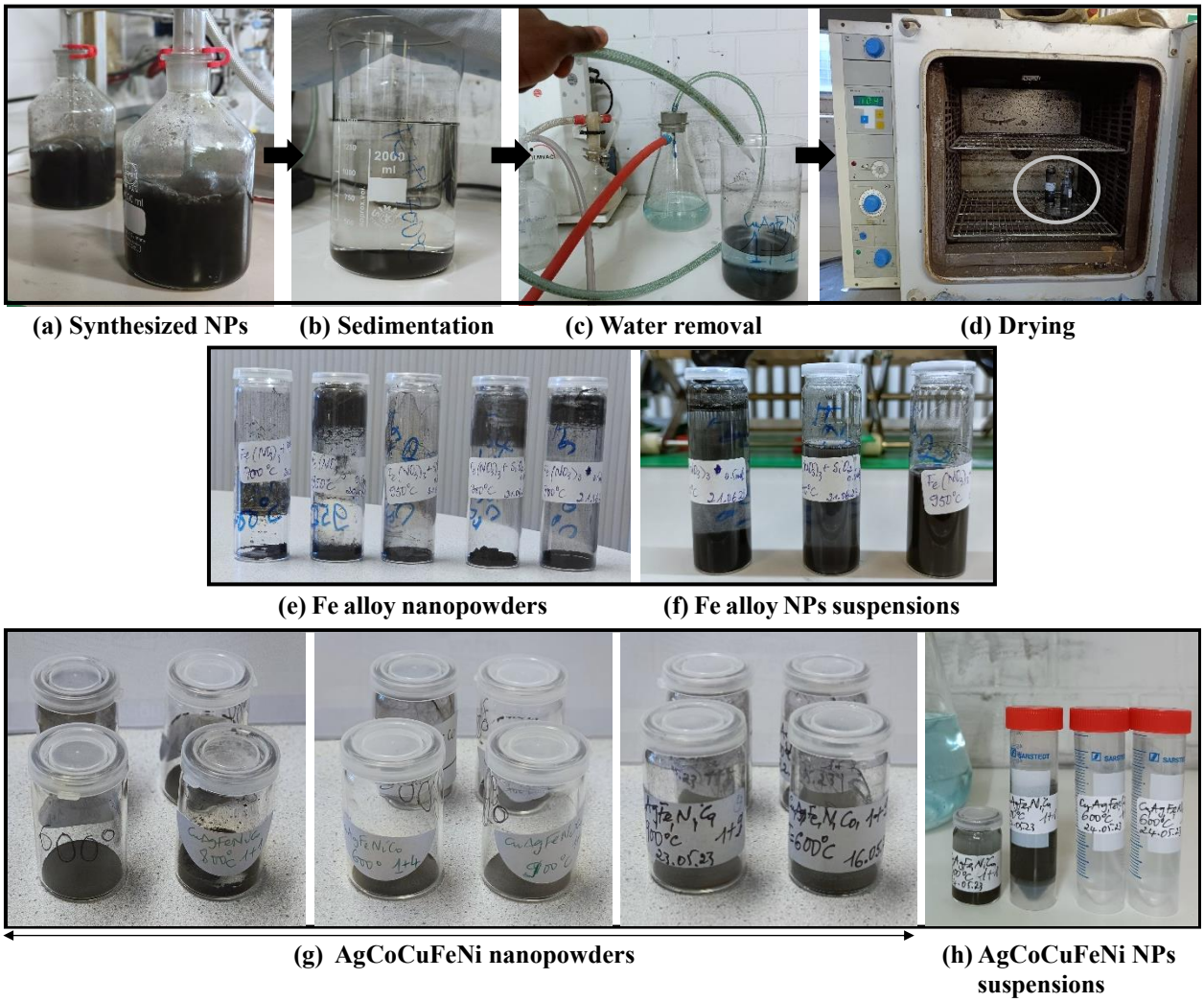

Figure 2.6. Sampling of nanoparticles

SEM images of the obtained (Fe, Fe-Si, Fe-Pt, AgCoCuFeNi) NPs were taken by Jeol JSM 7000F FEG-SEM and used to observe the surface morphology of particles formed at different reaction parameters. The particle size and size distribution were investigated from SEM images by ImagePro. EDS was carried out with a Si(Bi) X-ray detector connected to the SEM and a multi-channel analyzer, to quantify the chemical composition of the particles. The crystal structure of the particles was determined by XRD (Philips-1700 X-ray diffractometer).

Conclusion

This chapter provided a description of the methods and USP-HR equipment used for performing the experiments. Additionally, it outlined the characterization techniques used for analyzing the particle samples, which are essential for validating our hypotheses.

CHAPTER 3.

RESULTS AND DISCUSSION

CHAPTER III. RESULTS AND DISCUSSION

Introduction

This chapter is divided into two parts. First, the results of the conventional (Fe-) alloy runs were presented and analyzed. Particularly, the focus was to study the hydrogen reduction (HR) behavior of iron oxide (Fe_2O_3) in the absence and presence of additives (SiO_2 or Pt). The second part displayed the results of the AgCoCuFeNi HEA and discussed how the morphology, microstructure, composition, and crystallinity of its synthesized particles can be modified through variations in temperature, precursor solution concentration, and residence time.

3.1. Simple Fe-alloys NPs

3.1.1. Influence of temperature on HR of undoped Fe_2O_3 NPs

Without the addition of additives, we expected the following products in the synthesized nanoparticles from the hydrogen reduction of Fe_2O_3 at 700 °C: magnetite (Fe_3O_4), wuestite (FeO), and possibly metallic iron (Fe). With an increase in temperature to 950 °C, FeO and Fe were anticipated to be formed (Eqs. 1.18 – 1.20).

SEM, EDS, and XRD images were used to investigate the effects of the temperature, ranged from 700 and 950 °C, on the microstructure and composition of undoped Fe_2O_3 particles at 0.5 mol/L. SEM images of iron oxide nanoparticles are given in Figure 3.1.

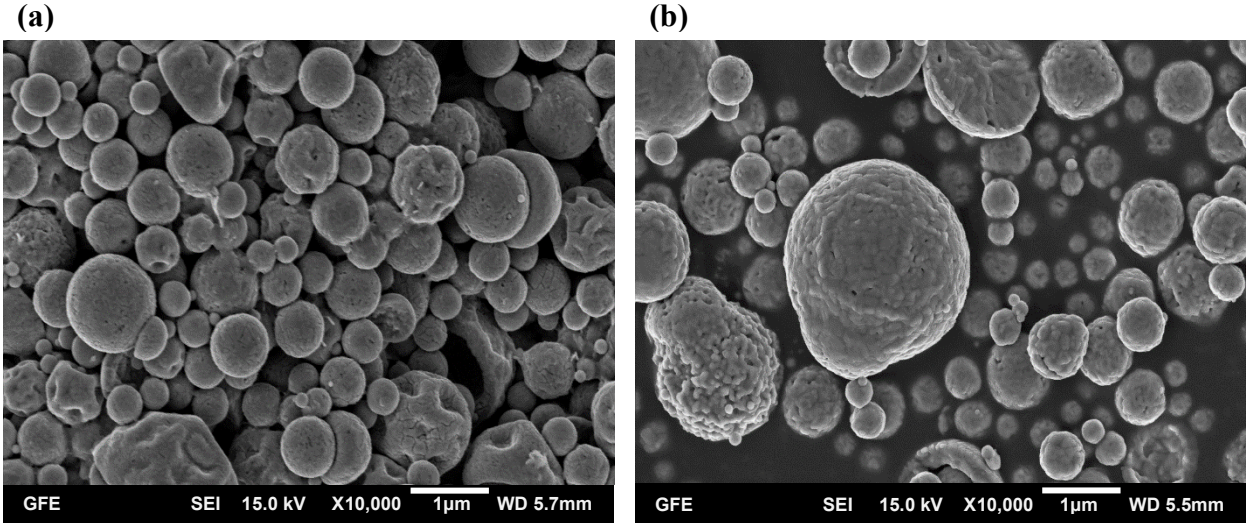

Figure 3.1. SEM analysis of undoped Fe_2O_3 particles (a) 700 °C, (b) 950 °C

Almost all particles had a spherical shape morphology with rough surfaces. Agglomeration of Fe_2O_3 NPs at 700 °C (Figure 3.1a) was reduced at 950 °C (Figure 3.1b) due to the formation of large particles from the aggregates of small particles. Consequently, the boundaries between particles became more visible at 950 °C than that at 700 °C. Moreover, it was observed that the diameters of the iron oxide particles were nearly unaffected by the variation of the reaction temperature (Figure 3.2). This is compatible with the work of Stopić *et al*. (2008) on the synthesis of copper NPs, in which they reported that increasing the furnace temperature in the range of 800 – 900 °C had little or no effect in their experimental reactor.

(a)

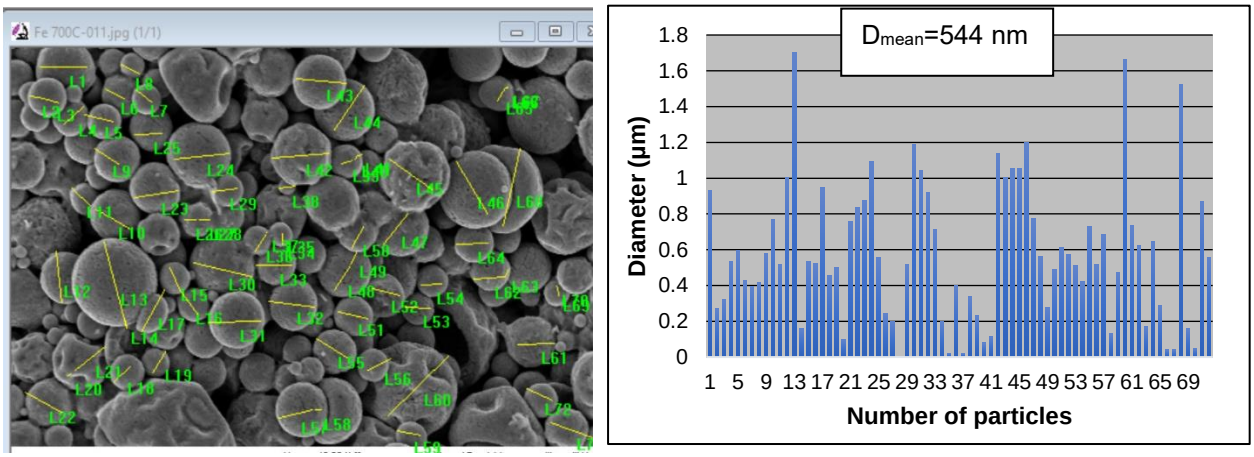

(b)

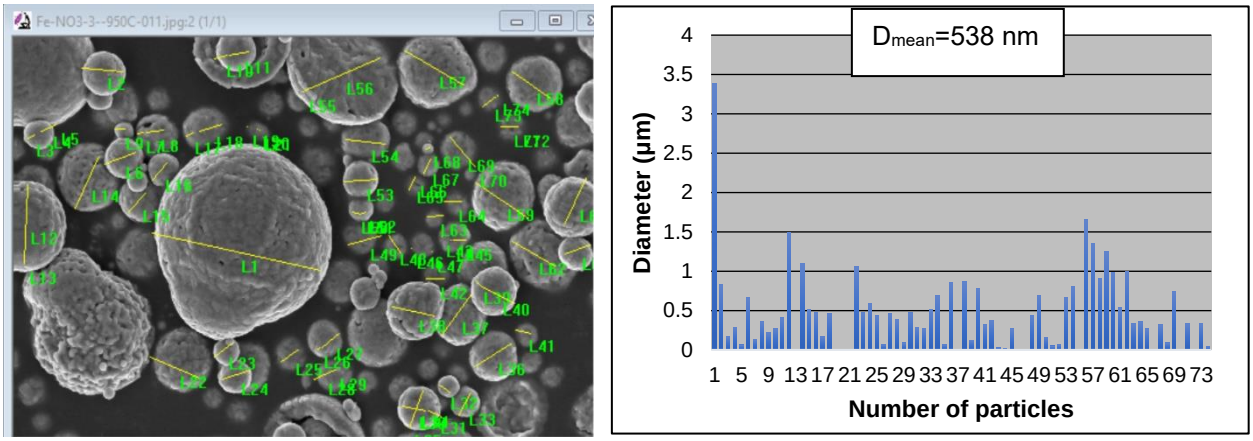

Figure 3.2. Mean diameters of Fe_2O_3 particles (a) 700 °C, (b) 950 °C

Although the maximum particle diameter jumped to 3,386 nm at 950 °C, the average particle size of iron oxide nanoparticles slightly decreased from 544 to 538 nm with an increase in temperature from 700 to 950 °C, as demonstrated in Figure 3.2.

The theoretical particle size of Fe NPs produced by the USP-HR method was determined by firstly determining the mean diameter of the aerosol droplet. Using Eq. 1.4 and the parameters of the study (γ:72.9·10^{-3} Nm^{-1}; ρ:1 g/cm3; f: 1.7 MHz), the droplet diameter was calculated as 2.92 μm. Thus, the theoretical particle diameter for 0.5 M iron nitrate precursor solution, employing Eq. 1.5, was calculated as 445 nm. The reason why the experimental particle sizes at 700 and 950 °C, 544 and 538 nm respectively, were bigger than the theoretical one may be explained by the lower rate of aggregation (Okuyama *et al*., 1986) and sintering (Jang and Jeong, 1995) of the particles due to less residence time of iron oxide droplets in the reaction zone at higher temperatures.

The quantitative results based on the EDS spectrums (Figure 3.3) of iron oxide nanoparticles are given in Table 3.1. EDS analysis indicates that particles produced from both reaction temperatures contained iron and a significant amount of oxygen. However, the atomic percentage of oxygen considerably decreased from 51.74 % to 31.15 % with an increase in temperature from 700 to 950 °C. When comparing the iron-to-oxygen (Fe/O) atomic ratios in the synthesized nanoparticles at different temperatures, we realized that the one at 950 °C (~ 100%) was greater than that at 700 °C (~ 93 %) (Table 3.1). So, the increase in reaction temperature is necessary for the elimination of some traces of oxygen from the produced nanopowder (Stopić *et al*., 2008).

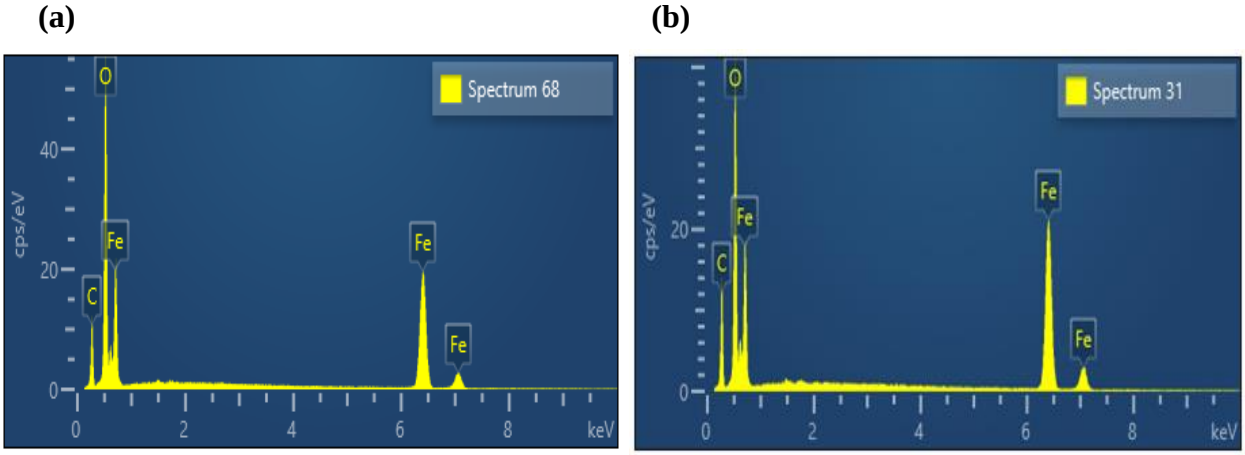

Figure 3.3. EDS spectrums for Fe_2O_3 particles produced at (a) 700 °C, (b) 950 °C

Although the atomic percentage of carbon is negligible in the synthesized particles at 700 °C, the EDS spectrum (Figure 3.3a) shows that there was a small amount of carbon detected even though its peak is weak. Carbon peaks observed at 700 and 950 °C resulted from the use of the glassy carbon slide (substrate) to fabricate the thick film for SEM/EDS characterization.

Moreover, EDS spectrums show that no impurities, such as nitrogen, were detected in the chemical composition of the particles.

Table 3.1. Atomic percentage of elements in Fe_2O_3 particles obtained by EDS analysis

		T (700 °C)		*T (950 °C)*	
Element	Atom. Mass (g/mol)	Weight (%)	Atom. (%)	Weight (%)	Atom. (%)
Iron	55.845	76.5	48.26	65.4	31.89
Oxygen	16	23.5	51.74	18.3	31.15
Carbon	12.01	0	0	16.3	36.96
Sum		**100**	**100**	**100**	**100**

All the obtained XRD patterns for the Fe-alloy (including AgCoCuFeNi HEA) runs exhibited multiple peaks or diffraction angles (Figure 3.4, 3.8, 3.11 and 3.16), making it difficult to distinguish and identify individual phases or crystal structures. We believe that employing high-resolution and 2D-XRD techniques is necessary to achieve accurate phase identification.

Figure 3.4. XRD patterns of Fe_2O_3 particles produced at (a) 700 °C, (b) 950 °C

However, the patterns shown in Figure 3.4 suggest that the hydrogen reduction of Fe_2O_3 in the absence of additives was complete at both reaction temperatures, leaving no traces of hematite behind. They reveal that the products formed at 700 °C were Fe_3O_4, and FeO (Figure 3.4a), while those at 950 °C were Fe_3O_4, FeO, and Fe (Figure 3.4b). Magnetite exhibited higher peaks in the synthesized particles at both reaction temperatures compared to the other products. Wuestite, resulting from the reduction of magnetite, was also present at both temperatures and was further reduced to iron with an increase in temperature from 700 to 950 °C. However, the iron peak was lower compared to that of the other products at 950 °C. Thus, XRD and EDS results are compatible with each other.

3.1.2. Influence of silicon on HR of Fe_2O_3 NPs

By adding 10 ml of colloidal silica (40 wt.% SiO_2) to 400 ml of 0.5 M iron nitrate solution, we expected the hydrogen reduction of Fe_2O_3 to be inhibited, resulting in the formation of only Fe_3O_4, with some remaining traces of Fe_2O_3 (Eqs. 1.18).

The effect of the Si content of the precursor mixture on the microstructure and size of iron oxide nanoparticles was investigated through SEM. Comparative analysis of SEM images of undoped Fe_2O_3 NPs (Figure 3.1) versus those of Si-doped Fe_2O_3 NPs (Figure 3.5), suggests that the darker particle-like objects were iron particles and were caged by brighter siliceous materials. In the Si-doped Fe_2O_3 runs, spherical particles with smooth surfaces were produced.

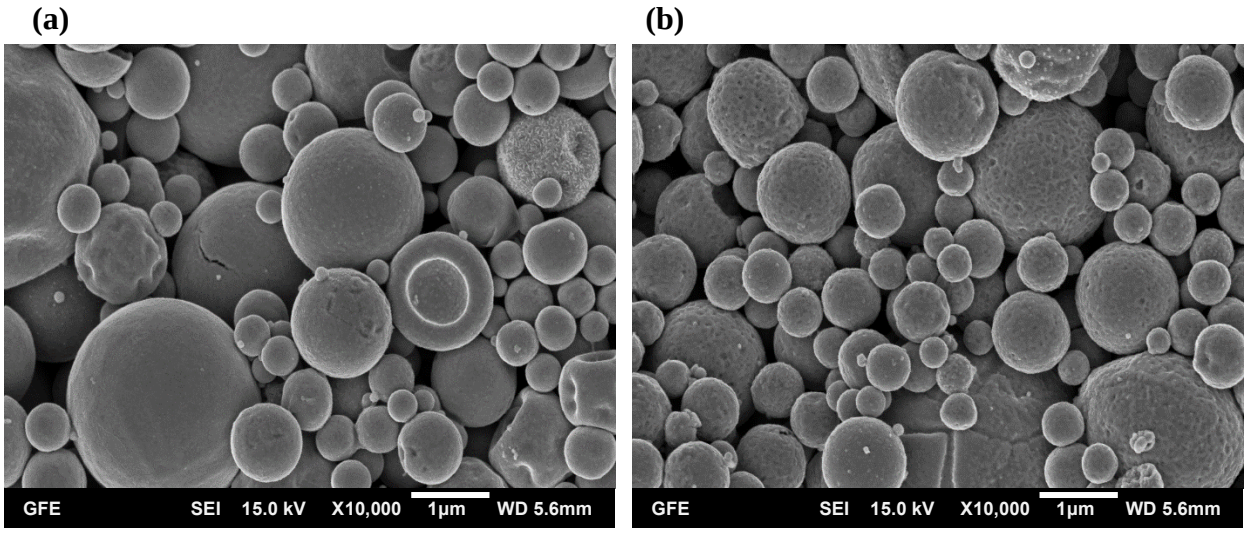

Figure 3.5. SEM analysis of Fe-Si particles (a) 700 °C, (b) 950 °C

At both temperatures, the agglomeration and formation of large particles were more pronounced than that of the Fe_2O_3-only experiments (Figure 3.5).

The size distribution of Si-doped Fe_2O_3 NPs is shown in Figure 3.6. With the addition of a small quantity of SiO_2 to the iron nitrate solution, the average particle size significantly increased from 544 to 877 nm and from 538 to 1032 nm at 700 and 950 °C, respectively (Figures 3.2 and 3.6). The slight decrease in particle size observed in Fe_2O_3-only runs when the temperature increased to 950 °C was also inhibited by Si-doping.

(a)

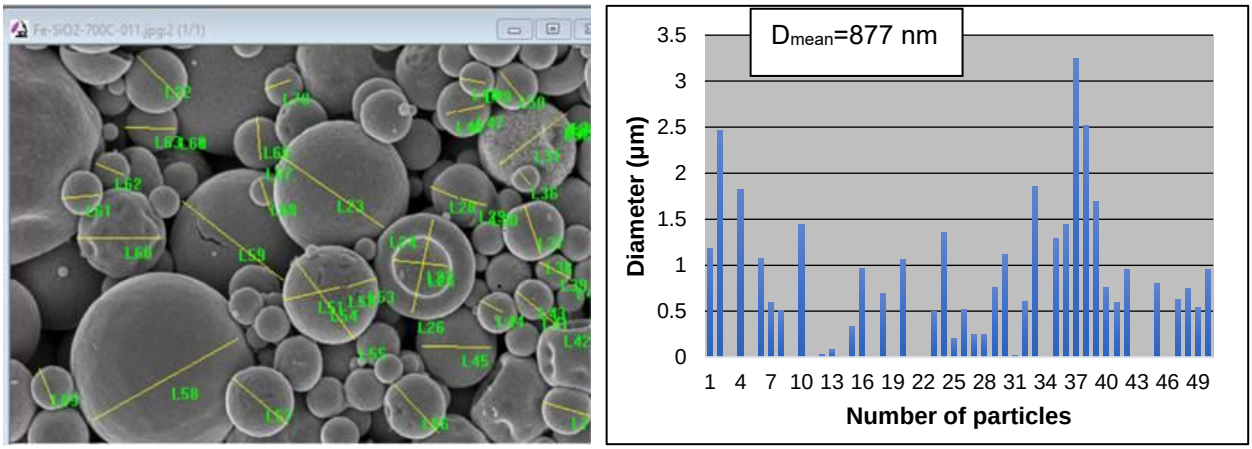

(b)

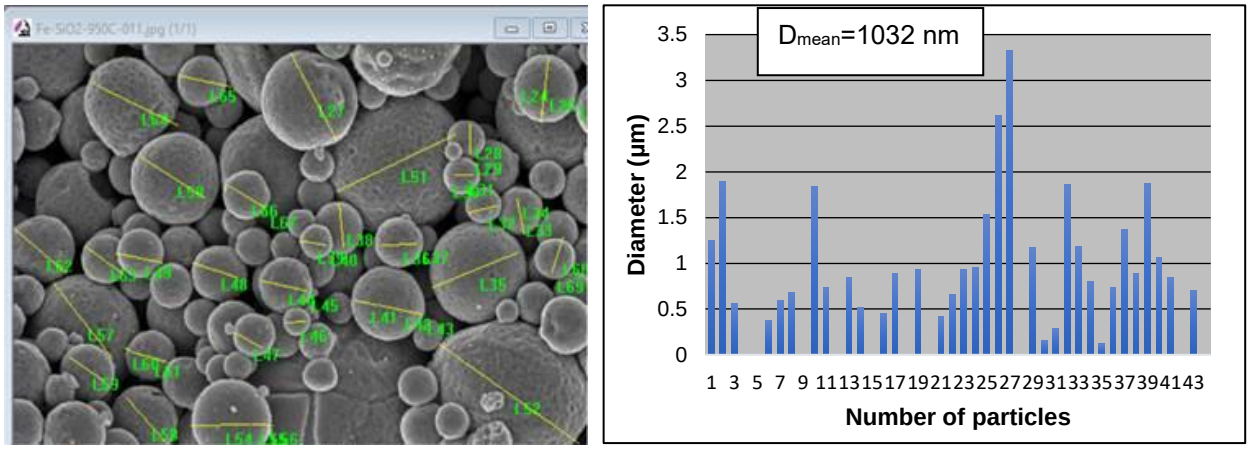

Figure 3.6. Mean diameters of Fe-Si particles (a) 700 °C, (b) 950 °C

EDS analysis was used to clarify the chemical composition of the synthesized Fe-Si nanoparticles (Figure 3.7). The quantitative results from the two Fe-Si EDS spectrums, presented in Table 3.2, indicate that when Si was included in the experiments, the atomic percentage of oxygen became slightly higher in the Si-doped Fe_2O_3 NPs compared to the undoped Fe_2O_3 NPs.

However, the atomic percentage of iron drastically decreased to 19.91 or 18.40 at.% at 700 and 950 °C, respectively (Tables 3.1 and 3.2). This suggests that the reduction reaction of Fe_2O_3 in an Ar-H_2 atmosphere becomes less efficient when alloyed with Si in comparison to unalloyed Fe_2O_3. Furthermore, as the temperature increased to 950 °C, we noticed that the oxygen content in the Fe-Si nanoparticles increased slightly from 43.91 to 45.97 at.%, whereas the opposite was observed in the Fe_2O_3-only runs. Consequently, the atomic percentage of iron slightly decreased from 19.91 to 18.40 at.%, signifying that the temperature increase further inhibits the hydrogen reduction of iron oxide nanoparticles during Si-doping.

(a) **(b)**

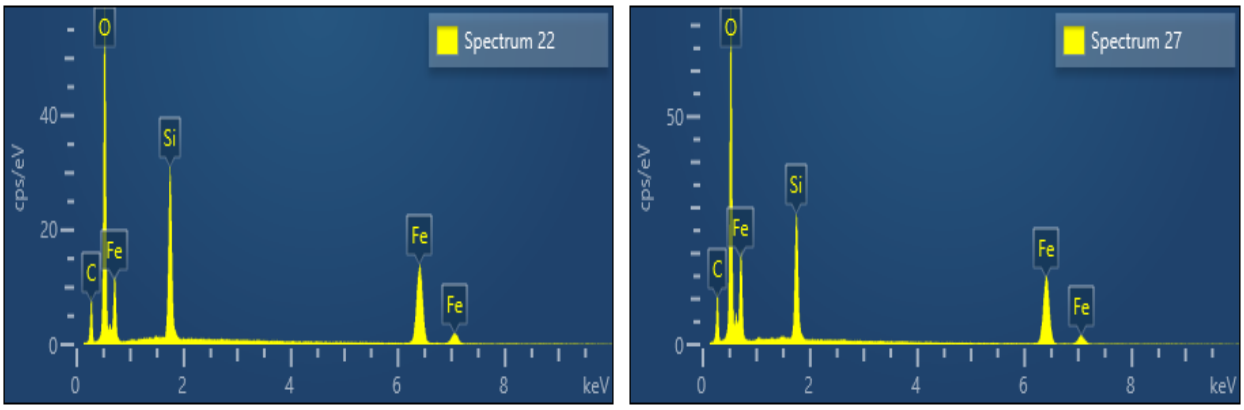

Figure 3.7. EDS spectrums for Si-doped Fe_2O_3 particles produced at (a) 700 °C, (b) 950 °C

Table 3.2. Atomic percentage of elements in Si-doped Fe_2O_3 particles obtained by EDS analysis

		T (700 °C)		*T (950 °C)*	
Element	Atom. Mass (g/mol)	Weight (%)	Atom. (%)	Weight (%)	Atom. (%)
Iron	55.845	46.1	19.91	44.3	18.40
Oxygen	16	29.1	43.91	31.7	45.97
Silicon	28.086	11.7	10.06	9.7	8.00
Carbon	12.01	13.1	26.12	14.3	27.63
Sum		**100**	**100**	**100**	**100**

XRD patterns of the Si-doped Fe_2O_3 runs reveal that the products formed at both reaction temperatures are Fe_3O_4 and FeO, with remaining traces of Fe_2O_3 (Figure 3.8). No metallic iron (Fe) was formed at any temperature. This suggests that the hydrogen reduction of Fe_2O_3 was not complete. Silicon acts on Fe_2O_3 by creating a layer enriched with SiOx in the surface-near region to block free surfaces of iron oxide, hindering their direct interactions with the hydrogen-reducing agent (Park *et al*., 2004; Patterer *et al*., 2023). We also noticed that the peak of hematite (Fe_2O_3) in the synthesized particles at 950 °C was higher than that at 700 °C, which proves that Si-doping further inhibits the hydrogen reduction of Fe_2O_3 at higher temperatures.

Figure 3.8. XRD patterns of Si-doped Fe_2O_3 particles at (a) 700 °C, (b) 950 °C

3.1.3 Platinum effect on HR of Fe_2O_3 NPs

Upon introducing 5ml of platinum (IV) nitrate solution (15 wt.% Pt) into 400 ml of 0.5 M iron nitrate solution, we expected that the hydrogen reduction of Fe_2O_3 would be accelerated, resulting in the formation of FeO and Fe, with no residual traces of Fe_2O_3.

SEM, EDS, and XRD analyses were also used to investigate the influence of platinum on the particle size and composition of iron oxide nanoparticles at 700 °C. In the Fe_2O_3-only experiments at 700 °C, long aggregates, consisting of primary particles with an average size of about 544 nm, were formed, and the boundaries between these particles were not clear (Figures 3.1a and 3.2a). With the addition of a very small quantity of Pt to the iron nitrate solution, the agglomeration of particles decreased significantly; the average particle size slightly increased to 591 nm and the boundaries became clearer (Figures 3.9a and 3.10).

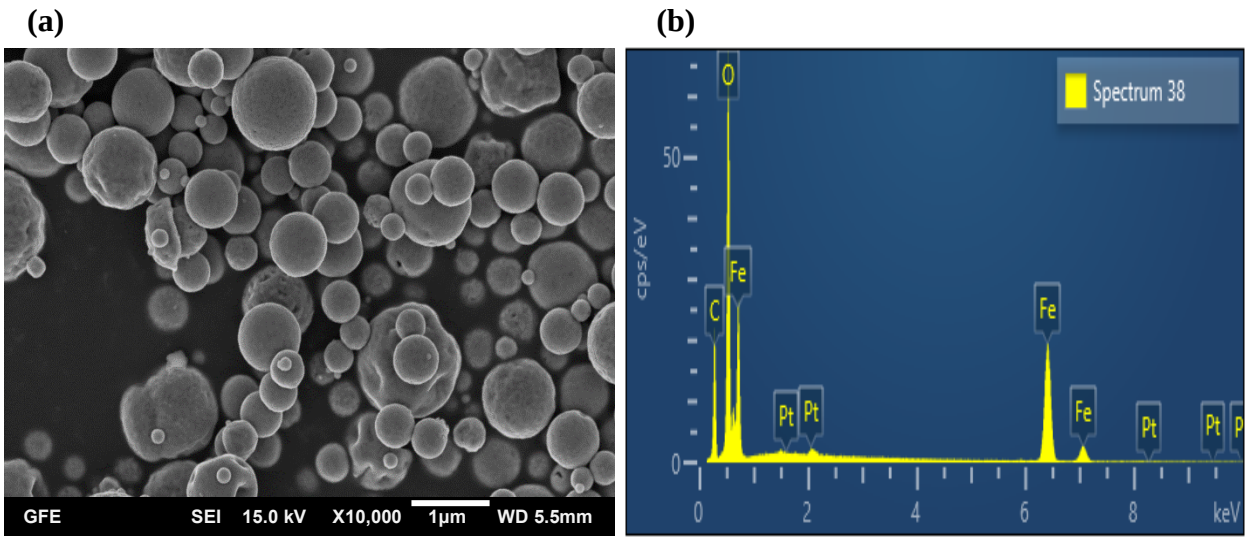

Figure 3.9. Analysis of Fe-Pt NPs with (a) SEM, (b) EDS images at 700 °C

The quantitative results based on the EDS spectrums (Figure 3.9b) of Pt-doped Fe_2O_3 NPs at 700 °C are given in Table 3.3. EDS analysis indicates that when Fe_2O_3 was doped with Pt, the atomic percentage of oxygen experienced a significant decrease from 51.74 to 36.51 at.% after the hydrogen reduction treatment. However, the Fe/O atomic ratio in the synthesized Fe-Pt particles was slightly lower than that in the undoped Fe_2O_3 particles at 700 °C (Tables 3.1 and 3.3). Despite this observation being noted, the XRD pattern suggests that, in addition to the Fe_3O_4 and FeO products, metallic iron (Fe) was formed during Pt-doping at 700 °C (Figure 3.11). In the Fe_2O_3-only runs, Fe was only formed at the higher temperature of 950 °C.

This implies that, even at low temperatures and with a relatively low concentration of Pt (0.09 at.%), Fe could be directly obtained from the hydrogen reduction of Fe_2O_3.

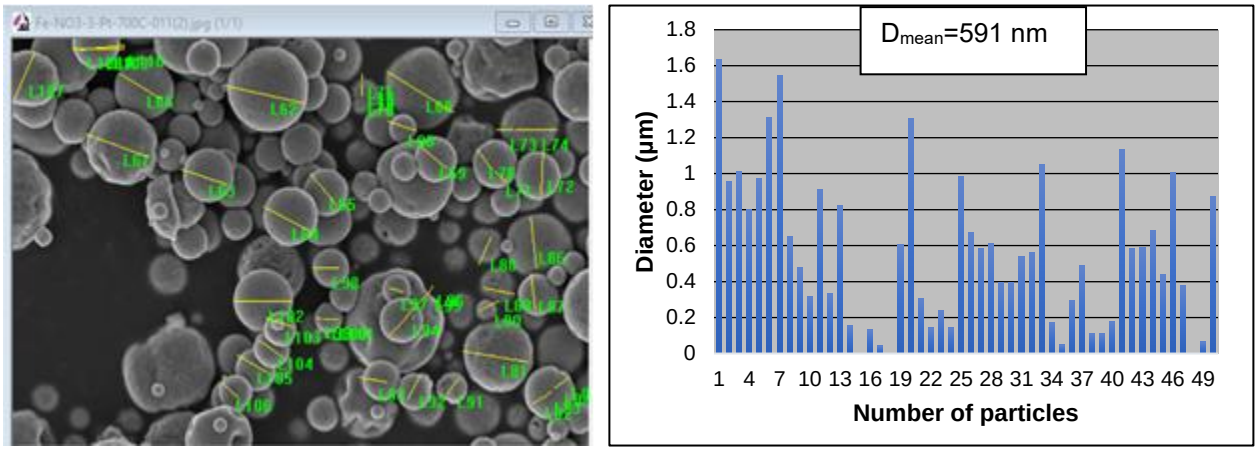

Figure 3.10. Mean diameter of Fe-Pt particles at 700 °C

Table 3.3. Atomic percentage of elements in Pt-doped Fe_2O_3 particle obtained by EDS analysis

Element	Atom. Mass (g/mol)	Weight (%)	Atom. (%)
Iron	55.845	59.6	27
Oxygen	16	23.1	36.51
Platinum	195.084	0.7	0.09
Carbon	12.01	17.3	36.42
Sum		**100**	**100**

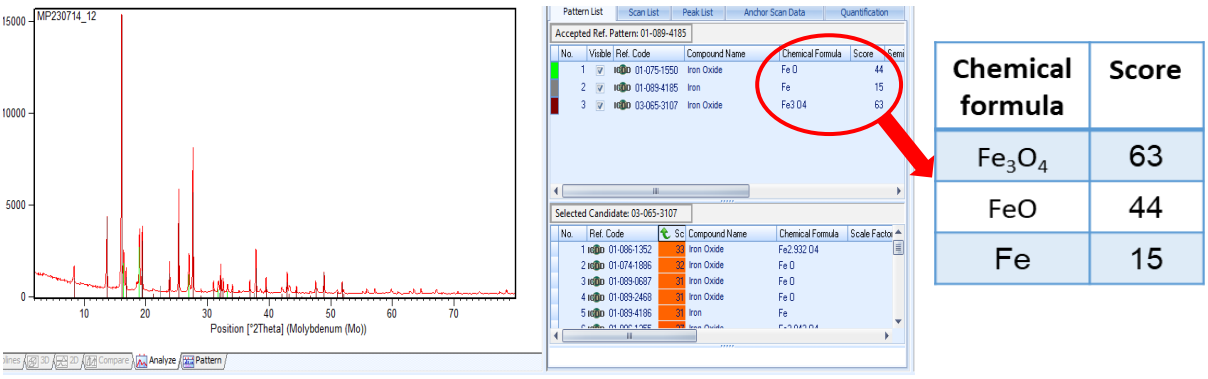

Figure 3.11. XRD patterns of Fe-Pt particles produced at 700 °C

Unlike silicon, which blocks the free surfaces of iron oxide, platinum offers active sites on its surface to facilitate the adsorption of hydrogen molecules, their subsequent dissociation into atomic hydrogen species, and a more facile reaction with the iron oxide (Karim *et al.*, 2017; Meng *et al.*, 2019. We believe that by increasing the platinum concentration in the precursor solution, the Fe/O atomic ratio in the synthesized Fe-Pt NPs would be greater than that in the undoped Fe_2O_3 NPs at 700 °C. By considering this aspect and performing calculations for the relative concentration or atomic percentage of iron and oxygen, based on Tables 3.1 and 3.2, a scenario like the one illustrated in Figure 3.12a can be anticipated.

Conclusion

The above results validated the hypothesis that the hydrogen-based direct reduction of iron trioxide can be inhibited and accelerated by silicon (Si) and platinum (Pt), respectively. Figure 3.12b shows a summary of the hydrogen reduction behavior of Fe_2O_3 in the presence and absence of additives (SiO_2 or Pt) by ultrasonic spray pyrolysis method.

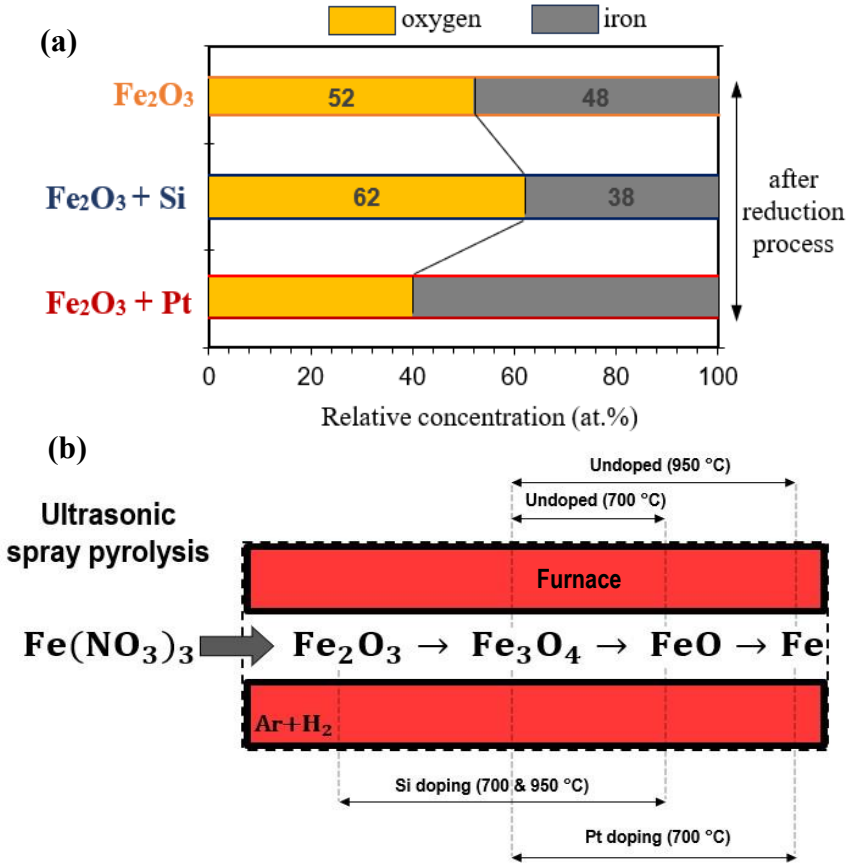

Figure 3.12. a) The surface Fe/O ratio of undoped, Si-doped, and Pt-doped Fe_2O_3 NPs after hydrogen reduction at 700 °C, b) Hydrogen reduction of Fe_2O_3 by USP

3.2. Effects of processing parameters on the AgCoCuFeNi HEA NPs

3.2.1. Influence of temperature

The effects of the reaction temperature on the particle size, morphology, and composition of AgCoCuFeNi nanoparticles were investigated while keeping the other parameters at constant values. SEM images of particles synthesized in the low-temperature setup at 600, 700, 800 and 900 °C using 0.05M precursor solution are shown in Figure 3.13.

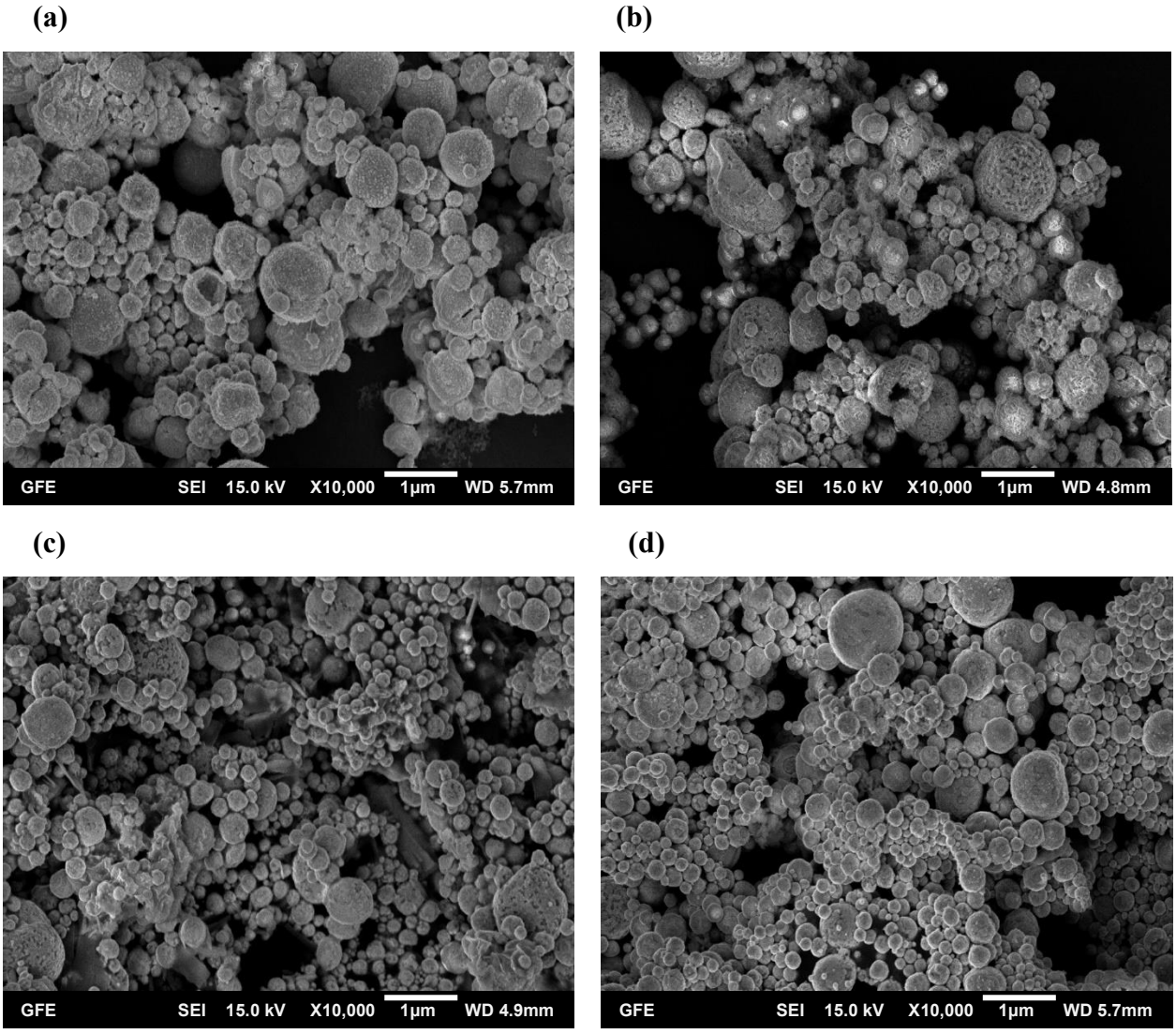

Figure 3.13. SEM analysis of AgCoCuFeNi particles produced at 0.05 mol/L (a) 600 °C, (b) 700 °C, (c) 800 °C, (d) 900 °C

SEM results show that almost all particles had spherical morphology and appeared to be smoother on the surface with increasing temperature. Moreover, it was observed that the densification of small particles increased while the average particle size tended to decrease with increasing reaction temperature (Figures 3.13 and 3.14). The average particle sizes, calculated using ImagePro software, were 428, 382, 280, and 264 nm at 600, 700, 800, and 900 °C, respectively (Figure 3.14).

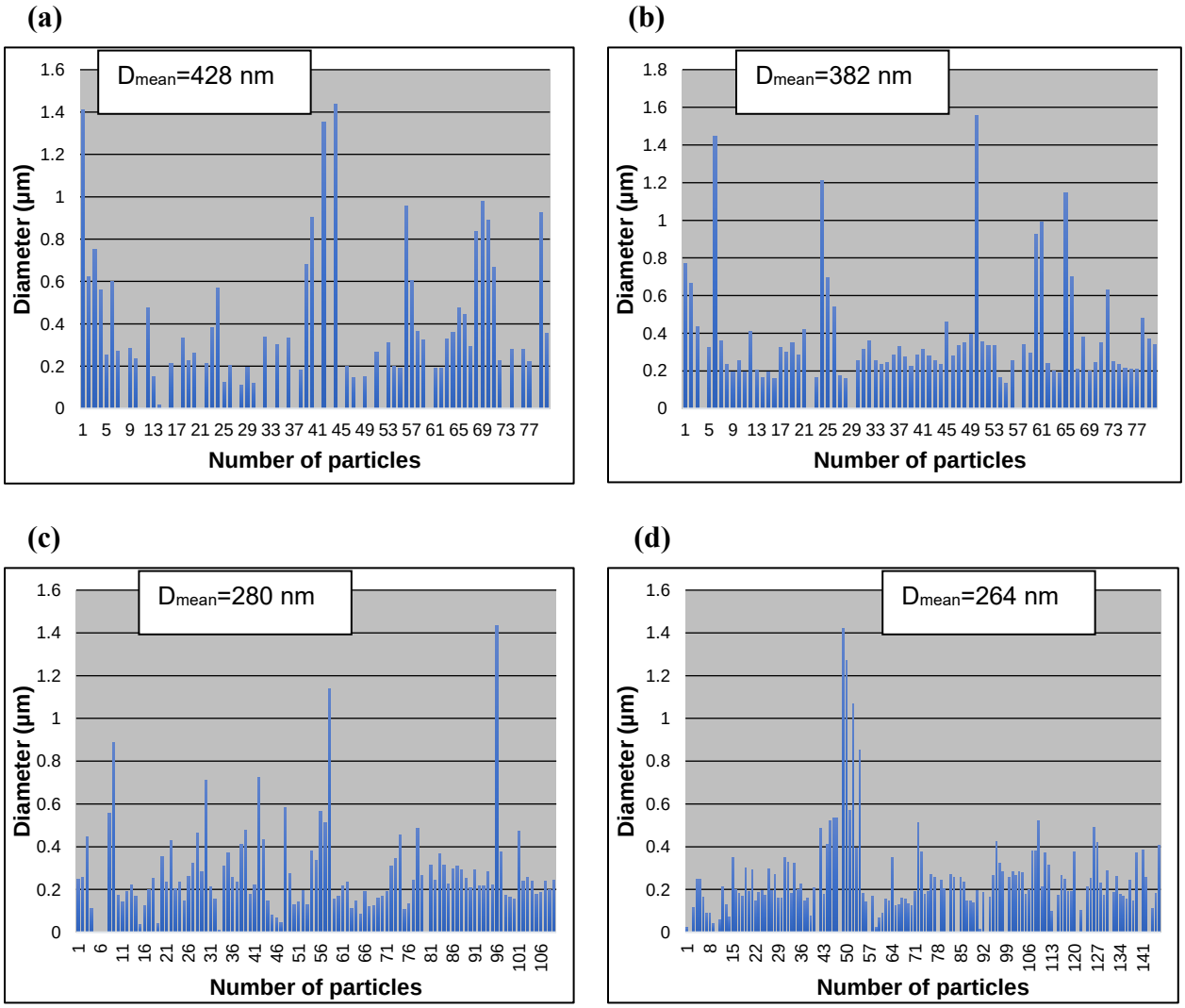

Figure 3.14. Mean diameters of AgCoCuFeNi particles at 0.05 mol/L (a) 600 °C, (b) 700 °C, (c) 800 °C, (d) 900 °C

The results of EDS analysis (Figure 3.15) of the AgCoCuFeNi HEA particles synthesized at different reaction temperatures, 600, 700, 800, and 900 °C, are given in Table 3.4. The results indicate that the elements making up the composition were present in close amounts at all reaction temperatures, suggesting that the AgCoCuFeNi HEA NPs were successfully formed using the USP-HR approach. When the temperature reached 900 °C, four of the metal elements (Ag, Co, Fe, and Ni) in the synthesized nanoparticles appeared to be in very similar proportions and their atomic percentages increased to 15.25% for Ag, 15.68% for Co, 15.05% for Fe, and 15.44% for Ni, while the percentage of Cu remained relatively large at all temperatures and increased to 21.2% at 900°C. The oxygen content in the particles decreased with increasing temperature, as proven in Chapter 3.1.1.

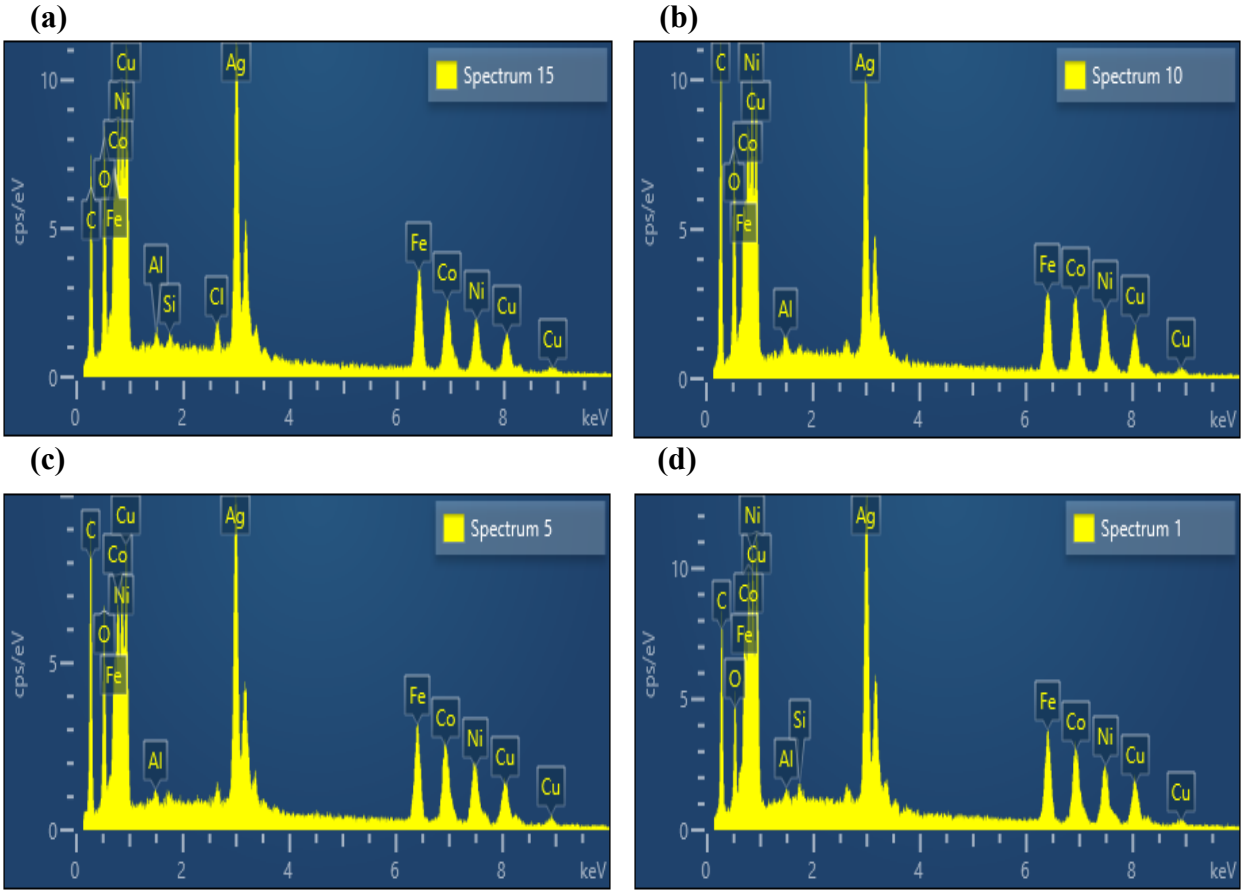

Figure 3.15. EDS spectrums for AgCoCuFeNi particles at 0.05 mol/L (a) 600 °C, (b) 700 °C, (c) 800 °C, (d) 900 °C

Table 3.4. EDS results of AgCoCuFeNi NPs produced at different temperatures at 0.05 mol/L

Temperature (°C)	Element (at.%)							
	Ag	Co	Cu	Fe	Ni	O	Al	Cl
600	13.06	11.77	19.55	14.35	12.09	28.33	–	0.91
700	11.77	14.04	18.09	11.79	15.17	28.24	0.78	0
800	12.96	14.79	17.57	13.85	14.66	25.53	0.60	0
900	15.25	15.68	21.2	15.05	15.44	16.69	0.66	0

Small peaks of aluminum (Al), chlorine (Cl), and silicon (Si) were also detected in the EDS spectrums. Al was used as the background material for EDS analysis. We believe that Si came from the use of the silica glass tube. During the USP-HR method for producing nanoparticles, it is possible that under heating of the silica tube by the furnaces, small traces of silicon decomposed and infiltrated the particles. It is also possible that the water used during precursor and sample preparation was not properly distilled and purified. As a result, it may have contained impurities such as silicon and chlorine.

Additionally, we can take note of the bright dots randomly distributed in the synthesized AgCoCuFeNi particles at all reaction temperatures (Figure 3.13). In fact, four of the metal elements, Co, Cu, Fe, and Ni, have similar atomic masses, 58.9, 63.5, 55.8, 58.7 g/mol, respectively, while one element, Ag, has a relatively larger atomic mass (107.8 g/mol). It is known that atoms with a higher atomic mass tend to create a stronger interaction with the electron beam in SEM analysis. Consequently, they produce stronger backscattered and secondary electron signals which appear brighter in the SEM image. The bright dots in the AgCoCuFeNi nanoparticles, as shown in Figure 3.13, are likely caused by the presence of Ag atoms. This phenomenon was previously proven in the research by Yang *et al*. (2020), where they reported that the bright dots observed in the NiCoCuFePt particles were attributed to the presence of Pt atoms because of their relatively high atomic mass.

As stated earlier, high-resolution and 2D-XRD techniques are needed to precisely identify the various crystal phase structures in the synthesized AgCoCuFeNi particles. However, the XRD patterns shown in Figure 3.16 suggest that all five metal elements were present in the synthesized AgCoCuFeNi particles at 700 and 900 °C (Figure 3.16).

With an applied magnetic field (e.g., magnet), all the AgCoCuFeNi samples also showed a magnetic behavior (Figure 3.17), mainly due to the presence of ferromagnetic materials (Fe, Ni, and Co) in the composition. Yet, specific characterization tools like magnetic particle analyzer (MPA) are required to quantify or study the degree to which a sample exhibits magnetic properties compared to the others.

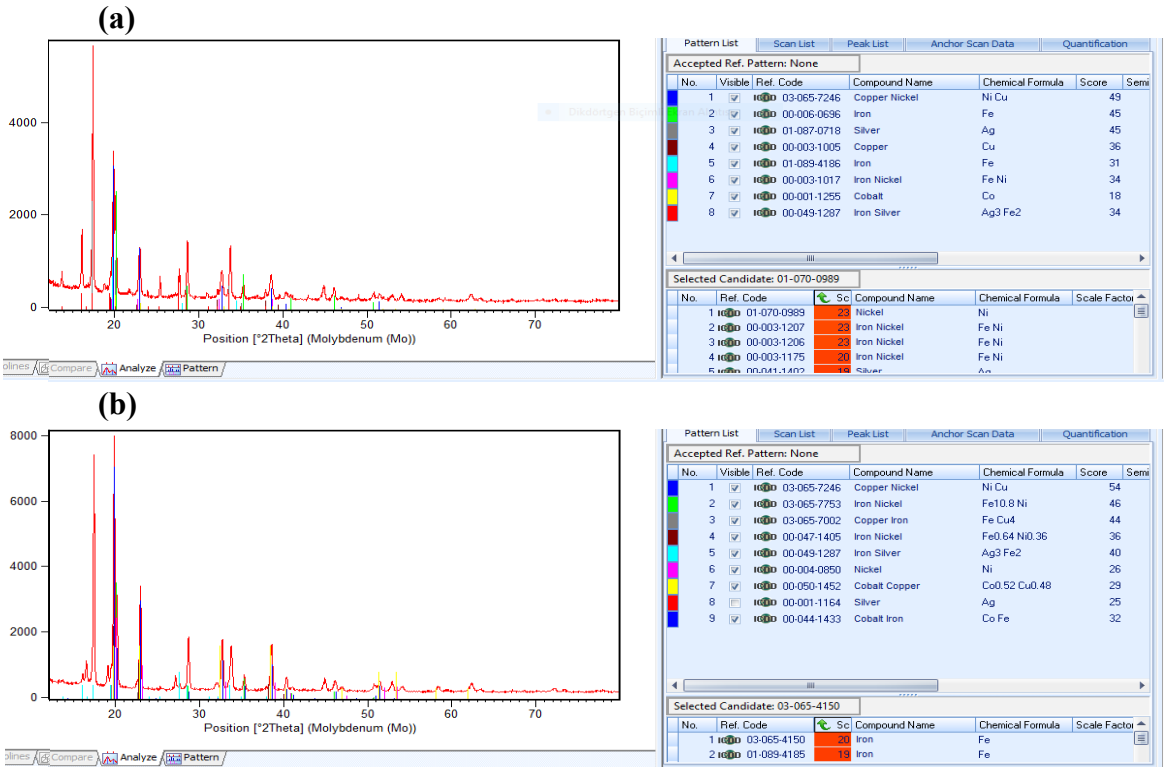

Figure 3.16. XRD patterns of AgCoCuFeNi particles produced at (a) 700 °C, (b) 900 °C

Figure 3.17. AgCoCuFeNi samples with magnetic properties

3.2.2. Influence of concentration

Here, the effects of the precursor solution concentration, ranging from 0.25, 0.1, and 0.05 M, on the particle size, morphology, and composition were investigated at 900 °C.

SEM images of the AgCoCuFeNi particles are given in Figure 3.18. Particles prepared in all concentrations had spherical morphology but became smoother on the surface with decreasing solution concentration. The AgCoCuFeNi particles exhibited a decreasing trend as the corresponding solution concentration decreased from 0.25 or 0.1 to 0.05 M but showed an increasing trend when the concentration was reduced from 0.25 to 0.1 M (Figure 3.19).

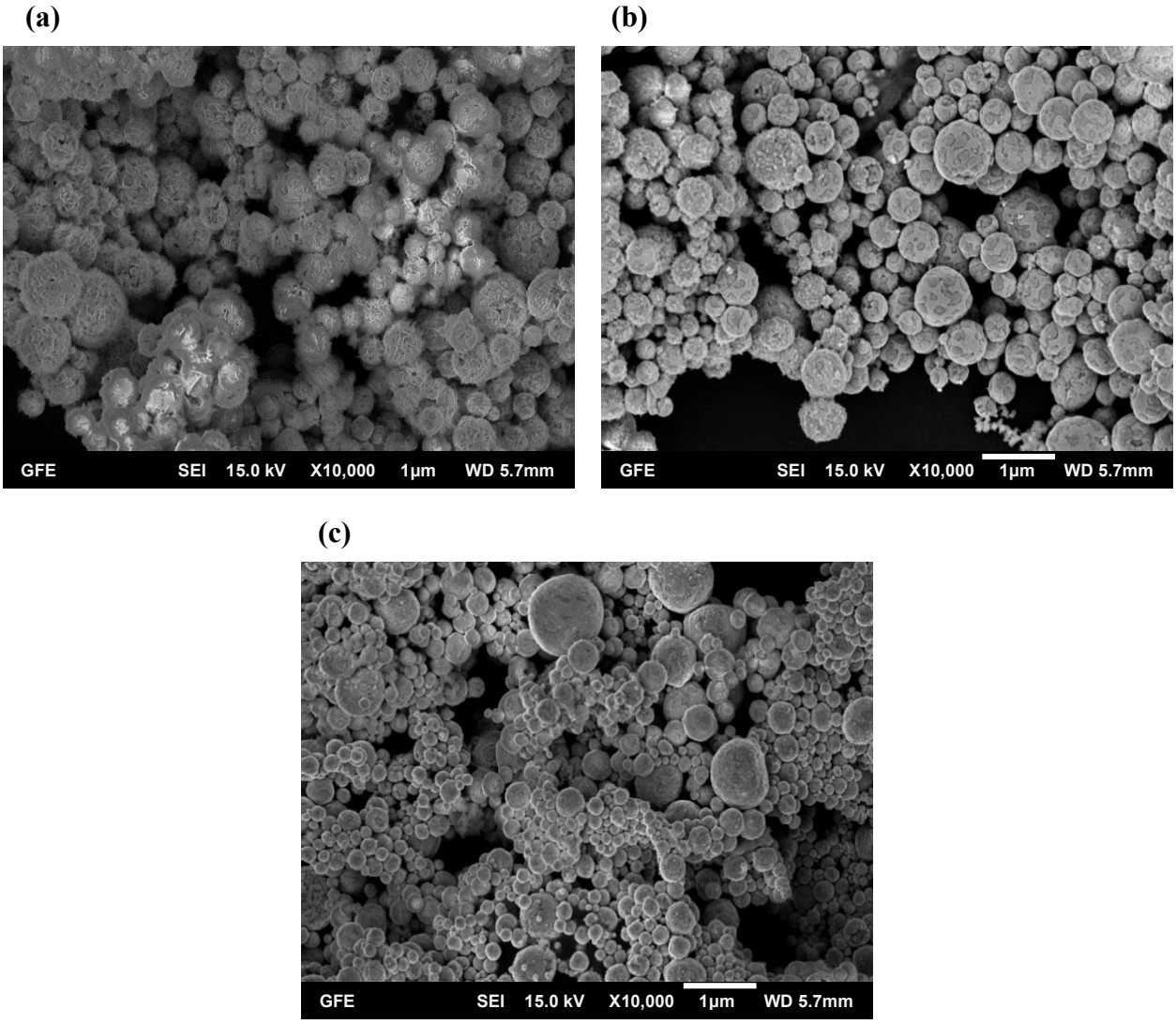

Figure 3.18. SEM analysis of AgCoCuFeNi particles at 900 °C (a) 0.25 mol/L, (b) 0.1 mol/L, (c) 0.05 mol/L

The average particle sizes for the synthesized AgCoCuFeNi particles using 0.25, 0.1, and 0.05 M solutions were 294, 641, and 264 nm, respectively (Figure 3.19). Moreover, it was observed that narrower size distribution was obtained at 0.05 M and the size uniformity of the particles increased by reducing the solution concentration to 0.05 M (Figure 3.19).

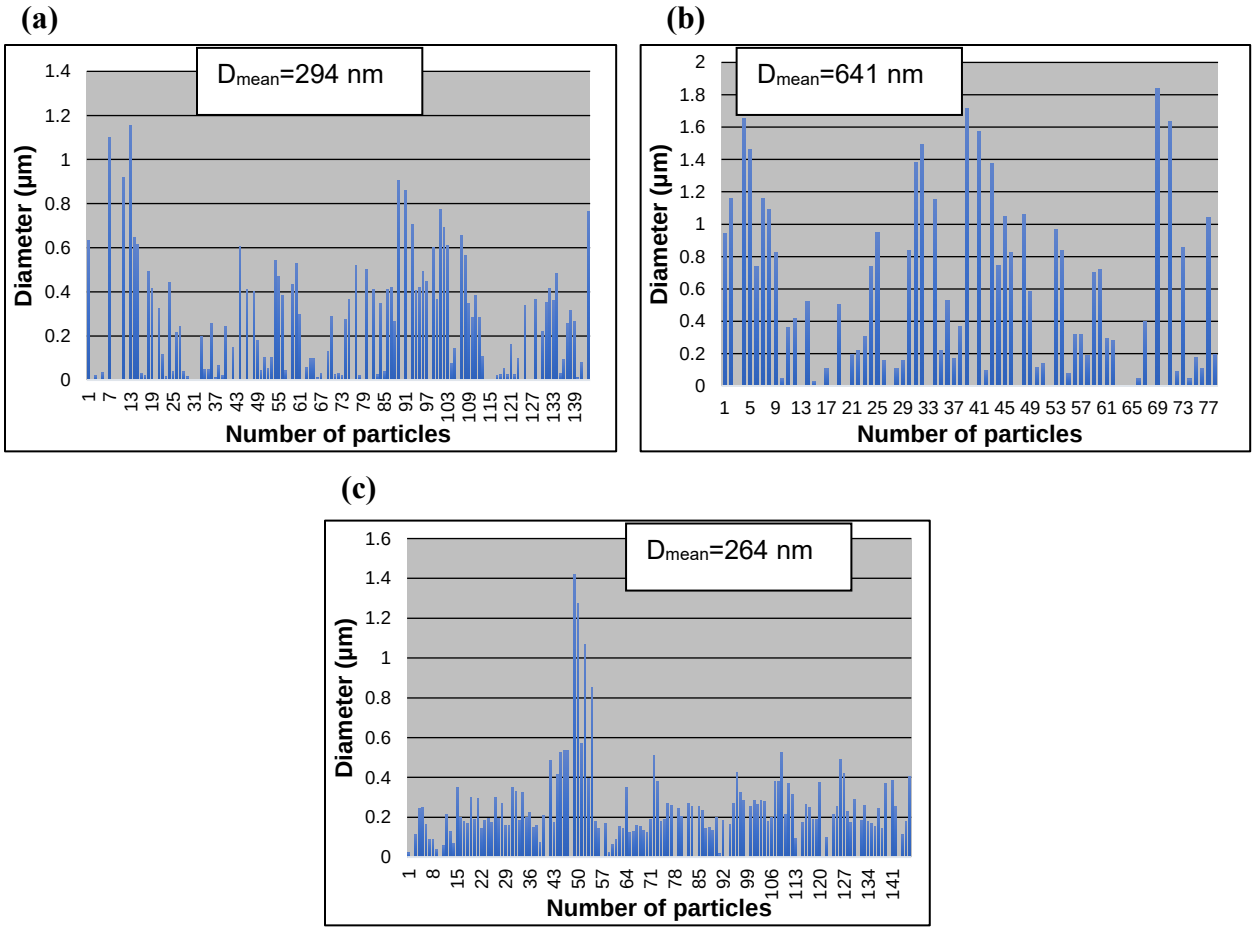

Figure 3.19. Mean diameters of AgCoCuFeNi particles at 900 °C (a) 0.25 mol/L, (b) 0.1 mol/L, (c) 0.05 mol/L

EDS analysis indicates that AgCoCuFeNi particles produced from both precursor concentrations, 0.25 and 0.05 M, contained the five metal elements (Ag, Co, Cu, Fe, and Ni) in closer proportions than AgCoCuFeNi particles synthesized at 0.1 M. In particular, the atomic percentage of Cu element remained relatively high at 0.25 and 0.05 M but was low at 0.1 M compared to the other metal elements present in the nanoparticles. In addition, the oxygen content decreased with decreasing precursor concentration (Figure 3.20 and Table 3.5).

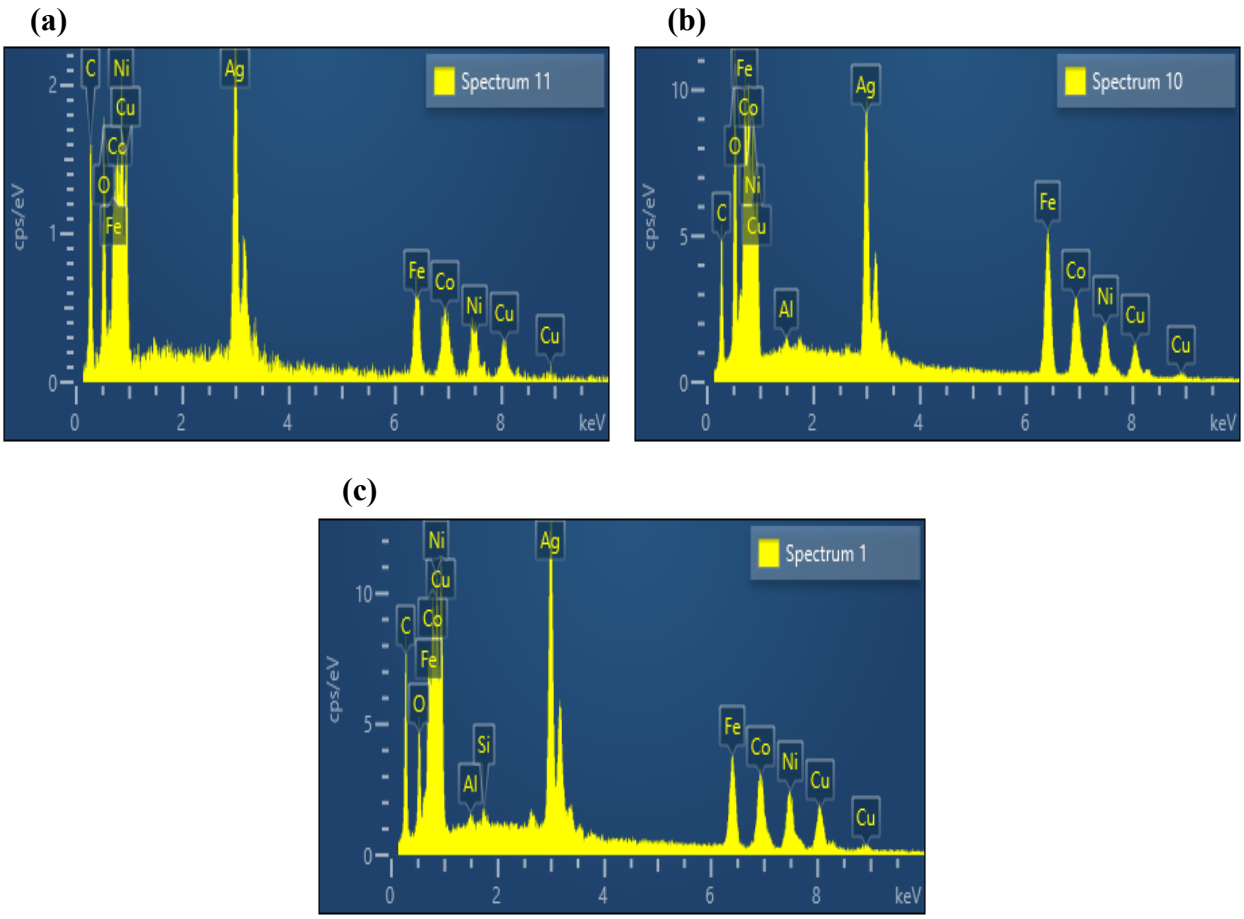

Figure 3.20. EDS spectrums for AgCoCuFeNi particles at 900 °C (a) 0.25 mol/L, (b) 0.1 mol/L, (c) 0.05 mol/L

Table 3.5. EDS results of AgCoCuFeNi NPs produced at different concentrations at 900 °C

Concentration (mol/L)	Element (at.%)						
	Ag	Co	Cu	Fe	Ni	O	Al
0.25	13.44	11.77	15.65	13.56	13.59	31.96	0
0.1	10.24	13.65	9.89	19.60	12.28	33.77	0.54
0.05	15.25	15.68	21.2	15.05	15.44	16.69	0.66

3.2.3. Influence of residence time

The effects of the residence time on the particle size, morphology, and composition of AgCoCuFeNi nanoparticles were also investigated using the 0.05M precursor solution at 900 °C in the small and large tubular reactor.

Spherical particles with smooth surfaces were obtained only from the low-temperature setup with a short residence time of 5.3 s. When the residence time was increased to 23.8 s using the high-temperature setup, particles with an unclear structure but approximately spherical shape with rough surfaces were formed (Figure 3.21). Indeed, the amount of AgCoCuFeNi particles obtained at the end of the USP-HR process in the wash bottles of the high-temperature setup was quite low compared to that of the low-temperature setup (Figure 3.22). This made SEM analysis of the particles synthesized in the high-temperature setup more difficult.

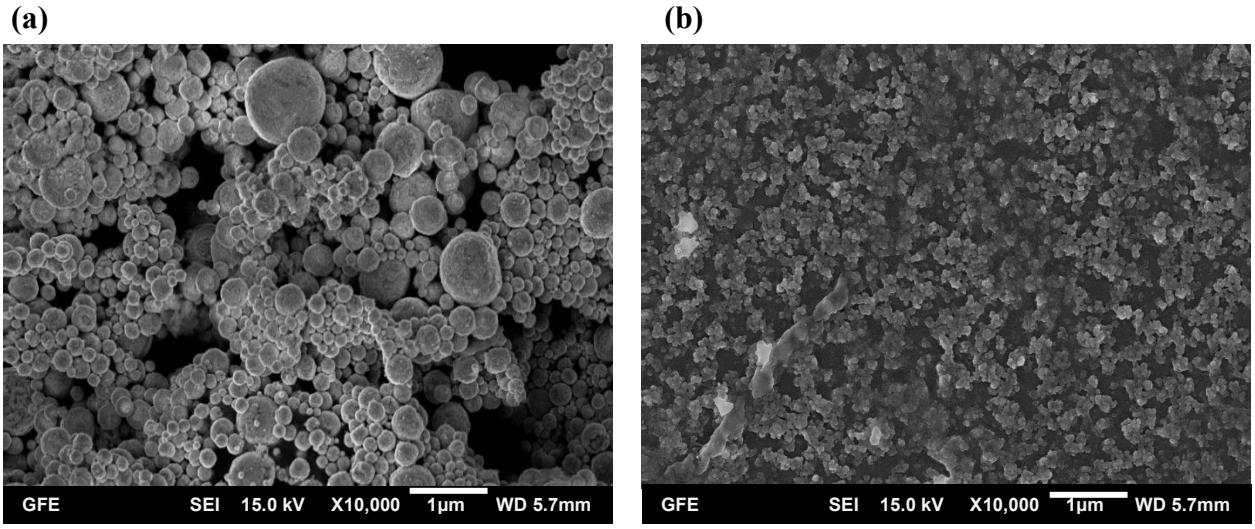

Figure 3.21. SEM analysis of AgCoCuFeNi particles at 900 °C and 0.05 M with residence time ranged (a) 5.3 s, (b) 23.8 s

EDS spectrum of the particles synthesized with the residence time of 23.8 s clearly shows that none of the five metal elements constituting the AgCoCuFeNi HEA nanoparticles were formed (Figure 3.23b). We believe that more reaction or operating time is needed to obtain the desired nanoparticles since the residence time of aerosol droplets inside the large tubular reactor is approximately 4 times higher than that of the small tubular reactor. We also believe that the replacement of the alumina glass tube or the increase in the gas flow rate are essential parameters to be considered.

(a)

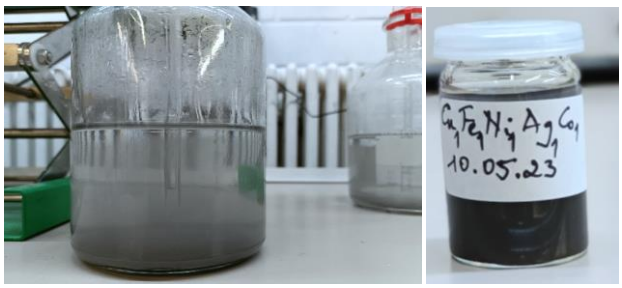

(b)

Figure 3.22. AgCoCuFeNi particles synthesized with residence time (a) 5.3 s, (b) 23.8 s

(a) **(b)**

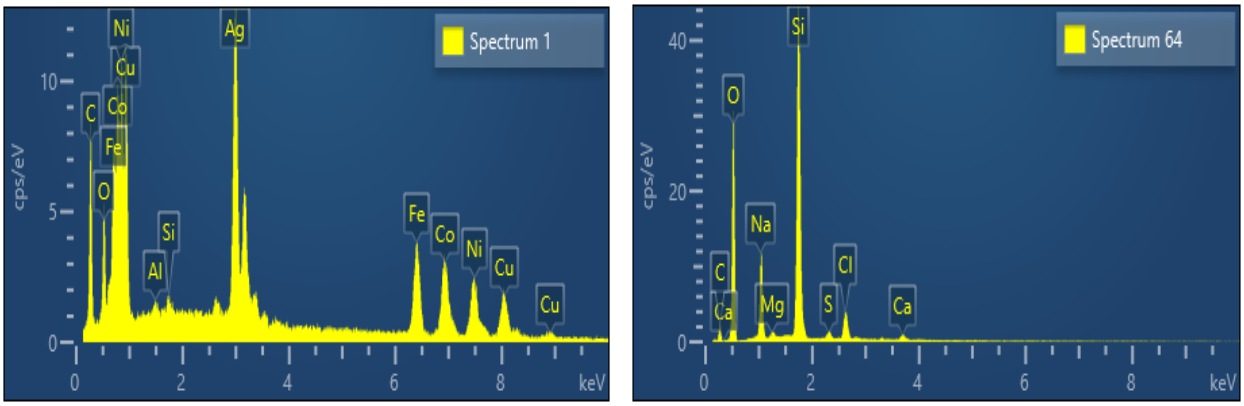

Figure 3.23. EDS spectrums for AgCoCuFeNi particles at 900 °C and 0.05 M with residence time ranged (a) 5.3 s, (b) 23.8 s

Conclusion

The optimization of synthesis conditions for spherical AgCoCuFeNi nanoparticles can be effectively achieved by adjusting the furnace temperature, the precursor solution concentration, and the residence time of the aerosol droplets inside the furnace.

GENERAL CONCLUSION

GENERAL CONCLUSION

In the first part of the work, the hydrogen reduction-assisted ultrasonic spray pyrolysis (USP-HR) technique was used to successfully produce simple alloy (undoped Fe_2O_3, Si-doped Fe_2O_3, and Pt-doped Fe_2O_3) particles at 700 and 950 °C. The primary focus of this study was to investigate the hydrogen reduction behavior of iron oxide (Fe_2O_3) in the absence and presence of additives (SiO_2 or Pt). The investigation revealed that the oxygen content of iron oxide particles, in the absence of additives, decreases with increasing temperature from 700 to 950 °C but significantly increases with the doping of 10 ml (40 wt.%) of SiO_2 at both reaction temperatures. The introduction of Si into the precursor solution inhibits the hydrogen reduction of Fe_2O_3 by creating a layer enriched with SiOx on the surface of Si-doped Fe_2O_3 to block free surfaces of iron oxide, hindering their direct interactions with the reducing agent. The reduction inhibition, in the presence of Si, becomes even more pronounced at higher temperatures (950 °C). In contrast, the doping of only 5 ml (15 wt.%) of Pt significantly decreased the oxygen concentration in the synthesized particles by accelerating the hydrogen reduction of Fe_2O_3 at 700 °C. Metallic iron (Fe), obtained in the undoped Fe_2O_3 run at only 950 °C, was also formed at 700 °C in the Pt-doped Fe_2O_3 run. At low temperatures and with a low Pt concentration, Fe particles can directly be produced from the hydrogen reduction of Fe_2O_3 due to platinum's catalytic role in offering active sites on its surface to induce the hydrogen spillover effect.

It is shown that catalytic reactions often involve the manipulation of surface oxygen species, and the knowledge gained from this study could lead to improved catalyst design and performance. The ability to efficiently generate metallic iron (Fe) from iron oxide nanoparticles at lower temperatures, especially with Pt-doping, could enhance catalytic activity in hydrogenation processes. Si-doped Fe_2O_3 NPs could also be used to create catalyst supports with enhanced stability and controlled redox properties.

In the second part of the work, spherical equiatomic AgCoCuFeNi high entropy alloy nanoparticles were successfully produced via hydrogen reduction-assisted ultrasonic spray pyrolysis (USP-HR) at temperatures below the melting point of each alloying metal. The study focused on investigating the influence of reaction temperature, precursor solution concentration, and residence time on the particle size, morphology, composition, and crystallinity of AgCoCuFeNi nanoparticles using SEM, EDS, and XRD characterization tools. The results are given below:

- Synthesis performed in the low-temperature setup at 600, 700, 800, and 900 °C starting from 0.05 M precursor mixture of the five metal salts revealed that increasing reaction temperature led to smaller and smoother spherical particles. The average particle size decreased from 428 to 264 nm with an increase in temperature from 600 to 900 °C. Four of the metal elements (Ag, Co, Cu, Fe, and Ni) making up the AgCoCuFeNi composition were present in very close proportions when the temperature reached 900 °C, while the at.% of Cu remained relatively large. The oxygen concentration in the synthesized particles decreased with increasing reaction temperature.

- Synthesis performed in the low-temperature setup with 0.25, 0.1, and 0.05 M precursor solutions at 900 °C resulted in narrower size distribution and uniformity of the AgCoCuFeNi NPs by reducing the solution concentration to 0.05 M. The average particle sizes using 0.25, 0.1, and 0.05 M solutions were 294, 641, and 264 nm, respectively. The five metal elements appeared to be in closer proportions at 0.25 and 0.05 M than at 0.1 M concentrations. The atomic percentage of oxygen decreased with decreasing precursor solution concentration.

- Synthesis performed in both the small and large tubular reactors with 0.05 M precursor solution at 900 °C revealed a decrease in the precision of AgCoCuFeNi particle microstructure and composition as the residence time increased from 5.3 s (small setup) to 23.8 s (the large setup). None of the five metal elements were formed in the large tubular reactor.

AgCoCuFeNi nanoparticles, being a high entropy alloy with a complex composition, can exhibit enhanced catalytic activity compared to traditional catalysts in various chemical reactions (e.g., hydrogenation, oxidation, and reduction processes) and be used as electrode materials to potentially improve battery (e.g., lithium-ion batteries) performance and cycle life. The outcomes of this study provide valuable insights into optimizing the synthesis of AgCoCuFeNi nanoparticles.

However, further research and development are needed to fully explore and validate the practical utility of AgCoCuFeNi nanoparticles in these fields and beyond.

PUBLICATIONS

1. *In Metals*: Hydrogen reduction of iron (III) nitrate from an aerosol by ultrasonic spray pyrolysis. Authors: Srećko Stopić [1,*], Ayadjenou Humphrey Hounsinou [1], Stéphane Aka Koffi [2]…
(*Status:* √ *Received* √ *Accepted* ☐ *Published)*

2. *In Metals*: Synthesis of AgCoCuFeNi high entropy alloy nanoparticles by USP-HR. Authors: Srećko Stopić [1,*], Ayadjenou Humphrey Hounsinou [1], Stéphane Aka Koffi [2]…
(*Status:* √ *Received* √ *Accepted* ☐ *Published)*

FUTURE WORK

For future work, the aim will be three-fold:

✓ Exploring additional catalysts based on other noble metals such as palladium (Pd), rhodium (Rh), ruthenium (Ru), and iridium (Ir) for the hydrogen reduction of Fe_2O_3. The primary focus will be on conducting a comparative analysis between at least two catalysts by assessing their catalytic activity and overall performance in the hydrogen reduction of Fe_2O_3 through advanced characterization techniques, including high-resolution X-ray diffraction (XRD) and X-ray photoelectron spectroscopy (XPS).

✓ Investigating the influence of other processing parameters (reaction time, gas flow rate, ultrasonic frequency, and even the type of the USP apparatus) on AgCoCuFeNi nanoparticles to improve the properties of the HEA NPs which were beyond the scope of this dissertation. High-resolution and 2D-XRD will also be used in this case to precisely determine the crystal phase structures of AgCoCuFeNi nanoparticles.

✓ Exploring new high entropy alloy compositions by increasing the number of principle metal elements (e.g., up to 8, including Ag, Co, Cu, Fe, and Ni) to see whether the increase in configurational entropy can stabilize the resulting solid solution and yield a single-phase crystal structure in the synthesized particles.

REFERENCES

[1] Abedi, M., Asadi, A., Vorotilo, S., & Mukasyan, A. S. (2021). A critical review on spark plasma sintering of copper and its alloys. *Journal of Materials Science*, *56*(36), 19739–19766. https://doi.org/10.1007/s10853-021-06556-z

[2] ADB (2012). Mining Industry Prospects in Africa. Retrieved August 16, 2023, from https://blogs.afdb.org/fr/afdb-championing-inclusive-growth-across-africa/post/mining-industry-prospects-in-africa-10177

[3] APP (2013). Equity in Extractives: Stewarding Africa's Natural Resources for All, at 44. Retrieved August 16, 2023, from https://reliefweb.int/sites/reliefweb.int/files/resources/relatorio-africa-progress-report-2013-pdf-20130511-125153.pdf

[4] Ali, N., Teixeira, J. A., Addali, A., Saeed, M., Al-Zubi, F., Sedaghat, A., & Bahzad, H. (2019). Deposition of Stainless Steel Thin Films: An Electron Beam Physical Vapour Deposition Approach. *Materials*, *12*(4), 571. https://doi.org/10.3390/ma12040571

[5] Arif, Z. U., Khalid, M. Y., ur Rehman, E., Ullah, S., Atif, M., & Tariq, A. (2021). A review on laser cladding of high-entropy alloys, their recent trends and potential applications. *Journal of Manufacturing Processes*, *68*, 225–273. https://doi.org/10.1016/j.jmapro.2021.06.041

[6] Arunachalam, R., Krishnan, P., & Rajaraman, M. (2019). A review on the production of metal matrix composites through stir casting – Furnace design, properties, challenges, and research opportunities. *Journal of Manufacturing Processes*, *42*, 213–245. https://doi.org/10.1016/j.jmapro.2019.04.017

[7] Avalo, O., Moura, F., Brocchi, E., & Navarro, R. C. s. (2010). Synthesis of Fe-Ni alloys by reduction with hydrogen. *65th ABM International Congress, 18th IFHTSE Congress and 1st TMS/ABM International Materials Congress* 2010, 3, 2277–2289. https://www.researchgate.net/publication/288820061_Synthesis_of_Fe-Ni_alloys_by_reduction_with_hydrogen

[8] Babić, E., Drobac, Đ., Figueroa, I. A., Laurent-Brocq, M., Marohnić, Ž., Mikšić Trontl, V., Pajić, D., Perrière, L., Pervan, P., Remenyi, G., Ristić, R., Salčinović Fetić, A., Starešinić, D., & Zadro, K. (2021). Transition from High-Entropy to Conventional Alloys: Which Are Better? *Materials*, *14*(19), 5824. https://doi.org/10.3390/ma14195824

[9] Bang, J. H., & Suslick, K. S. (2010). Applications of Ultrasound to the Synthesis of Nanostructured Materials. *Advanced Materials*, *22*(10), 1039–1059. https://doi.org/10.1002/adma.200904093

[10] Baptista, A., Silva, F. J. G., Porteiro, J., Míguez, J. L., Pinto, G., & Fernandes, L. (2018). On the Physical Vapour Deposition (PVD): Evolution of Magnetron Sputtering Processes for Industrial Applications. *Procedia Manufacturing*, *17*, 746–757. https://doi.org/10.1016/j.promfg.2018.10.125

[11] Baptista, A., Silva, F., Porteiro, J., Míguez, J., & Pinto, G. (2018). Sputtering Physical Vapour Deposition (PVD) Coatings: A Critical Review on Process Improvement and Market Trend Demands. *Coatings*, *8*(11), 402. https://doi.org/10.3390/coatings8110402

[12] Chen, P.-C., Liu, M., Du, J. S., Meckes, B., Wang, S., Lin, H., Dravid, V. P., Wolverton, C., & Mirkin, C. A. (2019). Interface and heterostructure design in polyelemental nanoparticles. *Science (New York, N.Y.)*, *363*(6430), 959–964. https://doi.org/10.1126/science.aav4302

[13] Cui, W., Li, W., Chen, W.-T., & Liou, F. (2020). Laser Metal Deposition of an AlCoCrFeNiTi0.5 High-Entropy Alloy Coating on a Ti6Al4V Substrate: Microstructure and Oxidation Behavior. *Crystals*, *10*(8), 638. https://doi.org/10.3390/cryst10080638

[14] Dutta, B., Shetake, N. G., Barick, B. K., Barick, K. C., Pandey, B. N., Priyadarsini, K. I., & Hassan, P. A. (2018). PH sensitive surfactant-stabilized Fe3O4 magnetic nanocarriers for dual drug delivery. *Colloids and Surfaces. B, Biointerfaces*, *162*, 163–171. https://doi.org/10.1016/j.colsurfb.2017.11.054

[15] Ebin, B., & Gürmen, S. (2011). Synthesis and Characterization of Nickel Particles by Hydrogen Reduction Assisted Ultrasonic Spray Pyrolysis(USP-HR) Method. *KONA Powder and Particle Journal*, *29*, 134–140. https://doi.org/10.14356/kona.2011016

[16] BMNT (2019). World Mining Data, Austria, 169 p. Retrieved August 16, 2023, from www.world-mining-data.info/wmd/downloads/PDF/WMD2019.pdf

[17] Feng, C., Faheem, M. B., Fu, J., Xiao, Y., Li, C., & Li, Y. (2020). Fe-Based Electrocatalysts for Oxygen Evolution Reaction: Progress and Perspectives. *ACS Catalysis*, *10*(7), 4019–4047. https://doi.org/10.1021/acscatal.9b05445

[18] Gao, S., Hao, S., Huang, Z., Yuan, Y., Han, S., Lei, L., Zhang, X., Shahbazian-Yassar, R., & Lu, J. (2020). Synthesis of high-entropy alloy nanoparticles on supports by the fast moving bed pyrolysis. *Nature Communications*, *11*(1), 2016. https://doi.org/10.1038/s41467-020-15934-1

[19] Garzón-Manjón, A., Meyer, H., Grochla, D., Löffler, T., Schuhmann, W., Ludwig, A., & Scheu, C. (2018). Controlling the Amorphous and Crystalline State of Multinary Alloy Nanoparticles in An Ionic Liquid. *Nanomaterials*, *8*(11), 903. https://doi.org/10.3390/nano8110903

[20] Germany (2023). In *The World Factbook*. Central Intelligence Agency. Retrieved August 16, 2023, from https://www.cia.gov/the-world-factbook/countries/germany/

[21] Germany Population (2023). Worldometer. Retrieved August 16, 2023, from https://www.worldometers.info/world-population/germany-population/

[22] Glasscott, M. W., Pendergast, A. D., Goines, S., Bishop, A. R., Hoang, A. T., Renault, C., & Dick, J. E. (2019). Electrosynthesis of high-entropy metallic glass nanoparticles for designer, multi-functional electrocatalysis. *Nature Communications*, *10*(1), 2650. https://doi.org/10.1038/s41467-019-10303-z

[23] Gupta, G., Tyagi, R. K., Kumar Rajput, S., Saxena, P., Vashisth, A., & Mehndiratta, S. (2020). PVD based thin film deposition methods and characterization / property of different compositional coatings—A critical analysis. *Materials Today: Proceedings*, *38*, 259–264. https://doi.org/10.1016/j.matpr.2020.07.132

[24] Gürmen, S., Stopić, S., & Friedrich, B. (2006). Synthesis of nanosized spherical cobalt powder by ultrasonic spray pyrolysis. *Materials Research Bulletin*, *41*(10), 1882–1890. https://doi.org/10.1016/j.materresbull.2006.03.006

[25] Haché, M. J. R., Cheng, C., & Zou, Y. (2020). Nanostructured high-entropy materials. *Journal of Materials Research*, *35*(8), 1051–1075. https://doi.org/10.1557/jmr.2020.33

[26] Hu, Z.-Y., Zhang, Z.-H., Cheng, X.-W., Wang, F.-C., Zhang, Y.-F., & Li, S.-L. (2020). A review of multi-physical fields induced phenomena and effects in spark plasma sintering: Fundamentals and applications. *Materials & Design*, *191*, 108662. https://doi.org/10.1016/j.matdes.2020.108662

[27] Huang, E.-W., & Liaw, P. K. (2019). High-temperature materials for structural applications: New perspectives on high-entropy alloys, bulk metallic glasses, and nanomaterials. *MRS Bulletin*, *44*(11), 847–853. https://doi.org/10.1557/mrs.2019.257

[28] IME Metallurgische Prozesstechnik Und Metallrecycling Der RWTH Aachen · Intzestraße 3, 52072 Aachen (n.d.). Retrieved August 16, 2023, from https://www.google.com/maps/place/IME+Metallurgische+Prozesstechnik+und+Metallrecycling+der+RWTH+Aachen/@50.7807074,6.0746083,17z/data=!3m1!4b1!4m6!3m5!1s0x47c09978172b7c23:0xd2e568fa25b8ea5e!8m2!3d50.7807074!4d6.0746083!16s%2Fg%2F121j1p_g?entry=ttu

[29] INN (2023). Top 10 Copper Producers by Country. Retrieved August 16, 2023, from https://investingnews.com/daily/resource-investing/base-metals-investing/copper-investing/copper-production-country/

[30] Inoue, A. (2000). Stabilization of Metallic Supercooled Liquid and Bulk Amorphous Alloys. *Acta Materialia*, *48*, 279–306. https://doi.org/10.1016/S1359-6454(99)00300-6

[31] Itaka, K., Ogasawara, T., Boucetta, A., Benioub, R., Sumiya, M., Hashimoto, T., Koinuma, H., & Furuya, Y. (2015). Direct Carbothermic Silica Reduction from Purified Silica to Solar-Grade Silicon. *Journal of Physics: Conference Series*, *596*(1), 012015. https://doi.org/10.1088/1742-6596/596/1/012015

[32] Jang, H. D., & Jeong, J. (1995). The Effects of Temperature on Particle Size in the Gas-Phase Production of TiO_2. *Aerosol Science and Technology*, *23*(4), 553–560. https://doi.org/10.1080/02786829508965337

[33] Jones, N., Ray, B., Ranjit, K. T., & Manna, A. C. (2008). Antibacterial activity of ZnO nanoparticle suspensions on a broad spectrum of microorganisms. *FEMS Microbiology Letters*, *279*(1), 71–76. https://doi.org/10.1111/j.1574-6968.2007.01012.x

[34] Karim, W., Spreafico, C., Kleibert, A., Gobrecht, J., VandeVondele, J., Ekinci, Y., & van Bokhoven, J. A. (2017). Catalyst support effects on hydrogen spillover. *Nature*, *541*(7635), 68–71. https://doi.org/10.1038/nature20782

[35] Kim, J., Shih, P.-C., Qin, Y., Al-Bardan, Z., Sun, C.-J., & Yang, H. (2018). A Porous Pyrochlore Y2[Ru1.6Y0.4]O7–δ Electrocatalyst for Enhanced Performance towards the Oxygen Evolution Reaction in Acidic Media. *Angewandte Chemie International Edition*, *57*(42), 13877–13881. https://doi.org/10.1002/anie.201808825

[36] Kim, J.-K., Jung, J., & Kang, Y. T. (2007). Absorption performance enhancement by nanoparticles and chemical surfactants in binary nanofluids. *International Journal of Refrigeration-Revue Internationale Du Froid - INT J REFRIG*, *30*, 50–57. https://doi.org/10.1016/j.ijrefrig.2006.04.006

[37] Köroğlu, M., Ebin, B., Stopic, S., Gürmen, S., & Friedrich, B. (2021). One Step Production of Silver-Copper (AgCu) Nanoparticles. *Metals*, *11*(9), 1466. https://doi.org/10.3390/met11091466

[38] Küçükelyas, B., Safaltın, Ş., Sam, E. D., & Gurmen, S. (2022). Synthesis, structural and magnetic characterization of spherical high entropy alloy CoCuFeNi particles by hydrogen reduction assisted ultrasonic spray pyrolysis. *International Journal of Materials Research*, *113*(4), 306–315. https://doi.org/10.1515/ijmr-2021-8519

[39] Kumar Katiyar, N., Biswas, K., Yeh, J.-W., Sharma, S., & Sekhar Tiwary, C. (2021). A perspective on the catalysis using the high entropy alloys. *Nano Energy*, *88*, 106261. https://doi.org/10.1016/j.nanoen.2021.106261

[40] Lin, S.-D., & Vannice, M. A. (1993). Toluene Hydrogenation Over Supported Platinum Catalysts. In L. Guczi, F. Solymosi, & P. Tétényi (Eds.), *Studies in Surface Science and Catalysis* (Vol. 75, pp. 861–874). Elsevier. https://doi.org/10.1016/S0167-2991(08)64062-8

[41] Liu, M., Zhang, Z., Okejiri, F., Yang, S.-Z., Zhou, S., & Dai, S. (2019). Entropy-Maximized Synthesis of Multimetallic Nanoparticle Catalysts via a Ultrasonication-Assisted Wet Chemistry Method under Ambient Conditions. *Advanced Materials Interfaces*, *6*, 1900015. https://doi.org/10.1002/admi.201900015

[42] Liu, Y., He, L., Mustapha, A., Li, H., Hu, Z. Q., & Lin, M. (2009). Antibacterial activities of zinc oxide nanoparticles against Escherichia coli O157:H7. *Journal of Applied Microbiology*, *107*(4), 1193–1201. https://doi.org/10.1111/j.1365-2672.2009.04303.x

[43] Ma, Y., Souza Filho, I. R., Bai, Y., Schenk, J., Patisson, F., Beck, A., van Bokhoven, J. A., Willinger, M. G., Li, K., Xie, D., Ponge, D., Zaefferer, S., Gault, B., Mianroodi, J. R., & Raabe, D. (2022). Hierarchical nature of hydrogen-based direct reduction of iron oxides. *Scripta Materialia*, *213*, 114571. https://doi.org/10.1016/j.scriptamat.2022.114571

[44] Mao, A., Ding, P., Quan, F., Zhang, T., Ran, X., Li, Y., Jin, X., & Gu, X. (2018). Effect of aluminum element on microstructure evolution and properties of multicomponent Al-Co-Cr-Cu-Fe-Ni nanoparticles. *Journal of Alloys and Compounds*, *735*, 1167–1175. https://doi.org/10.1016/j.jallcom.2017.11.233

[45] Meng, Z., Xiao, F., Wei, Z., Guo, X., Zhu, Y., Liu, Y., Li, G., Yu, Z.-Q., Shao, M., & Wong, W.-Y. (2019). Direct synthesis of L10-FePt nanoparticles from single-source bimetallic complex and their electrocatalytic applications in oxygen reduction and hydrogen evolution reactions. *Nano Research*, *12*(12), 2954–2959. https://doi.org/10.1007/s12274-019-2537-y

[46] Free, M. L. (2022). *Hydrometallurgy: Fundamentals and Applications*. Springer International Publishing. Salt Lake City, USA, 42 p. https://doi.org/10.1007/978-3-030-88087-3

[47] Miller, J. T., Meyers, B. L., Barr, M. K., Modica, F. S., & Koningsberger, D. C. (1996). Hydrogen Temperature-Programmed Desorptions in PlatinumCatalysts: Decomposition and Isotopic Exchange by SpilloverHydrogen of Chemisorbed Ammonia. *Journal of Catalysis*, *159*(1), 41–49. https://doi.org/10.1006/jcat.1996.0062

[48] *Minergyresources*, 2023. Retrieved August 16, 2023, from https://www.minergyresources.com//benin.php

[49] Miracle, D. B., Miller, J. D., Senkov, O. N., Woodward, C., Uchic, M. D., & Tiley, J. (2014). Exploration and Development of High Entropy Alloys for Structural Applications. *Entropy*, *16*(1), 494–525. https://doi.org/10.3390/e16010494

[50] Miracle, D. B., & Senkov, O. N. (2017). A critical review of high entropy alloys and related concepts. *Acta Materialia*, *122*, 448–511. https://doi.org/10.1016/j.actamat.2016.08.081

[51] Modupeola, D., & Popoola, P. (2023). High entropy nanomaterials for energy storage and catalysis applications. *Frontiers in Energy Research*, *11*. https://www.frontiersin.org/articles/10.3389/fenrg.2023.1149446

[52] Muñoz-Fernandez, L., Alkan, G., Milošević, O., Rabanal, M. E., & Friedrich, B. (2019). Synthesis and characterisation of spherical core-shell Ag/ZnO nanocomposites using single and two – steps ultrasonic spray pyrolysis (USP). *Catalysis Today*, *321–322*, 26–33. https://doi.org/10.1016/j.cattod.2017.11.029

[53] Navarro, R. C. s, Avalo, O., Moura, F., Brocchi, E., & Souza, R. (2014). Fe-Ni Alloy Synthesis Based on Nitrates Thermal Decomposition Followed by H2 Reduction. *Metallurgical Transactions B*, *45*. https://doi.org/10.1007/s11663-014-0221-x

[54] O'Connor, C. J., Kolesnichenko, V., Carpenter, E., Sangregorio, C., Zhou, W., Kumbhar, A., Sims, J., & Agnoli, F. (2001). Fabrication and properties of magnetic particles with nanometer dimensions. *Synthetic Metals*, *122*(3), 547–557. https://doi.org/10.1016/S0379-6779(01)00328-9

[55] Okuyama, K., Kousaka, Y., Tohge, N., Yamamoto, S., Wu, J. J., Flagan, R. C., & Seinfeld, J. H. (1986). Production of ultrafine metal oxide aerosol particles by thermal decomposition of metal alkoxide vapors. *AIChE Journal*, *32*(12), 2010–2019. https://doi.org/10.1002/aic.690321211

[56] Otanicar, T. P., Phelan, P. E., Prasher, R. S., Rosengarten, G., & Taylor, R. A. (2010). Nanofluid-based direct absorption solar collector. *Journal of Renewable and Sustainable Energy*, *2*(3), 033102. https://doi.org/10.1063/1.3429737

[57] Patterer, L., Mayer, E. B., Mráz, S., Pöllmann, P. J., Hans, M., Primetzhofer, D., Souza Filho, I. R., Springer, H. J., & Schneider, J. M. (2023). Effect of Si on the hydrogen-based direct reduction of Fe_2O3 studied by XPS of sputter-deposited thin-film model systems. *Scripta Materialia*, *233*, 115515. https://doi.org/10.1016/j.scriptamat.2023.115515

[58] Pinto, G., Silva, F. J. G., Porteiro, J., Míguez, J. L., Baptista, A., & Fernandes, L. (2018). A critical review on the numerical simulation related to Physical Vapour Deposition. *Procedia Manufacturing*, *17*, 860–869. https://doi.org/10.1016/j.promfg.2018.10.138

[59] Raabe, D., Tasan, C. C., & Olivetti, E. A. (2019). Strategies for improving the sustainability of structural metals. *Nature*, *575*(7781), Article 7781. https://doi.org/10.1038/s41586-019-1702-5

[60] Rioux, R. M., Song, H., Hoefelmeyer, J. D., Yang, P., & Somorjai, G. A. (2005). High-Surface-Area Catalyst Design: Synthesis, Characterization, and Reaction Studies of Platinum Nanoparticles in Mesoporous SBA-15 Silica. *The Journal of Physical Chemistry B*, *109*(6), 2192–2202. https://doi.org/10.1021/jp048867x

[61] Santo, L. (2008). Laser cladding of metals: A review. *International Journal of Surface Science and Engineering*, *2*(5), 327–336. https://doi.org/10.1504/IJSURFSE.2008.021345

[62] Schneider, J. M., Rohde, S., Sproul, W. D., & Matthews, A. (2000). Recent developments in plasma assisted physical vapour deposition. *Journal of Physics D: Applied Physics*, *33*(18), R173. https://doi.org/10.1088/0022-3727/33/18/201

[63] Shokouhmand, H., Ghazvini, M., & Shabanian, J. (2008). Performance Analysis of Using Nanofluids in Microchannel Heat Sink in different Flow Regimes and its simulation using Artificial Neural Network. *Lecture Notes in Engineering and Computer Science*, *2172*. https://www.researchgate.net/publication/44262252_Performance_Analysis_of_Using_Nanofluids_in_Microchannel_Heat_Sink_in_different_Flow_Regimes_and_its_simulation_using_Artificial_Neural_Network

[64] Simić, L., Stopic, S., Friedrich, B., Zadravec, M., Jelen, Ž., Bobovnik, R., Anžel, I., & Rudolf, R. (2022). Synthesis of Complex Concentrated Nanoparticles by Ultrasonic Spray Pyrolysis and Lyophilisation. *Metals*, *12*(11), 1802. https://doi.org/10.3390/met12111802

[65] Singh, S., Goyal, D. K., Kumar, P., & Bansal, A. (2020). Laser cladding technique for erosive wear applications: A review. *Materials Research Express*, *7*(1), 012007. https://doi.org/10.1088/2053-1591/ab6894

[66] Skrabalak, S. E., & Suslick, K. S. (2006). Porous Carbon Powders Prepared by Ultrasonic Spray Pyrolysis. *Journal of the American Chemical Society*, *128*(39), 12642–12643. https://doi.org/10.1021/ja064899h

[67] Son, B. D., Lee, J. K., & Yoon, W. Y. (2018). Effect of Tungsten Nanolayer Coating on Si Electrode in Lithium-ion Battery. *Nanoscale Research Letters*, *13*(1), 58. https://doi.org/10.1186/s11671-018-2460-2

[68] Song, C.-B., Park, J., & Park, K. (2004). Preparation of Fe-Si Nanoparticles in Furnace Aerosol Reactor. *Aerosol Science and Technology - AEROSOL SCI TECH*, *38*, 827–832. https://doi.org/10.1080/027868290503073

[69] Spreafico, C., Karim, W., Ekinci, Y., van Bokhoven, J. A., & VandeVondele, J. (2017). Hydrogen Adsorption on Nanosized Platinum and Dynamics of Spillover onto Alumina and Titania. *The Journal of Physical Chemistry C*, *121*(33), 17862–17872. https://doi.org/10.1021/acs.jpcc.7b03733

[70] Stahl, B., Ellrich, J., Theissmann, R., Ghafari, M., Bhattacharya, S., Hahn, H., Gajbhiye, N. S., Kramer, D., Viswanath, R. N., Weissmüller, J., & Gleiter, H. (2003). Electronic properties of 4-nm FePt particles. *Physical Review B*, *67*(1), 014422. https://doi.org/10.1103/PhysRevB.67.014422

[71] Stopić, S., Dvorak, P., & Friedrich, B. (2006). Synthesis of spherical nanosized silver powder by ultrasonic spray pyrolysis. *Metall*, 60, 377–382. https://www.researchgate.net/publication/321997712_Synthesis_of_spherical_nanosized_silver_powder_by_ultrasonic_spray_pyrolysis

[72] Stopić, S., Friedrich, B., Raić, K., Volkov-Husović, T., & Dimitrijević, M. (2008). Characterization of nano-powder morphology obtained by ultrasonic spray pyrolysis. *Metalurgija*, 14(1), 41–54.

[73] Stuart, B. W., & Stan, G. E. (2021). Physical Vapour Deposited Biomedical Coatings. *Coatings*, *11*(6), 619. https://doi.org/10.3390/coatings11060619

[74] Sun, L., Yuan, G., Gao, L., Yang, J., Chhowalla, M., Heydari Gharahcheshmeh, M., Gleason, K., Choi, Y., Hong, B., & Liu, Z. (2021). *Chemical vapour deposition*. *1*, 5. https://doi.org/10.1038/s43586-020-00005-y

[75] Sun, S., Murray, C. B., Weller, D., Folks, L., & Moser, A. (2000). Monodisperse FePt Nanoparticles and Ferromagnetic FePt Nanocrystal Superlattices. *Science*, *287*(5460), 1989–1992. https://doi.org/10.1126/science.287.5460.1989

[76] Tabasi, H., Mosavian, M. T., Sabouri, Z., Khazaei, M., & Darroudi, M. (2020). PH-responsive and CD44-targeting by Fe3O4/MSNs-NH2 Nanocarriers for Oxaliplatin loading and Colon cancer treatment. *Inorganic Chemistry Communications*, *125*, 108430. https://doi.org/10.1016/j.inoche.2020.108430

[77] Toparli, C., Ebin, B., & Gürmen, S. (2013). Iron-Nickel-Cobalt (Fe-Ni-Co) Alloy Particles Prepared by Ultrasonic Spray Pyrolysis and Hydrogen Reduction (USP-HR) Method. In *Processing and Properties of Advanced Ceramics and Composites V* (pp. 247–254). John Wiley & Sons, Ltd. https://doi.org/10.1002/9781118744109.ch27

[78] Toparli, C., Ebin, B., & Gürmen, S. (2017). Synthesis, structural and magnetic characterization of soft magnetic nanocrystalline ternary FeNiCo particles. *Journal of Magnetism and Magnetic Materials*, *423*, 133–139. https://doi.org/10.1016/j.jmmm.2016.09.005

[79] Tsai, M.-H., Wang, C.-W., Tsai, C.-W., Shen, W.-J., Yeh, J.-W., Gan, J.-Y., & Wu, W.-W. (2011). Thermal Stability and Performance of NbSiTaTiZr High-Entropy Alloy Barrier for Copper Metallization. *Journal of The Electrochemical Society*, *158*(11), H1161. https://doi.org/10.1149/2.056111jes

[80] Tyagi, H., Phelan, P., & Prasher, R. (2009). Predicted Efficiency of a Low-Temperature Nanofluid-Based Direct Absorption Solar Collector. *Journal of Solar Energy Engineering-Transactions of The Asme - J SOL ENERGY ENG*, *131*. https://doi.org/10.1115/1.3197562

[81] UNEP (2017). *Our work in Africa*. Retrieved August 16, 2023, from http://www.unep.org/regions/africa/our-work-africa

[82] Vassallo, P., Kumar, R., & D'Amico, S. (2004). Pool boiling heat transfer experiments in silica–water nano-fluids. *International Journal of Heat and Mass Transfer*, *47*(2), 407–411. https://doi.org/10.1016/S0017-9310(03)00361-2

[83] Vu, T. D., Chen, Z., Zeng, X., Jiang, M., Liu, S., Gao, Y., & Long, Y. (2019). Physical vapour deposition of vanadium dioxide for thermochromic smart window applications. *Journal of Materials Chemistry C*, *7*(8), 2121–2145. https://doi.org/10.1039/C8TC05014G

[84] Wang, S. (2013). Atomic Structure Modeling of Multi-Principal-Element Alloys by the Principle of Maximum Entropy. *Entropy*, *15*(12), 5536–5548. https://doi.org/10.3390/e15125536

[85] Wang, X., Dong, Q., Qiao, H., Huang, Z., Saray, M. T., Zhong, G., Lin, Z., Cui, M., Brozena, A., Hong, M., Xia, Q., Gao, J., Chen, G., Shahbazian-Yassar, R., Wang, D., & Hu, L. (2020). Continuous Synthesis of Hollow High-Entropy Nanoparticles for Energy and Catalysis Applications. *Advanced Materials*, *32*(46), 2002853. https://doi.org/10.1002/adma.202002853

[86] Wang, X., Guo, W., & Fu, Y. (2021). High-entropy alloys: Emerging materials for advanced functional applications. *Journal of Materials Chemistry A*, *9*(2), 663–701. https://doi.org/10.1039/D0TA09601F

[87] Wang, X., Li, Z., Wu, D.-Y., Shen, G.-R., Zou, C., Feng, Y., Liu, H., Dong, C.-K., & Du, X.-W. (2019). Porous Cobalt-Nickel Hydroxide Nanosheets with Active Cobalt Ions for Overall Water Splitting. *Small (Weinheim an Der Bergstrasse, Germany)*, *15*(8), e1804832. https://doi.org/10.1002/smll.201804832

[88] Wu, S., Zhu, D., Zhang, X., & Huang, J. (2010). Preparation and Melting/Freezing Characteristics of Cu/Paraffin Nanofluid as Phase-Change Material (PCM). *Energy & Fuels*, *24*(3), 1894–1898. https://doi.org/10.1021/ef9013967

[89] Yan, J., Kong, L., Ji, Y., White, J., Li, Y., Zhang, J., An, P., Liu, S., Lee, S.-T., & Ma, T. (2019). Single atom tungsten doped ultrathin α-Ni(OH)2 for enhanced electrocatalytic water oxidation. *Nature Communications*, *10*(1), Article 1. https://doi.org/10.1038/s41467-019-09845-z

[90] Yang, Y., Song, B., Ke, X., Xu, F., Bozhilov, K. N., Hu, L., Shahbazian-Yassar, R., & Zachariah, M. R. (2020). Aerosol Synthesis of High Entropy Alloy Nanoparticles. *Langmuir*, *36*(8), 1985–1992. https://doi.org/10.1021/acs.langmuir.9b03392

[91] Yao, Y., Huang, Z., Xie, P., Lacey, S. D., Jacob, R. J., Xie, H., Chen, F., Nie, A., Pu, T., Rehwoldt, M., Yu, D., Zachariah, M. R., Wang, C., Shahbazian-Yassar, R., Li, J., & Hu, L. (2018). Carbothermal shock synthesis of high-entropy-alloy nanoparticles. *Science (New York, N.Y.)*, *359*(6383), 1489–1494. https://doi.org/10.1126/science.aan5412

[92] Ye, Y. F., Wang, Q., Lu, J., Liu, C. T., & Yang, Y. (2016). High-entropy alloy: Challenges and prospects. *Materials Today*, *19*(6), 349–362. https://doi.org/10.1016/j.mattod.2015.11.026

[93] Yeh, J. W., Chen, Y. L., Lin, S. J., & Chen, S. K. (2007). High-Entropy Alloys – A New Era of Exploitation. *Materials Science Forum*, *560*, 1–9. https://doi.org/10.4028/www.scientific.net/MSF.560.1

[94] Yeh, J.-W., Chen, S.-K., Lin, S.-J., Gan, J.-Y., Chin, T.-S., Shun, T.-T., Tsau, C.-H., & Chang, S.-Y. (2004). Nanostructured High-Entropy Alloys with Multiple Principal Elements: Novel Alloy Design Concepts and Outcomes. *Advanced Engineering Materials*, *6*(5), 299–303. https://doi.org/10.1002/adem.200300567

[95] Zhang, Y., Zuo, T., Cheng, Y., & Liaw, P. K. (2013). High-entropy Alloys with High Saturation Magnetization, Electrical Resistivity and Malleability. *Scientific Reports*, *3*(1). https://doi.org/10.1038/srep01455

[96] Zhang, Y., Zuo, T. T., Tang, Z., Gao, M. C., Dahmen, K. A., Liaw, P. K., & Lu, Z. P. (2014). Microstructures and properties of high-entropy alloys. *Progress in Materials Science*, *61*, 1–93. https://doi.org/10.1016/j.pmatsci.2013.10.001

[97] Zhu, L., Xue, P., Lan, Q., Meng, G., Ren, Y., Yang, Z., Xu, P., & Liu, Z. (2021). Recent research and development status of laser cladding: A review. *Optics & Laser Technology*, *138*, 106915. https://doi.org/10.1016/j.optlastec.2021.106915

[98] Zou, Y., Wheeler, J. M., Ma, H., Okle, P., & Spolenak, R. (2017). Nanocrystalline High-Entropy Alloys: A New Paradigm in High-Temperature Strength and Stability. *Nano Letters*, *17*(3), 1569–1574. https://doi.org/10.1021/acs.nanolett.6b04716

[99] Zou, Z., Wang, B., Wang, C., Xiwen, Y., Cao, Y., Gao, L.-F., Luo, W., Wu, C., Yao, Y., & Lin, Z. (2020). *General synthesis of high-entropy alloy and ceramic nanoparticles in nanoseconds*. https://doi.org/10.21203/rs.3.rs-116889/v1

APPENDIX

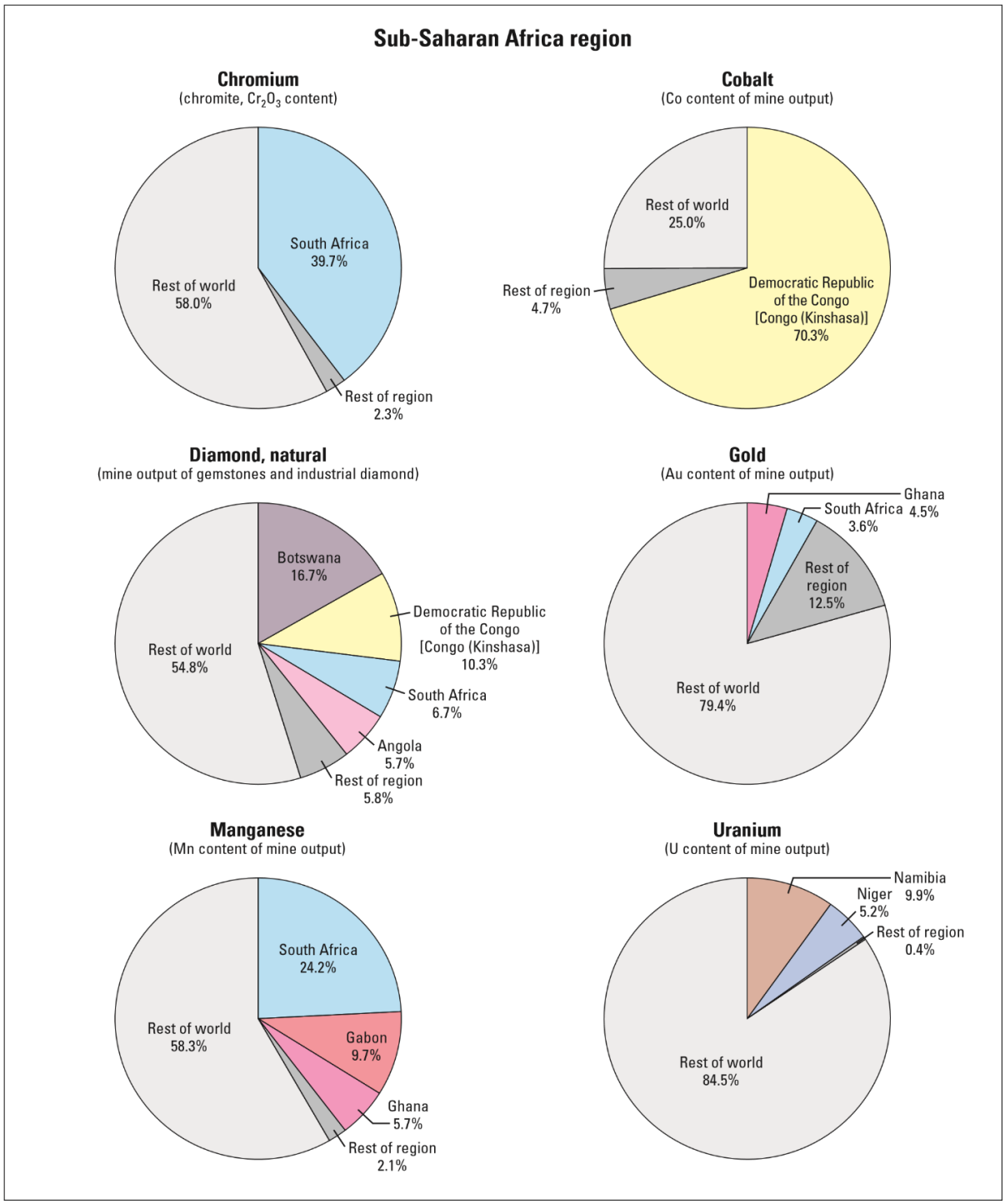

Appendix 1. Share of Sub-Saharan African countries in the world production of selected mineral products (chromite, cobalt, diamond, gold, manganese, and uranium) in 2018 (USGS, 2018)